THE UNIVERSITY *of* EDINBURGH

This thesis has been submitted in fulfilment of the requirements for a postgraduate degree (e.g. PhD, MPhil, DClinPsychol) at the University of Edinburgh. Please note the following terms and conditions of use:

- This work is protected by copyright and other intellectual property rights, which are retained by the thesis author, unless otherwise stated.
- A copy can be downloaded for personal non-commercial research or study, without prior permission or charge.
- This thesis cannot be reproduced or quoted extensively from without first obtaining permission in writing from the author.
- The content must not be changed in any way or sold commercially in any format or medium without the formal permission of the author.
- When referring to this work, full bibliographic details including the author, title, awarding institution and date of the thesis must be given.

Plasticity of Metallic Nanostructures - Molecular Dynamics Simulations

Con Healy

Doctor of Philosophy
The University of Edinburgh
2014

Abstract

During high speed cutting processes, metals are subject to high strains and strain rates. The dynamic nature of the deformation during high speed cutting makes it difficult to detect atomic scale deformation mechanisms experimentally. Atomic scale plasticity behaviour is often studied using various micromachining techniques such as micropillar compression testing, nanoindentation, and nanoscratching. However, strain rates in micromachining experiments are far lower than those seen during high speed cutting. Atomistic simulations can be used to study high strain rate plasticity at nanometre length scales. In this thesis, we present results from molecular dynamics simulations of plasticity in nanostructures. Results from simulations of uniaxial strain of both bcc and fcc nanopillars are presented. We find that the outcomes of these uniaxial strain simulations depend sensitively on the initial configurations of the systems. In particular, the choice of crystallographic surfaces on the faces of the pillars and the means by which strain is implemented in the simulations can affect the simulation results. We find that the twinning anti-twinning asymmetry in bcc materials causes nanopillars to deform by dislocation glide in compression and by twinning in tension. This explains the compression tension asymmetry reported experimentally in bcc micropillars. We find that deformation is mediated by glide of shockley partials in fcc pillars for compressive and tensile strains. Simulations of pure shear of nanocrystalline Fe are also presented. We find a change in deformation mechanisms for this system when at high temperatures. At low temperatures, plasticity is mediated in part by dislocation glide and twinning. However, at temperatures above 1200K the deformation is dominated by grain boundary sliding, recrystallization, and amorphization.

Lay Summary

Objects made of metals are often subject to applied forces or stresses. Engineers and scientists try to predict how the metals react in such conditions. Stresses will cause the structure and shape of metals to deform. When low stresses are applied to metals, the metal can typically recover its original shape when the stress is removed. This is known as elastic deformation. High stresses cause an irreversible change in the shape or configuration of the metal. This is known as plastic deformation or plasticity. The mechanical properties of metals are dependent on atomic scale processes. These processes are difficult to observe experimentally. In many situations where plasticity is observed it is not currently possible to determine conclusively what the atomic level deformation mechanisms are. It is therefore necessary to use computer simulations in order to understand these atomic level processes and to improve material performance. One example of such a situation is the plasticity observed in metals during high speed cutting. The microscopic structure of the metals can be examined before and after the cutting has taken place. However, it is currently not possible to examine the microscopic structure in the metals during the cutting process. Plasticity at small length scales is examined in metals using a variety of techniques. To study plasticity at micron and nanometre length scales, microscale and nanoscale pillars consisting of a particular metal can be created. These pillars are used in techniques known as micropillar and nanopillar compression testing which involve plastically deforming microscale and nanoscale pillars of the metals in question. However the strain rates applied to these structures differ greatly from those seen during high speed cutting. In this thesis, we use atomic scale computer simulation techniques to examine the deformation mechanisms in nanoscale metallic structures at high strain rates. We examine plasticity in nanopillars and in polycrystalline samples which have a similar structure to bulk metals.

Declaration

I declare that this thesis was composed by myself, that the work contained herein is my own except where explicitly stated otherwise in the text, and that this work has not been submitted for any other degree or professional qualification except as specified.

Parts of this work have been published in [1] and [2].

(*Con Healy, 2014*)

Acknowledgements

The work required to complete this thesis would not have been possible without the help of many people.

I would like to thank my supervisor, Graeme Ackland, for his continued support and patience.

I would also like to thank all my colleagues in the MaMiNa project, in particular Carsten Siemers whose energy and enthusiasm was key in making MaMiNa a fantastic project to be a part of.

I would like to thank my MaMiNa colleagues here in Edinburgh, Bengt Tegner and Linggang Zhu, for much useful discussion and for making my MaMiNa related travel experiences so much easier and more enjoyable.

Thanks to EU Framework 7 for financial support.

A special thanks goes to my parents who were always there to support me through the most difficult times during my PhD.

Finally I would like to thank my partner, Rachel, to whom this thesis is dedicated. Her love and support kept me sane at the most testing of times and this thesis would certainly not have been possible without her.

Contents

List of Figures

List of Tables

Chapter 1

Introduction

Metals are materials that are commonly used because of their strong structural and mechanical properties. Metals are key materials in a wide range of industries including the construction industry and the aerospace and automotive industries. For these reasons plasticity of metals is a wide area of interest in science and engineering. An understanding of plasticity in metals is not just required for the sake of understanding structural integrity of engineering projects. It is also useful in relation to industrial machining processes.

Machining of metals is a process which is vital to many industries, in particular the automotive and aerospace industries. However, aspects of machining such as chip morphology are still difficult to predict. This makes the development of alloys which are easy to machine more difficult. Part of the reason for the limited understanding is due to the conditions under which deformation occurs in metals during machining. Parts of the metal are subject to extremely high strains, strain rates, and temperatures during these processes. Plastic deformation takes place so quickly and in such small parts of the metal that microscale plasticity behaviour is almost impossible to examine experimentally.

Many machining processes involve scraping the surface of a piece of metal at high speeds using a cutting tool. The shavings produced during these processes are known as chips and their morphology can have significant impacts on machining performance. Currently chip morphology is predicted and studied in metals using computer simulations based on empirical material models. However, these material models have to be extrapolated up to three orders of magnitude in strain rate as current materials testing techniques are limited to testing materials at

strain rates far lower than those that occur in parts of a metal during machining.

In recent years various metallic microstructures and nanostructures have become major areas of interest. For example, it is now possible to create pillars and wires of metals at the nanoscale consisting of a single crystal. The plasticity behaviour of these structures can be strikingly different from that of bulk metals. In addition to this the recent development of nanocrystalline metals has led to a range of interesting research demonstrating that they have strikingly different mechanical properties from coarse grained metals [6]. Nanoccrystalline metals have been found to be stronger than regular coarse grained metals and are generally less ductile [7]. The small grain size usually results in a change in the dominant deformation mechanism from dislocation activity to grain boundary sliding [8] (see chapter 2 for more information on deformation mechanisms). This change in deformation mechanism accounts for the observed increase in material strength. As the grain size is reduced further, the strength of nanocrystalline materials can begin to decrease again due to a large grain boundary surface area which assists grain boundary sliding [9]. Nanocrystalline metals tend to fracture if subject to tensile strains of more than a few percent [6, 7]. However, recent research suggests that the ductility of these materials can be dramatically increased by constructing the metals with grain size gradients [10].

As the length scales of interest have become smaller in experiments, the length scales accessible by atomistic simulation have grown. It is now possible to simulate systems of millions of atoms in molecular dynamics simulations spanning length scales of tens of nanometres.

In this thesis, results from molecular dynamics simulations of nanostructured materials are presented. Comparison is drawn between the results presented here and results from experiments on microstructures and nanostructures. Implications of the results for machining processes in bulk metals are also discussed.

1.1 Outline of Thesis

Chapter 2 presents some background on plasticity in metals. Deformation mechanisms are discussed with particular attention paid to fcc and bcc metals. Some details of modern experimental techniques for analysing mechanical

behaviour and plasticity in metals along with methods of modeling plasticity in macroscale metals are discussed.

Chapter 3 contains background on molecular dynamics simulations and related analysis techniques. The theoretical foundations of MD simulations are presented with particular focus on simulating metals. Analysis techniques for identification of defects and deformation mechanisms are presented along with an overview of relevant software.

Chapter 4 contains results from simulations of plasticity in metallic nanopillars showing that some relatively subtle aspects of the initial simulation configuration can have significant effects on the simulation results. Specifically, the surface orientation and the boundary conditions are found to affect the results of the simulations. These findings are discussed in relevence to existing literature on molecular dynamics simulations of nanopillar and nanowire plasticity.

In chapter 5 details of simulations of plasticity in nanopillars of bcc Fe. A tension compression asymmetry is found in the pillars, matching experimental results for plasticity in bcc micropillars and nanopillars. We find deformation occurs by dislocation glide in compression and by twinning in tension.

In chapter 6 simulations of plasticity in nanopillars of fcc Cu are presented. The differences between plasticity in compression and tension are minor, particularly in comparison with the pillars of bcc Fe presented in the chapter 5.

In chapter 7, simulations of shear in a polycrystalline sample of Fe are presented. Plasticity occurs through a combination of different deformation mechanisms including slip, twinning, and grain boundary sliding. At high temperatures and strains, a significant amount of amorphisation occurred in the system.

Overall conclusions from this thesis will be discussed in chapter 8. Some suggestions for future research in this area will also be discussed.

Chapter 2

Theory of Mechanical Deformation in Metals

In this chapter we discuss theory of plasticity in crystalline materials. For more information on metal plasticity see *Introduction to Dislocations* by Hull and Bacon [11].

2.1 Defects in Crystalline Materials

In this section we will discuss crystalline defects which occur in metals. We will start out by discussing point defects (i.e. defects which occupy a single lattice site) followed by line defects and then planar defects.

2.1.1 Point defects

Point defects are those which occupy a single lattice site. The most common types of point defects are interstitial atoms and crystal vacancies. Vacancies are defects which arise when a site normally containing an atom is empty. Owing to crystal stability, atoms surrounding the vacancy do not simply collapse into the vacancy site. Atoms surrounding the vacancy relax by moving toward the vacancy site slightly as shown in figure 2.1.

Interstitial atoms are atoms which occupy a site in the lattice not normally

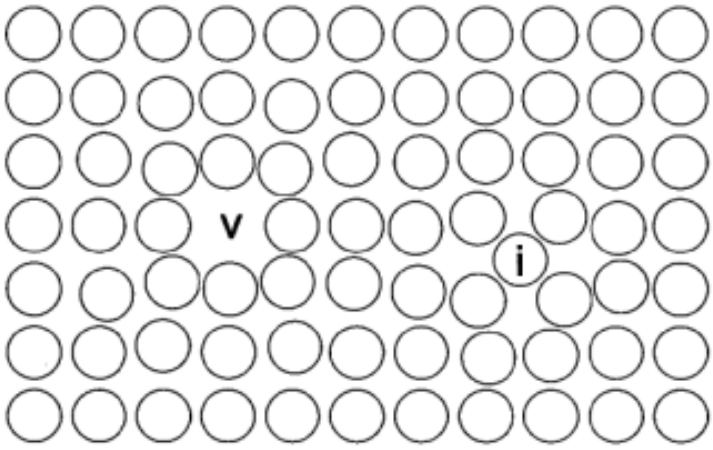

Figure 2.1 *Schematic of a vacancy (marked with a v) and an interstitial atom (marked with an i) in a 2d lattice.(From Hull and Bacon [11])*

occupied by an atom. The atoms surrounding the interstitial will relax by moving away from the interstitial atom. Many impurity atoms (in particular small atoms such as Hydrogen) can occupy interstitial sites in a metallic crystal.

2.1.2 Miller index bracket notation

In this thesis Miller indices will commonly be used to indicate directions and planes in crystal structures. We use the conventional Miller index bracket notation [11] to indicate whether we are referring to a specific direction, a family of directions, a specific plane, or a family of planes. The rules of this notation are as follows:

- Miller indices in square brackets, such as [100], refer to a specific direction.
- Indices in angle brackets represent a family of directions. For example, $\langle 100 \rangle$ refers to the following directions: [100], [010], [001], $[\bar{1}00]$, $[0\bar{1}0]$, and $[00\bar{1}]$.
- Indices in parentheses, such as (100) refer to a specific plane.
- Indices in curly brackets, such as $\{100\}$, refer to a family of planes.

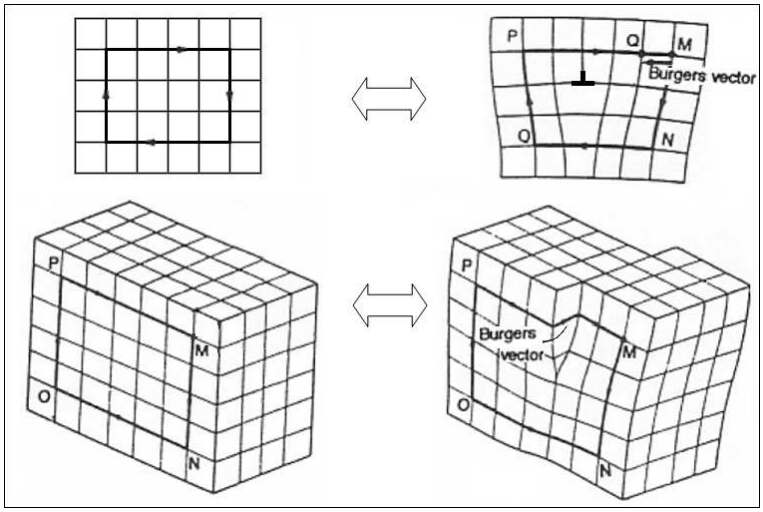

Figure 2.2 *Illustration of edge dislocation (top) and screw dislocation (bottom) and associated Burgers vectors.(From Hull and Bacon [11])*

2.1.3 Dislocations

Dislocations are line defects in crystals. The presence of dislocations was predicted independently by several scientists in the 1930s [11–16]. They can be broken down into two main categories, edge dislocations and screw dislocations. We first consider dislocations in a cubic lattice for the sake of simplicity. Edge dislocations can be described as the defect arising from inserting a half plane of atoms in between two planes. This sort of dislocation is shown in the top of figure 2.2. The line running along the edge of this inserted plane is the dislocation line. In the edge dislocation in figure 2.2 the dislocation line runs into the page.

A screw dislocation is shown in the bottom of figure 2.2. This defect can be described as the one created when one makes a slice on a particular half plane in the crystal and shears the crystal in opposite directions on either side of this slice. The line separating the sheared from the unsheared region on this plane is the dislocation line.

In general dislocation lines in crystalline materials are not always straight. Non straight dislocation lines consist of segments of edge and screw dislocations and are said to have mixed edge/screw character.

A useful way of characterising dislocations is by Burgers vectors. The Burgers vector of a dislocation is calculated by first constructing a Burgers circuit in the lattice enclosing the dislocation line. A Burgers circuit is made up of a sequence of

lines connecting atoms to neighbouring atoms in a crystal which forms a closed loop surrounding a dislocation line. Such a circuit is shown around the edge dislocation in figure 2.2. The path MNOPQ is a Burgers circuit. If the same circuit is traversed in a dislocation free crystal, the path traced will no longer form a closed loop. The additional vector required to make this loop closed is the Burgers vector. An illustration of a Burgers for an edge dislocation can be seen in figures 2.3 (a) and (b). In figure 2.3 (a) a Burgers circuit is represented by a black line in a 2 dimensional square lattice containing an edge dislocation. If the same sequence of movements between atomic sites is taken in a dislocation free lattice, as shown in 2.3 (b), a closed circuit is not formed. The additional displacement, represented by the dashed line in figure 2.3 (b), to complete the circuit is the Burgers vector.

Burgers vectors in an edge and a screw dislocation are illustrated in figure 2.3 (c). If one compares the schematics for Burgers vectors in edge and screw dislocations in this figure, the following rules become clear:

- The Burgers vector in an edge dislocation is perpendicular to the dislocation line.
- The Burgers vector in a screw dislocation is parallel to the dislocation line.

For dislocations of mixed character the angle between the Burgers vector and the dislocation line will be between 0° and 90°. Generally, the most common dislocations observed in particular materials are the ones which have the shortest Burgers vectors.

Any lattice can constructed by layering planar layers of atoms in any given crystallographic direction. The arrangement of atoms on any given layer will form a 2 dimensional repeating lattice. The sequence of unique 2 dimensional atomic lattice planes occurring in a given lattice direction is known as the stacking sequence in that direction. Sometimes there is a stacking sequence in the direction of the Burgers vector. In this case more than one half plane of atoms is needed to create an edge dislocation in which the stacking sequence is preserved. If, for example, the stacking sequence of planes is ABAB.... in the direction of the Burgers vector then two additional half planes of atoms are required to construct an edge dislocation. Dislocations of this type will have a Burgers vector long enough to traverse enough planes to conserve the stacking sequence (i.e. two planes when the stacking is ABAB....). Such dislocations are known as

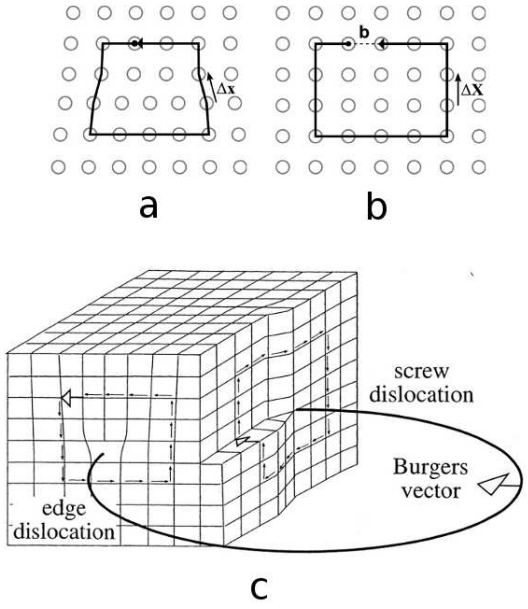

Figure 2.3 *(a)Schematic of a Burgers circuit in a 2 dimensional square lattice containing an edge dislocation (From paper by Stukowski et al [17]). (b) Illustration of same path traversed in forming the Burgers circuit in (a), taken in a dislocation free lattice (From paper by Stukowski et al [17]). The dashed line shows the additional path segment required to form a closed loop in the dislocation free lattice. This additional path segment is the Burgers vector. (c) Illustration of the Burgers vector in an edge and a screw dislocation. The arrows with large arrowheads represent Burgers vectors in each case (From Passchier and Trouw [18]).*

perfect dislocations. Perfect dislocations can separate into smaller dislocations called partial dislocations. A perfect edge dislocation can break into several dislocations with smaller Burgers vectors. Partial dislocations can be created by removing fewer than the required number of planes required to preserve the stacking sequence. They are particularly important in fcc crystals as we will see later. Partial dislocations separate regions of perfect crystal from regions containing defects known as stacking faults. This is illustrated in the schematic in figure 2.4

2.1.4 Stacking faults

As mentioned in the previous section, for any crystal structure, there is a repeating stacking sequence of crystalline planes in any given direction in the

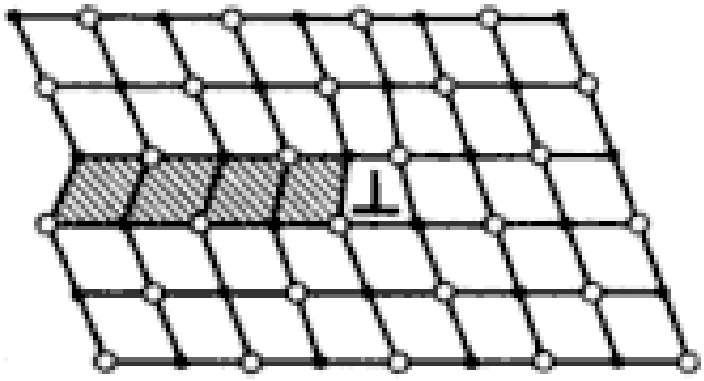

Figure 2.4 *Illustration of partial dislocations in a lattice with ABAB... stacking sequence. The dislocation is formed by the addition of a single half plane of atoms. The dislocation line runs into the page at the position marked by the inverted 'T' symbol. This defect can be thought of as that introduced when the atoms in the quadrant above and to the right of the dislocation line in the image are shifted to the right by half a lattice translation. A stacking fault (indicated by the shaded grey area) is produced to the left of the dislocation line. (From Vainshtein, Fridkin, and Indenbom [19]).*

lattice. A stacking fault is a planar defect in which the normal stacking sequence of planes is changed in a specific region. Stacking faults are common in fcc materials where, as we will discuss later, they are created due to the separation of perfect dislocations into partials. A diagram of a stacking fault in an ABC layered lattice can be seen in figure 2.5. Note that the stacking fault in this image is bounded by partial dislocations. The increase in the energy of the crystal per unit area of the stacking fault is known as the stacking fault energy.

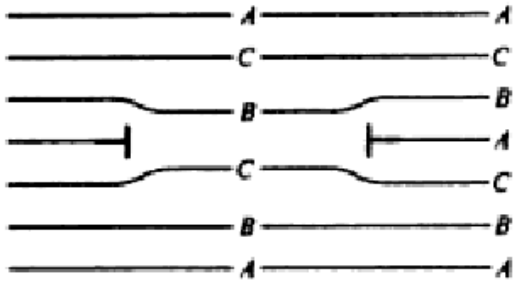

Figure 2.5 *Schematics of a stacking fault in a lattice with ABC stacking (such as fcc). Note that the stacking fault is bounded by partial dislocations. (Image from Haasen [20].)*

2.1.5 Twin boundaries

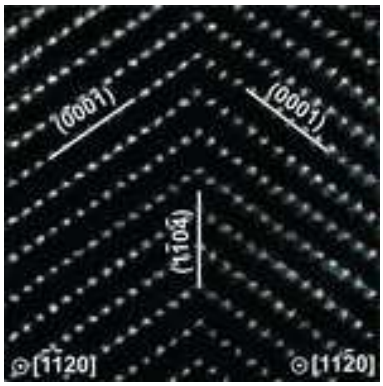

Figure 2.6 *STEM image of twin boundary in a sample of $LiCoO_2$. (From Moriwake et al [21].)*

Twin boundaries are planar defects in crystals where the crystal on one side of the twin boundary is a mirror image of the the crystal on the opposite side. Twin boundaries are normally created during plastic deformation of the crystal but they can also be created during crystal growth and during phase transitions. A STEM image of a twin boundary in $LiCoO_2$ can be seen in figure 2.6.

2.1.6 Grain Boundaries

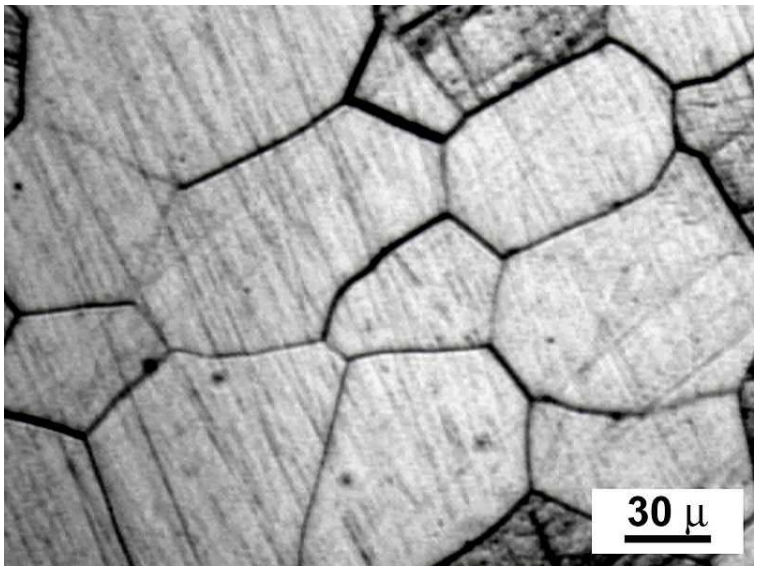

Figure 2.7 *A grain structure in a Ti alloy. (Image from Wikimedia Commons)*

Bulk crystalline solids rarely consist of just a single crystal in one orientation. Usually there are many regions in the crystalline material each with its own specific crystalline orientation. These regions are known as grains and the boundaries between these grains are known as grain boundaries. Figure 2.7 shows a typical grain structure in a Ti alloy.

2.2 Mechanisms of Mechanical Deformation

2.2.1 Dislocation Glide

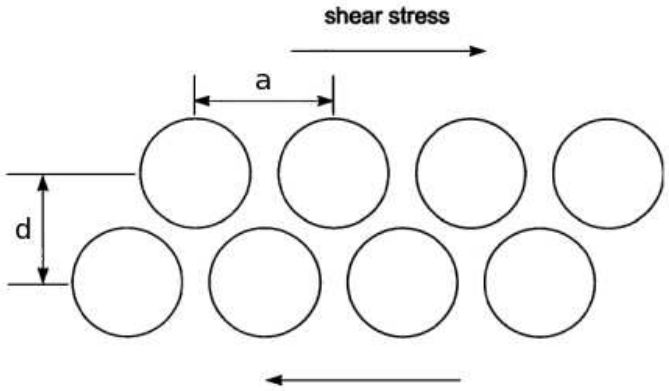

Figure 2.8 *Schematic of shear of two planes of atoms relative to each other in a defect free lattice. (From Hull and Bacon [11].)*

Prior to experimental observation of dislocations, the presence of dislocations in crystalline materials had been inferred from the difference between the experimentally observed values and the theoretical values of the shear stresses required to induce plastic deformation in a crystal.

A simple model for the relationship between shear stress and shear strain was proposed by Frenkel in 1926 [22]. Consider the planes of atoms shown in figure 2.8.

Frenkel considered the stress caused by the shear of such atomic planes across each other. The stress, σ, was assumed to vary sinusoidally with displacement, x, of one plane relative to another. This stress behaviour can be described by:

$$\sigma = \sigma_{max} \sin \frac{2\pi x}{a} \tag{2.1}$$

For small displacements, the shear modulus should be given by $G = \frac{d\sigma}{d\epsilon}$, where $\epsilon = \frac{x}{d}$. Combining this with equation 2.1, we have:

$$\sigma = \frac{Ga}{2\pi d} \sin \frac{2\pi x}{a} \tag{2.2}$$

The quntity σ_{max} in equation 2.1 is the theoretical shear strength required to induce plastic shear strain. Comparing equation 2.1 and equation 2.2, it can be seen that σ_{max} is given by:

$$\sigma_{max} = \frac{Ga}{2\pi d} \tag{2.3}$$

Equation 2.3 gives values for the theoretical shear stress which are far higher than observed experimentally. More sophisticated calculations of the shear stress as a function of strain result in values for σ_{th} as low as $G/30$ [23]. This is still far higher than experimental values which range from $10^{-8}G$ to $10^{-4}G$.

In a typical metal, the most common mechanism by which plastic deformation occurs is dislocation glide. Dislocation glide is the process in which the dislocation line moves on the surface which contains both the dislocation line itself and its Burgers vector. Glide of many dislocations results in a process called slip where planes of atoms, known as slip planes, slide across one another. Slip planes are normally the most densely packed of the crystallographic planes.

An illustration of glide of an edge dislocation can be seen in figure 2.9. Shearing the crystal in this figure by one atomic spacing requires breaking a single plane of atoms and connecting half of that plane to the existing half plane at the location of the dislocation. In contrast to this, shearing two planes in a perfect lattice (as illustrated in figure 2.8) requires breaking many planes of atoms in two and connecting each half plane with the next half plane in the sequence. For this reason the stress required to shear a crystal containing dislocations is much lower than that for a defect free crystal. This explains the discrepancy between the experimentally observed shear stress required to induce plastic deformation and the theoretical one which we have discussed above. The stress required to move a dislocation along a slip plane is known as the Peierls stress [24].

Slip occurs on specific crystallographic planes, known as slip planes, in a given material. The slip plane is usually the plane most densely packed with atoms. Slip also occurs in specific crystallographic directions which lie in the slip planes. This direction is usually the direction in the slip plane with the shortest spacing between consecutive atoms. In bcc crystals, for example, slip most often occurs

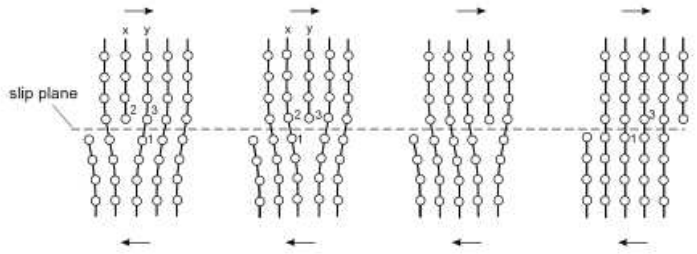

Figure 2.9 *Illustration of dislocation glide. (From Hull and Bacon [11].)*

on close packed {110} planes and in ⟨111⟩ directions. Often many different slip planes will intersect each other. Dislocations can then move from one slip plane to another. This process is known as cross slip.

Consider a single crystal subject to an applied force F. Now consider a specific slip plane and slip direction in this crystal. If θ is the angle between the force and the slip plane and λ is the angle between the force and the slip direction, then the shear stress resolved on the slip plane in the slip direction, σ_{res}, is given by:

$$\sigma_{res} = \frac{F}{A} \cos\theta \cos\lambda \tag{2.4}$$

where A is the cross-sectional area of the crystal. The quantity $\cos\theta \cos\lambda$ is called the Schmid factor. For many crystals, it has been found that slip occurs when σ_{res} reaches a critical value on a given slip plane known as the critical resolved shear stress. A material is said to obey Schmid's law if the critical resolved shear stress is a constant.

A segment of dislocation which is pinned at two ends is known as a Frank-Read source. Such a dislocation is illustrated in figure 2.10(a). When a stress is applied to this dislocation it bows out until a separate dislocation loop is formed and another dislocation segment is created in between the two pinning points. By this processes, many new dislocations are created in a sample during plastic deformation. Frank Read sources allow many dislocations to be created on a single plane when a stress is applied allowing a large amount of strain to be accommodated by dislocation glide.

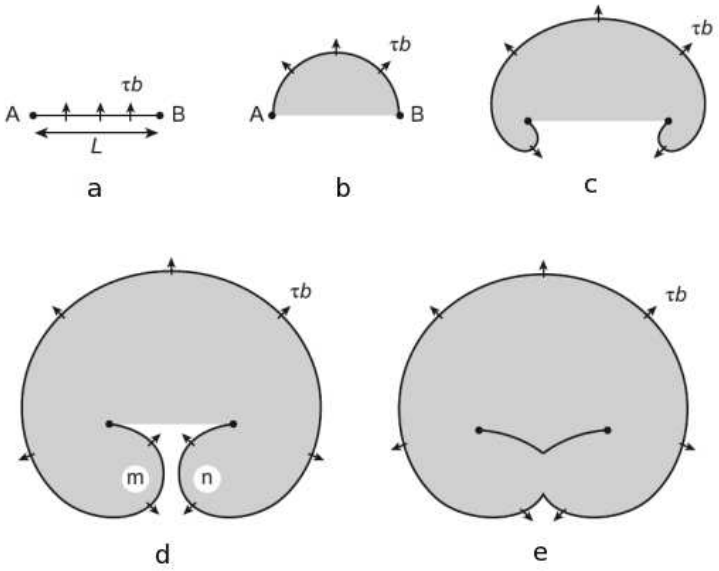

Figure 2.10 *Schematic showing dislocation creation from a Frank-Read source. (From Hull and Bacon [11].)*

2.2.2 Strain Hardening

Strain hardening (also known as work hardening) is a phenomenon in which metals can become stronger by deforming the material. As the materials are deformed the dislocation density in the solid increases due to the activity of dislocation sources such as the Frank-Read source. When the dislocation density is high enough, most dislocations will not easily be able to glide as their paths will be blocked by a network of dislocations. This means that dislocation glide is no longer as effective at introducing strains in the material as was the case in the crystal when its dislocation density was lower.

2.2.3 Twinning

Deformation twinning is the process by which twin boundaries are created during shearing of a crystal. Twinning occurs when one part of a crystal (called the twin region) is sheared in such a way that its orientation changes and it forms a mirror image of the part of the crystal in its original orientation (called the parent region). A twin boundary is hence formed in between these two regions. An illustration of the twinning process can be seen in figure 2.11. Twinning generally occurs when strain rates are too high for the strain to be accommodated

by dislocation glide. It tends to occur more often at low temperatures and in materials with low stacking fault energies.

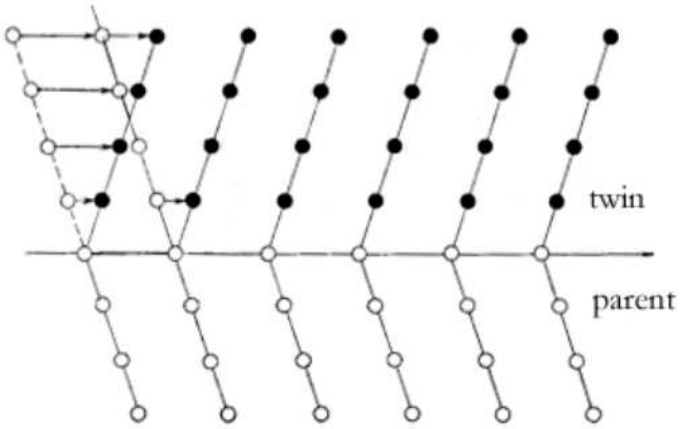

Figure 2.11 *Schematic of twinning in a crystalline material. The twinned region of the crystal changes orientation relative to the parent region resulting in the formation of a twin boundary. Arrows in the image indicate the direction of shear. (Image by Su Leen Wong of the Sibley School of Mechanical and Aerospace Engineering, Cornell University.)*

2.2.4 Grain Boundary Sliding

Grain boundary sliding is a deformation mechanism where grains in a crystalline material slide past each other [25]. This deformation mechanism contributes little to plasticity of typical metals near room temperature. However, it is frequently observed in nanocrystalline metals where the ratio of grain boundary surface to volume is high [26]. Grain boundary sliding occurs more often at high temperatures.

2.3 Plasticity in FCC Materials

2.3.1 Dislocations and slip

In fcc crystals the shortest interatomic separation is $\frac{1}{2}[110]$ and this is therefore the Burgers vector for the most common type of perfect dislocation found in the

crystals. However, perfect dislocations are rarely observed in fcc materials. The perfect $\frac{1}{2}\langle 110\rangle$ dislocations can split into partials which are far more commonly observed in fcc materials than perfect dislocations.

The most commonly observed type of partial dislocation found in fcc materials is called the Shockley partial and has Burgers vector of $\frac{1}{6}\langle 112\rangle$. A perfect $\frac{1}{2}\langle 110\rangle$ dislocation can separate into two Shockley partials by one of the following reactions:

$$\frac{1}{2}[\bar{1}10] \rightarrow \frac{1}{6}[\bar{2}11] + \frac{1}{6}[\bar{1}2\bar{1}] \tag{2.5}$$

$$\frac{1}{2}[\bar{1}01] \rightarrow \frac{1}{6}[\bar{2}11] + \frac{1}{6}[\bar{1}\bar{1}2] \tag{2.6}$$

$$\frac{1}{2}[0\bar{1}1] \rightarrow \frac{1}{6}[1\bar{2}1] + \frac{1}{6}[\bar{1}\bar{1}2] \tag{2.7}$$

This type of reaction is illustrated in the schematic in figure 2.12.

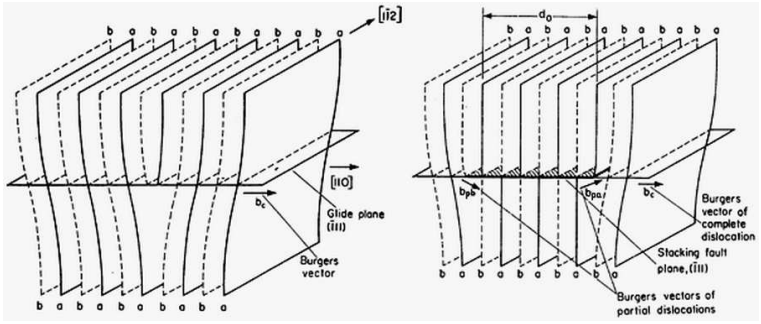

Figure 2.12 *Schematic illustrating the splitting of a complete* $\frac{1}{2}[110]$ *dislocation into Shockley partials. A crystal containing the complete dislocation is shown on the left and the corresponding crystal with the complete dislocation having split into partials is shown on the right. The Burgers vector for the complete dislocation and the two Shockley partials are labelled* b_c*,* b_{pa}*, and* b_{pb} *respectively.(From Hull and Bacon [11].)*

To understand why perfect dislocations in fcc materials tend to split into partials it is useful to consider the strain energy of a dislocation. Small strains in a crystal are often assumed to induce a Hooke's Law type response. If a dislocation with Burgers vector $\mathbf{b}$ is introduced to at some point it induces a displacement of magnitude b in the surrounding crystal. Assuming the Hooke's law type behaviour and neglecting the energy of the dislocation core, the energy of the dislocation will be proportional to b^2. This leads to Frank's rule which states that a perfect dislocation with Burgers vector $\mathbf{b}_1$ will split into two partials with Burgers vectors $\mathbf{b}_2$ and $\mathbf{b}_3$ if $b_1^2 > (b_2^2 + b_3^2)$. For a perfect $\frac{1}{2}\langle 110\rangle$ dislocation in

an fcc crystal with lattice constant a:

$$b^2 = \frac{a^2}{4}\left(1^2 + 1^2 + 0^2\right) = \frac{a^2}{2} \tag{2.8}$$

and for a Shockley partial we get:

$$b^2 = \frac{a^2}{36}\left(1^2 + 1^2 + 2^2\right) = \frac{a^2}{6} \tag{2.9}$$

It is therefore energetically favourable for a $\frac{1}{2}\langle 110\rangle$ dislocation in fcc crystals to split into Shockley partials.

As seen in figure 2.13 Shockley partials must be accompanied by a stacking fault. When a perfect $\frac{1}{2}\langle 112\rangle$ splits into two Shockley partials, the surface on the slip plane in between these partials will be a stacking fault. In figure 2.13 the presence of a Shockley partial at the M in the image results in a displacement of $\frac{1}{6}\,[1\bar{2}1]$ for the atoms in the region above and to the left of the dislocation relative to the locations of the atoms in an equivalent dislocation free lattice. This results in a stacking fault represented by the red line in the image. This combination of a stacking fault bounded by partial dislocations is known as an extended dislocation. The separation between these partials is limited by the stacking fault energy. The stacking fault energy is defined as the energy required to create a particular type of stacking fault divided by the stacking fault energy. As the separation between partial dislocations grows the stacking fault area grows and hence the energy required to generated such a stacking fault increases.

Slip occurs on $\{111\}$ planes. Figure 2.14 shows the Burgers vectors for a $\frac{1}{2}[110]$ perfect dislocation and two Shockley partials on a (111) plane. The direction of the slip motion follows a zig-zag path made up of Shockley partial Burgers vectors. The overall slip direction is $\langle 110\rangle$.

2.4 Plasticity in BCC Materials

2.4.1 Dislocations and slip

The shortest lattice vector in bcc crystals is $\frac{1}{2}\langle 111\rangle$ and this is also the most commonly observed Burgers vector for dislocations in bcc materials. Slip occurs in $\langle 111\rangle$ directions. Slip is observed to occur on many different planes in a bcc

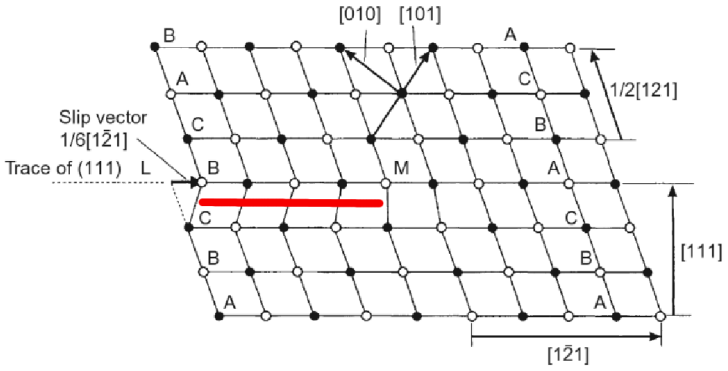

Figure 2.13 *Schematic illustrating stacking fault due to presence of a Shockley partial. The Shockley partial is located at the M in the figure. White circles represent atoms in a single* $10\bar{1}$ *plane and black circles represent atoms in a* $10\bar{1}$ *plane immediately above the plane containing the atoms represented by white circles. The letters A, B, and C are used to represent the stacking sequence in the crystal on the left and right sides in the image. Due to the presence of the dislocation, the atoms in the region above and to the left in the image are displaced by* $\frac{1}{6}[1\bar{2}1]$ *relative to their positions in an equivalent dislocation free lattice. This results in a stacking fault represented by the red line in the image. (From Hull and Bacon [11].)*

lattice. The most densely packed {110} planes are the most commonly observed slip planes, particularly at low temperatures. However, slip is also observed on {112} and {123} planes. It is worth noting that any given ⟨111⟩ slip direction intersects three {110} planes, three {112} planes, and six {123} planes. For this reason a process known as cross slip is found to occur frequently in bcc materials. This means that slip lines can be made up of many small segments on individual planes and the overall slip line need not be straight.

An interesting feature of slip in bcc crystals is the asymmetry of slip. For a specific crystal in a specific orientation, the favoured slip planes may differ in compression from those in tension.

Calculations of the core structures of screw dislocations in bcc crystals using interatomic potentials gives some insight into why this happens [27, 28]. Two equivalent core structures are outlined in figures 2.15 (a) and (b). Each image shows a {111} plane of atoms with a screw dislocation located at the centre of the plane. The Burgers vector of the dislocation is perpendicular to the plane. The black, grey, and white dots in these diagrams represent atoms. The length of the arrows in the diagram are proportional to the change in interatomic displacements

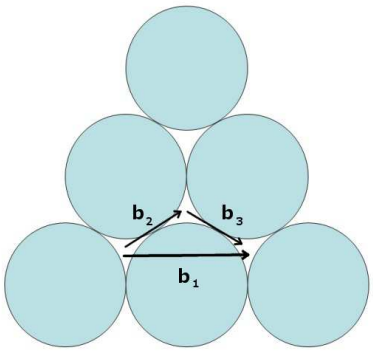

Figure 2.14 *Schematic of Burgers vectors for Shockley partial dislocations (labeled b_2 and b_3) and for their parent perfect dislocation (labeled b_1) . The blue circles here represent atoms on a* $\{111\}$ *plane.*

relative to a defect free crystal in the [111] (screw) direction. The arrow lengths are scaled such that an arrow which runs the full length from one atom to another corresponds to a displacement of $b/3$ where b is the Burgers vector.

The displacements are concentrated on three intersecting $\{110\}$ planes, each containing a short ranged unstable stacking fault due to a $\frac{1}{6}[111]$ displacement. These $\frac{1}{6}[111]$ cores are referred to as fractional dislocations. A stereographic projection of [110] and [112] planes in a [111] plane is shown in figure 2.15 (c) to indicate where the intersecting $\{110\}$ planes are in figures 2.15 (a) and (b).

Under the action of an applied stress, the core structures shown in figure 2.15 change. Figure 2.16 shows core structures for these dislocations under different applied stresses. The change in core structure depends on the direction of the applied stress and this gives rise to a compression tension slip asymmetry. This change in core structure affects the critical resolved shear stress for glide of the given dislocation. As a result, the critical resolved shear stress is not constant for bcc materials. These materials therefore do not obey Schmid's law.

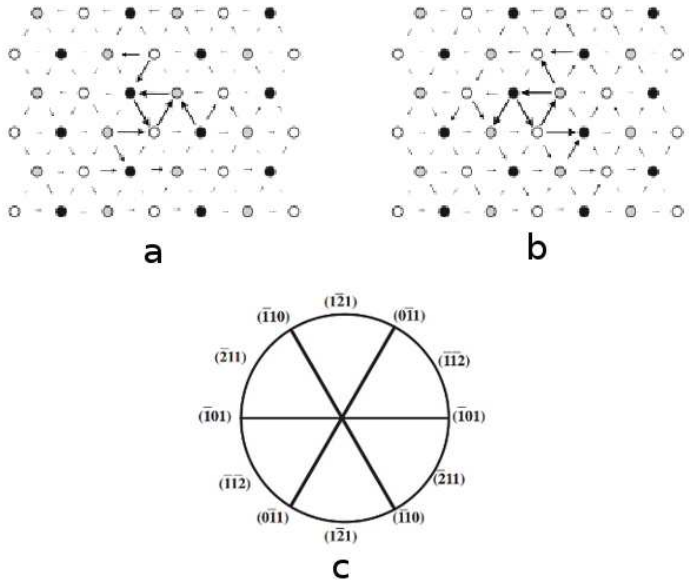

Figure 2.15 *(a) and (b) show degenerate core structures for* $\frac{1}{2}[111]$ *screw dislocations in bcc crystals. White, grey, and black circles represent atoms on three consecutive* [111] *planes. The arrows between atoms represent relative displacements between neighbouring atoms in the* [111] *(screw) direction. The length of the arrows is proportional to the magnitude of the displacement and these lengths are normalised so that an arrow with a length equal in magnitude to the separation between neighbouring atoms in the image represents a displacement of* $|\frac{1}{6}[111]|$*. The displacements represented by the arrows, as well as the dislocation line and Burgers vector are therefore directed into the page. (c) Stereographic projection showing the orientations of all* [110] *and* [112] *planes in a* [111] *plane. (Images by Vitek [29, 30].) (From Vitek [29].)*

2.4.2 Twinning

Twinning occurs in bcc metals on {112} planes. The stacking sequence for {112} planes is ABCDEFAB..... One can see from figure 2.17(b) that if the region of crystal above a plane labeled E for example is moved by a displacement of $\frac{1}{6}[\bar{1}11]$ then the E plane shifts to a C plane, the F plane changes to a D plane and so on. The resulting stacking sequence is ABCDCDE... If the adjacent plane now moves with the same displacement then the stacking sequence becomes ABCDCBC... If this process is repeated we will eventually have a stacking sequence of ABCDCBA... which is the stacking sequence of a twinned crystal with the twin boundary at the D plane. Displacements on successive planes like this have been observed to occur in bcc metals by the motion of $\frac{1}{6}\langle 111\rangle$ partial

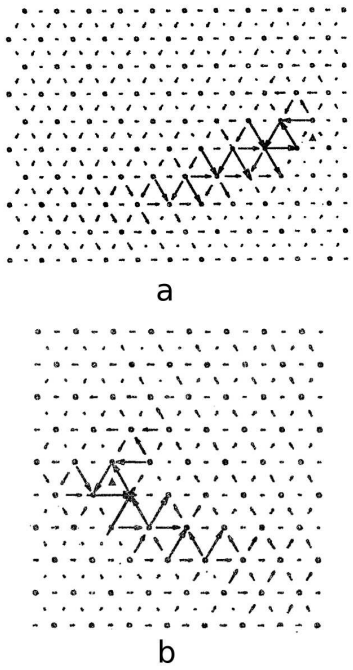

Figure 2.16 *Core structures of* $\frac{1}{2}[111]$ *dislocations under applied shear stresses of (a) 0.02G in the* $[\bar{1}01]$ *direction and (b) 0.021G in the* $[10\bar{1}]$ *direction. Applied stresses alter the core structure and the change depends on the direction of the applied shear stress. This results in a compression tension asymmetry in the plasticity behaviour. (From Duesbery, Vitek, and Bowen [28].)*

dislocations on successive planes.

It is clear from figure 2.17(b) that moving an E plane in the opposite direction from the one just described (i.e. a displacement of $\frac{1}{6}[1\bar{1}\bar{1}]$), then the E plane moves to a D plane and an unstable high energy stacking fault is created. There is therefore an asymmetry with respect to $\frac{1}{6}\langle 111\rangle$ displacements between successive $\{112\}$ planes. The direction which produces a twinned crystal is known as the twinning direction and the opposite direction is known as the anti-twinning direction.

2.4.3 The twinning-antitwinning slip asymmetry

We have just seen that glide of $\frac{1}{6}\langle 111\rangle$ partials on $\{112\}$ planes can create twin boundaries in bcc materials. Slip planes can only move in the twinning direction and not the antitwinning direction and this implies that the same applies for

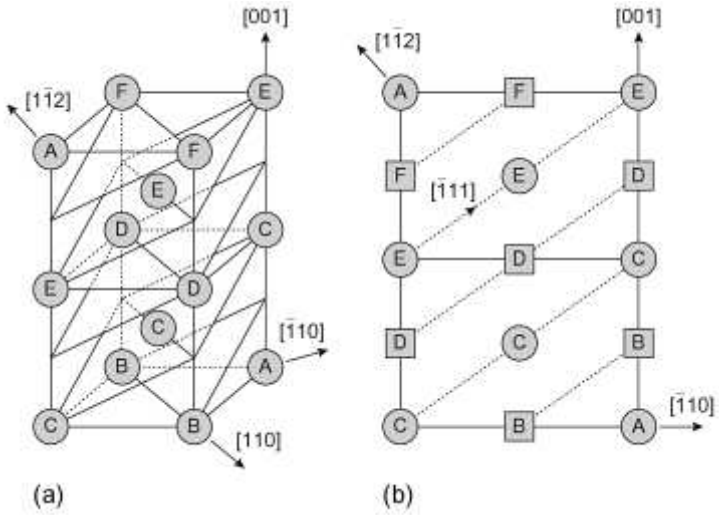

Figure 2.17 *(a) Illustration of the stacking sequence of* 112 *planes in a bcc crystal. (b) (110) projection showing stacking of* $(1\bar{1}2)$ *planes. The atoms marked by squares lie* $a/\sqrt{2}$ *above and below the circles marked by circles. (From Hull and Bacon [11].)*

$\frac{1}{6}\langle 111\rangle$ partials. This asymmetry is known as the twinning-antitwinning slip asymmetry and its effect is not confined just to partial dislocations. Perfect $\frac{1}{2}\langle 111\rangle$ dislocations are also affected by this asymmetry. This can be understood by looking at the concepts of the generalised stacking fault and the γ-surface introduced by Vitek[27]. Consider a crystal which is cut across a given plane so that it is split into two parts. One part of the crystal is then offset by some vector, $\mathbf{f}$, which lies in the plane in question. This results in a stacking fault with a stacking fault energy $\gamma(\mathbf{f})$. The function $\gamma(\mathbf{f})$ is the generalised stacking fault energy and can be represented by a surface which spans a unit cell of the material in question. This surface is known as the γ-surface. Note that $\gamma(\mathbf{f})$ is not the stacking fault energy. The stacking fault energy represents the energy of a stable stacking fault with atoms at and near the stacking fault in equilibrium positions. This is a scalar quantity. $\gamma(\mathbf{f})$ is a function which represents the energy required to create an atomic configuration where two regions in a lattice are displaced relative to each other by a displacement $\mathbf{f}$. Most of these configurations will not be stable equilibrium configurations. γ is a vector function representing the energy of many different configurations. $\mathbf{f}$ is usually considered as a two dimensional vector and γ can therefore be represented by a surface.

The γ-surfaces for $\{112\}$ planes are shown in figure 2.18. Note that the surface is asymmetric in the $\langle 111\rangle$ direction. This means that glide of any dislocation on

{112} planes is subject to the twinning-antitwinning asymmetry.

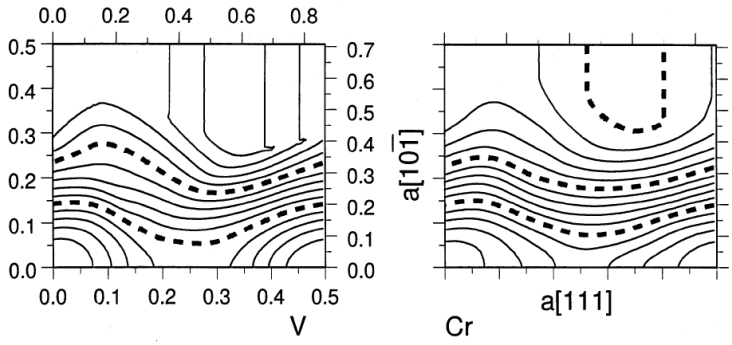

Figure 2.18 *The γ surfaces of {112} planes in bbc lattices of Vanadium (left) and Chromium (right) calculated using molecular statics simulations. (From Duesbery and Vitek [27].)*

2.5 Buckling

Under a large enough compressive load, small lateral forces or slight geometrical asymmetries will cause a column like structure such as a metal beam to bend in the centre and deform plastically. This process is called buckling and it is illustrated in figure 2.19. A beam will buckle if subject to a critical load, F_{cr}, which is given by:

$$F_{cr} = \frac{\pi^2 EI}{(KL)^2} \tag{2.10}$$

Here E is the Youngs modulus, I is the moment of inertia, and L is the length of the beam. K is a constant which depends on the boundary conditions of the beam. If the beam is fixed at both ends then $K = 0.5$ and if one end of the beam is free to move laterally then $K = 2$.

2.6 The Wulff Construction

In the remainder of this thesis, many structures with nanoscale dimensions and/or nanoscale structural features (such a grain boundaries) will be discussed. These structures will be referred to as nanostructures. In crystalline solids, each crystallographic surface has a corresponding surface energy. In fcc crystals the surface with the lowest surface energy is {111} and in bcc it is {110}. However,

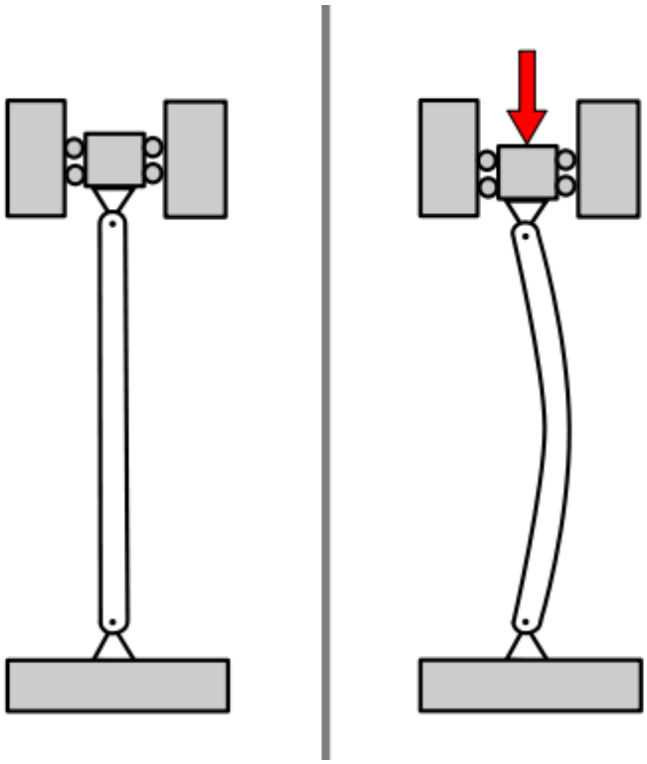

Figure 2.19 *Illustration of buckling in a column. (Image from Wikimedia Commons.)*

the surface energy of nanostructures is not necessarily minimised if all the surfaces are the crystallographic surfaces with the lowest surface energy. The total surface energy of a nanostructure is also lowered by reducing the overall surface area. The minimum energy configuration of a nanostructure is known as the Wulff construction and it often represents a compromise between a configuration with low energy surfaces and one where the total surface area is minimised. The excess energy, ΔG, of a nanostructure compared with the same number of atoms in a bulk lattice at equilibrium is:

$$\Delta G = \sum_i \Gamma_i O_i \tag{2.11}$$

where Γ_i is the surface energy per unit area of the ith face of the nanostructure and O_i is the surface area of the face. Note that the surfaces, O_i, are assumed to be flat. The Wulff construction is the configuration which minimises this quantity. Figure 2.20 shows a TEM image of the cross section of a $\langle 110 \rangle$ oriented Si nanowire. The Wulff construction for this nanostructure contains some high energy $\{100\}$ faces.

Many nanostructures in experiments are constructed in a metastable shape that is not the Wulff construction [31, 32]. Often such nanostructures may appear to have high energy surfaces but close inspection of the surfaces reveals that many facets of low energy surface exist on the apparent high energy surfaces [31]. These facets are usually the result of local surface reconstructions. Segments from the surface of a gold nanowire are shown in figure 2.21. Many small facets with low energy {111} type surface orientation are visible on these segments.

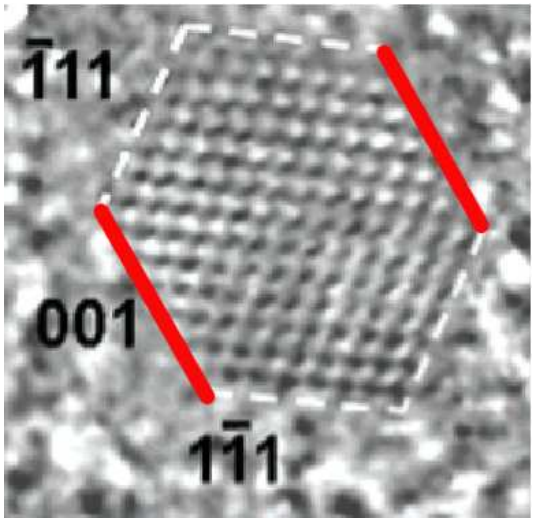

Figure 2.20 *TEM image showing the cross section of a* $\langle 110 \rangle$ *oriented Si nanowire. The nanowire contains some high energy* $\{100\}$ *faces. The* $\{100\}$ *faces are highlighted by the red lines in the image. (Image from article by Wu et al [33].)*

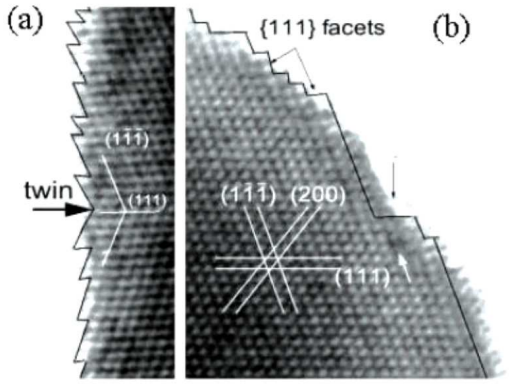

Figure 2.21 *Segments of gold nanowire showing many small* $\{111\}$ *facets on the surface. (Image by Tian et al [31].)*

2.7 Machining and Experimental Materials Testing

2.7.1 The MaMiNa collaboration

The work presented in this thesis was undertaken as part of a collaborative project called MaMiNa. The acronym MaMiNa stands for **Ma**cro, **Mi**cro, and **Na**no aspects of machining and the collaboration involved a collection of research groups (both experimental and computational) investigating plasticity at different length scales. Some of the experimental and computational techniques used within this collaboration include the Hopkinson-split experiments, quick stop experiments, finite element simulations, and various micromechanical testing techniques. In the next few sections we will discuss some of these techniques.

One of the main goals of this collaboration was to produce a Titanium alloy which is easy to machine by adding different alloying elements. Titanium alloys are particularly difficult to machine due to strong mechanical properties and poor thermal conductivity. This low thermal conductivity results in a large amount of heating near the cutting tool which can result in frequent damage to the tool. The research presented in this thesis addressed atomic scale processes during plastic deformation. Molecular dynamics simulations were used to characterise plasticity behaviour of various nanostructures which are particularly relevant to the broader research profile of the MaMiNa network. As we will see later, molecular dynamics simulations are useful for studying plasticity behaviour in machining processes due to the inherent limitations on the applied strain rate in the simulations. Nanostructures studied as part of this work include nanopillars and nanocrystalline samples. These structures were chosen to resemble single crystal metallic nanopillars and polycrystalline bulk metals, structures which are the subject of much experimental research within the MaMiNa collaboration.

The performance of the machining processes depends sensitively on the chip morphology as we will see below. However, studying the chip morphology can be difficult. Deformation takes place very quickly during machining processes and temperatures in parts of the machining chips can reach 1000°C. This makes observation of the microscale deformation mechanisms impossible.

2.7.2 Chips formed during machining processes

High speed cutting of metals involves carving into a piece of metal called the workpiece with a cutting tool as can be seen in figure 2.22. During this process metal chips are formed which can be separated into two main categories, continuous chips and segmented chips [34, 35]. The image in figure 2.22 shows a continuous chip being formed during cutting. These chips can grow to metres in length and can easily interfere with cutting machinery in an industrial setting. Often so called free machining alloys which produce segmented chips are developed to avoid this problem. However, there are not currently any commercially available free machining Ti alloys. The MaMiNa project aimed to address this problem. Figure 2.23 shows continuous and segmented chips from different alloys.

Figure 2.22 *Image showing high speed cutting of a Ti alloy. (Courtesy of Lenka Fusova of the MaMiNa collaboration.)*

Closer inspection of the morphology of continuous and segmented chips reveals that continuous chips have more or less constant thickness while segmented chips have a sawtooth profile as can be seen in figure 2.24. In continuous chips, the shear strain is distributed quite evenly throughout the chip while in segmented chips the shear is concentrated in shear bands. The shear bands in segmented chips deform under quite extreme conditions. In these shear bands strains of over 800% are reported with strain rates reaching $10^7 s^{-1}$ and temperatures believed to exceed 1000°C [34]. Predicting which types of chips will be produced in a given metal can be difficult. Finite element simulations (discussed below) based on empirical material models are used to study and predict chip morphology.

Figure 2.23 *Continuous chip (left) and segmented chips (right) produced during high speed cutting. (Image courtesy of Badya Zahra of the MaMinNa collaboration.)*

2.7.3 Hopkinson-Split bar testing.

The Hopkinson-split bar apparatus is used to acquire stress strain curves for macroscopic samples at high strain rates [37, 38]. Using this apparatus, strain rates of up to 1000 s^{-1} can be achieved. A diagram of an Hopkinson-split bar apparatus can be seen in figure 2.25 (a). The sample is placed directly in front of a metal bar (called the transmitted bar) and a second metal bar (the incident bar) is fired at the sample using a high pressure gas gun. The sample is compressed plastically and vibrations in the transmitted bar are recorded during this process. Analysis of vibrations in the transmitted bar can be used to calculate stress vs. strain curves for the deformed sample.

2.7.4 Plasticity of micropillars

Many experimental techniques are used to examine plasticity behaviour at the nanoscale and microscale. One such experimental technique is micropillar compression testing developed by Uchic *et al* [40]. The technique involves creating microscale (and sometimes nanoscale) pillars of metals using a focused ion beam. The pillars are etched from a single crystal. The pillars are compressed using an indenter and the the stress vs strain data is recorded during the indentation. Slip planes are clearly visible following the compression as can be seen from the image

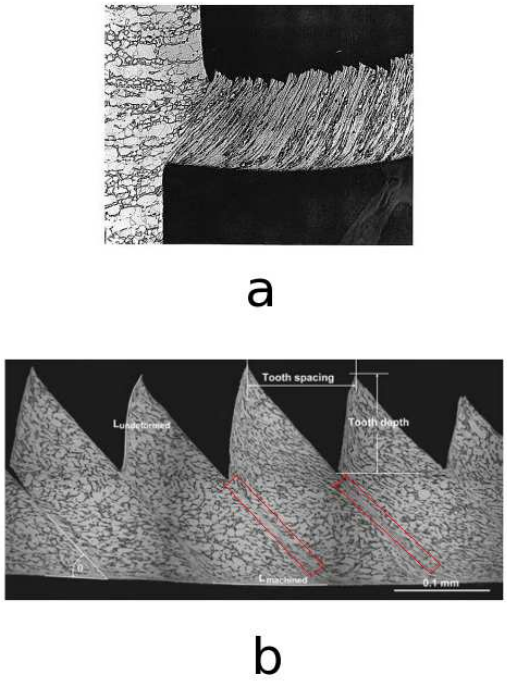

Figure 2.24 *Cross section of (a) a continuous chip and (Image by Trent and Wright [35].) and (b) a segmented chip (Image by Majumdar and Manna [36]). The workpiece can be seen in (a) on the left of the image while the workpiece in (b) would be located to the right if the image if the chip was still connected to the workpiece. The cutting tools were applied from below in each image and moved towards the top of each image. The chip can be seen running perpendicular to the workpiece in (a) and the flow lines on the chip are closely spaced shear bands. Shear bands run through the chip in (b) continuing in the direction of the diagonal edge of the 'teeth' on the chip. Two shear bands are highlighted by the red frames in the image.*

of a compressed micropillar of a Ti alloy in figure 2.26. Micropillar compression experiments can therefore be used to determine favoured slip planes in different metals. This is particularly useful for bcc alloys in which a large degree of cross slip is observed, as the full slip path can be observed in compressed micropillars [41].

Micropillar compression experiments typically involve pillars with diameters between 100 nm and 10 μm in size[42, 43]. Typical strain rates applied to the pillars are between 10^{-6} s^{-1} and 10^{-3} s^{-1} [42, 44]. Many commercial indentation apparatuses are now available. Indenters can generally operate in two modes, load control and displacement control [45, 46]. Using load control involves applying a fixed force to the top of the pillar and observing the plastic strain response to

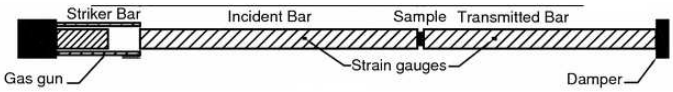

a

b

Figure 2.25 *(a) Schematic of Hopkinson-split bar apparatus. (Image from Dai et al [39]). (b) The Hopkinson-split bar apparatus at Tampere University of Technology. (Courtesy of Tőnu Leemet.)*

this force. In this mode the speed of the indenter is controlled by the plastic yield behaviour of the pillars. The speed of the indenter consequently varies throughout the experiment. Strain control involves moving the indenter at a fixed speed and measuring how the stress on the indenter varies during the experiment. These two indentation modes give rise to distinctive stress vs strain signatures. Under load control, a pillar will deform elastically until the applied force on the pillar is large enough that the plastic yield stress is reached in the pillar. Once the yield stress is reached in the pillar, the pillar deforms plastically until the load is removed. An example of a typical stress vs strain curve for load control can be seen in figure 2.27 (a). In contrast strain control involves moving the indenter at a constant speed. In this mode the pillar is strained elastically until the stress in the pillar reaches the yield stress. The pillar then deforms plastically until the stress returns to a value below the yield stress and the pillar begins to strain elastically again. The result of this is a stress vs strain curve characterised by segments in which the stress increases with strain, separated by sharp drops in the stress as a result of plastic yielding. A typical stress vs strain curve for strain control can be seen in figure 2.27 (b).

In a general sense, micropillars can be used to study mechanical properties and

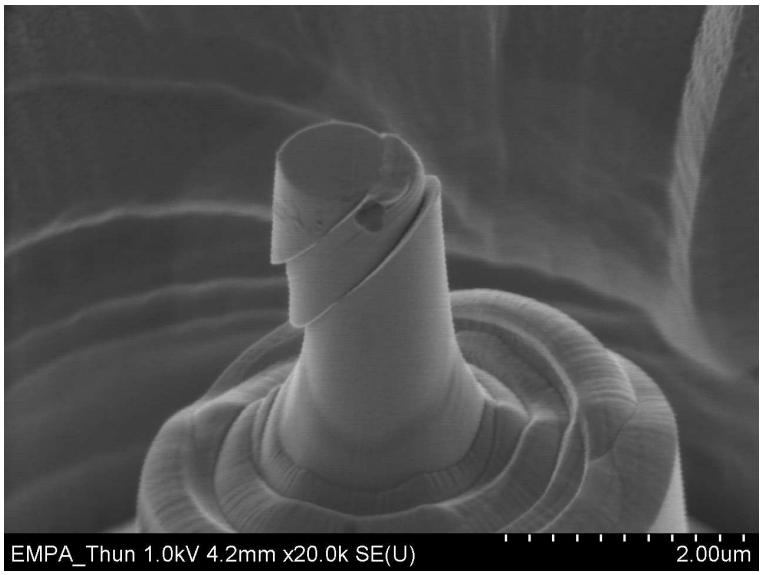

Figure 2.26 *A micropillar of a Ti alloy following compression. The pillar has deformed by dislocation glide and the slip planes are visible.*

plasticity behaviour at micron and nanometre length scales. A large number of interesting results have now emerged from studies of plasticity of micropillars of both fcc and bcc crystals. It has been found, for example, that the strength of micropillars depends on their size and smaller pillars are generally stronger than larger ones [40, 47]. A strain hardening effect has also been observed in micropillars when compressed, with sudden increases in strength occurring intermittently during compression [42, 48]. In load controlled compression tests plastic deformation is found to occur in discrete bursts of strain. The amount of plastic strain occurring in each of these strain bursts is highly variable and appears to occur at random [49]. In addition to these results, a transition from brittle to ductile plasticity behaviour has been found to occur in micropillars of Si and GaAs when the pillar size is below a critical value [50, 51].

The most significant experimental finding from micropillars with respect to this thesis is probably the compression-tension asymmetry reported by Kim and Greer for bcc micropillars of Mo, Nb, Ta, and W [52–54]. The plasticity behaviour was found to be similar for micropillars of these four materials. They found significant differences in the final morphology of bcc micropillars depending on whether tensile or compressive strains were applied. Narrow shear bands were found in compressed pillars indicating that deformation had occurred by slip. Pillars which had been strained in tension deformed by necking and eventually fractured. The atomic scale deformation mechanisms could not be determined

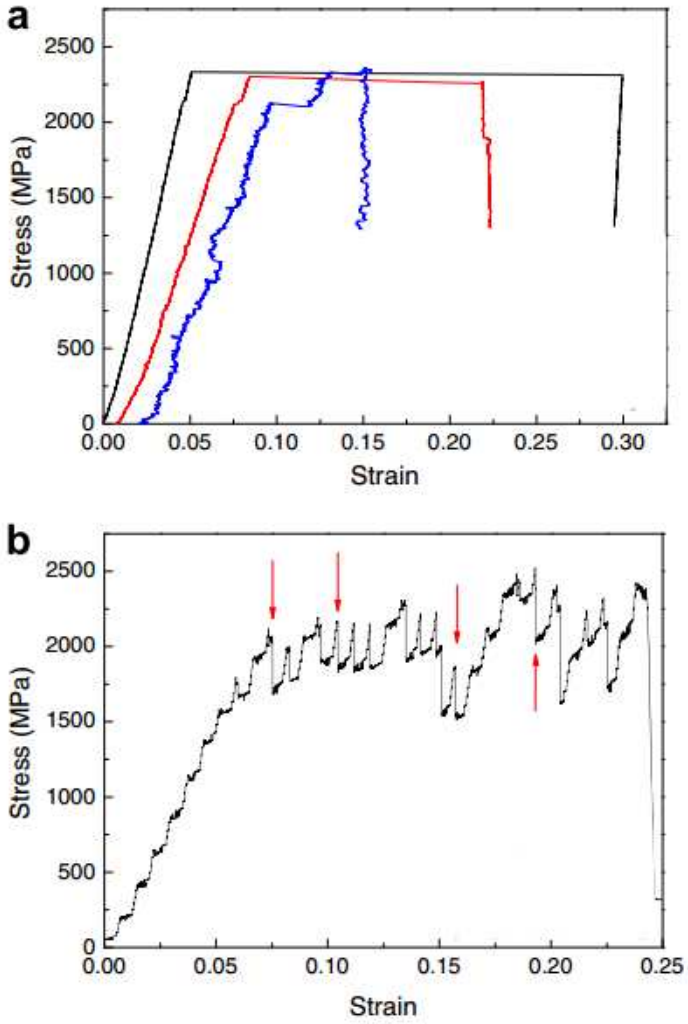

Figure 2.27 *Typical stress vs strain curves for micropillar compression under (a) load control and (b) strain control (Graphs from Dubach et al [46]).*

from this plasticity behaviour and morphology. Figure 2.28 shows the final morphologies for W micropillars following tension and compression. The dynamic plastic response was also different in both cases. In compression plastic strain occurred in discrete strain bursts while plastic strain occurred continuously in the tensile case once the yield stress had been reached. The stress strain curves for tension and compression of the Nb micropillars can be seen in figure 2.29. The twinning-antitwinning slip asymmetry was suggested by Kim and Greer as the reason for the observed tension compression asymmetry [52]. However, this could not be proven definitively as the atomic scale deformation mechanisms could not be determined for the tensile case.

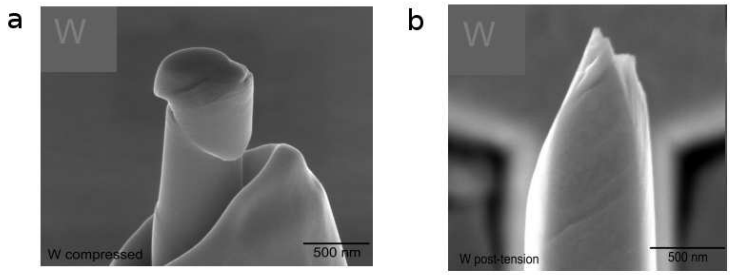

Figure 2.28 *Morphology of W micropillars following compressive straining (left) and tensile straining (right). The compressed pillar contains narrow shear bands indicating that deformation has occurred by slip. The pillar subject to a tensile strain has necked and fractured. The underlying deformation mechanisms in the tensile case cannot be determined from the morphology. (Images by Kim and Greer [52]).*

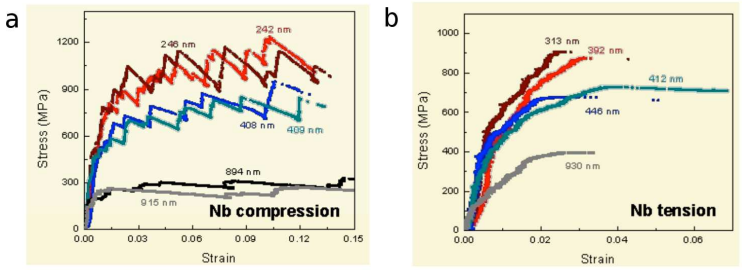

Figure 2.29 *Stress vs strain for Nb micropillars in (a) compression and (b) tension. (From Kim and Greer [52])*

2.8 Modeling and Simulation of Machining Processes

2.8.1 Johnson-Cook constitutive model

The Johnson-Cook material model is an empirical model which describes the stress in a material as a function of strain, strain rate, and temperature [55]. This model is frequently used to describe metals subject to high strains, strain rates, and temperatures. The stress, σ, is expressed as follows.

$$\sigma = (A + B\epsilon^n)\,(1 + C\ln\dot{\epsilon}')\,(1 - T'^m) \tag{2.12}$$

where the quantities $\dot{\epsilon}'$ and T' are defined:

$$\dot{\epsilon}' = \frac{\dot{\epsilon}}{\dot{\epsilon}_0} \tag{2.13}$$

$$T' = \frac{T - T_0}{T_m - T_0} \tag{2.14}$$

Here ϵ denotes strain and hence $\dot{\epsilon}$ is strain rate. Temperature is denoted by T. T_0 and $\dot{\epsilon}_0$ are a reference temperature and strain rate. A, B, C, n, and m are all fitting parameters. The first term in equation 2.12 results in an increasing stress as the strain increases. This term is therefore intended to represent strain hardening in the material. The second term in equation 2.12 results in a hardening effect with increased strain rate and the third term results in a softening effect with increasing temperature. Equation 2.14 implies that the stress goes to zero at the melting temperature.

Fitting parameters are usually determined from the results of Hopkinson-split bar experiments. The parameters are usually found by first performing experiments at the chosen reference temperature and strain rate. In this case the model simplifies to:

$$\sigma = (A + B\epsilon^n) \tag{2.15}$$

Data from these tests is used to fit parameters A, B, and n. Once these parameters have been fitted they are fixed as constants and parameter C and m are fitted by performing the Hopkinson-split bar experiments at a range of strain rates and temperatures.

2.8.2 Finite element modeling

Finite element modeling (FEM) is a simulation technique in which a simulated material is broken up into small elements [56, 57]. FEM simulations can be carried out in two or in three dimensions. The shape of each element is allowed to change under the influence of stresses according to a constitutive model such as the Johnson-Cook model.

The Johnson-Cook model is in fact used commonly as the basis for FEM simulations of chip formation in metals. However, the Johnson-Cook model is based on data from Hopkinson-split bar experiments which only test strain rates up to $10^3 s^{-1}$. In FEM simulations of segmented chip formation strain rates can reach up to $10^6 s^{-1}$ [57] and have been reported by experimentalists to be up to $10^7 s^{-1}$ [34]. This means the the Johnson-Cook model which is empirical in nature is extrapolated over three orders of magnitude in strain rate.

An image of a segmented chip formed in an FEM simulation is shown in figure 2.30.

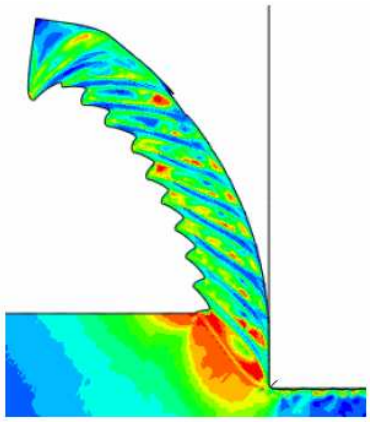

Figure 2.30 *An example of a segmented chip formed during an FEM simulation of high speed cutting. (Courtesy of Aviral Shrot of the MaMiNa collaboration).*

2.9 Summary

In this chapter we have presented some background theory on theory of mechanical deformation in metals. In addition to this we have presented some background on machining and the research undertaken as part of the MaMiNa project to try to develop a free machining Ti alloy. The machining performance of an alloy is dependent on the chip morphology. This morphology is usually predicted by means of FEM simulations. However, the material model on which these FEM simulations are based is typically extrapolated over three orders of magnitude in strain rate. Furthermore the deformation mechanisms which occur in the shear bands, which are subject to high strain rates and temperatures, have not been observed experimentally. As we will see in the following chapters,

molecular dynamics simulations are particularly useful for studying plasticity at high strain rates and at small length scales. Much of the focus of the research within MaMiNa was on bcc alloys of Titanium. Currently it is not possible to simulate a bcc alloy of Titanium due to a lack of necessary potential functions (see next chapter). The results presented in this thesis were from simulations of Iron. Iron was chosen as a model bcc material as it can be reliably simulated using molecular dynamics. In chapter 6 we present simulations of Copper, which was chosen as a model fcc material. The results in fcc Copper nanopillars were acquired in order to provide a contrast with the plasticity behaviour of bcc nanopillars.

Chapter 3

Molecular Dynamics Simulations and Analysis Techniques

3.1 Introduction

Molecular dynamics is an atomic scale simulation technique in which systems of atoms are represented as classical particles moving in a dynamically evolving potential energy profile [58]. The potential energy profile is calculated from a classical potential function, $\Phi(\mathbf{r}_{i1}, \mathbf{r}_{i2}, ..., \mathbf{r}_{iN})$, which describes the potential energy of atom i in a system in terms of its position relative to all other atoms in the system. Here $\mathbf{r}_{ij}$ is a vector representing the separation between atoms i and j. This potential function in most cases contains fitting parameters which are fitted so that systems simulated using the potential represent a real material.

This potential function can be used to calculate the force acting on atom i:

$$\mathbf{F}_i = \nabla\Phi(\sum_j \mathbf{r}_{ij}) \tag{3.1}$$

The acceleration of atom i can be calculated from Newton's second law:

$$\mathbf{a}_i = \mathbf{F}_i/m_i = \frac{\mathrm{d}^2\mathbf{r}_i}{\mathrm{d}t^2} \tag{3.2}$$

Given the positions and velocities of a system of atoms, over a short timestep, Δt, this equation of motion can be integrated to calculate the new positions of atoms in the system at a time $t + \Delta t$.

The basic algorithm is as follows:

1. Calculate forces on each atom based on the potential function.
2. Integrate the equations of motion to calculate the positions and velocities of the atoms at time $t + \Delta t$. Now repeat from step 1.

We can approximate atoms as classical particles as long as the de Broglie thermal wavelength [59], Λ, is small in comparison with the nearest neighbour distance in the system. The de Broglie thermal wavelength is:

$$\Lambda = \sqrt{\frac{2\pi\hbar^2}{Mk_BT}} \tag{3.3}$$

where M is the atomic mass and T is the temperature of the system. The classical potential approximation is valid for most materials. It is poor at simulating light atoms such as H and He as well as systems at low temperatures.

3.2 Potentials

3.2.1 Lennard-Jones

A simple form form for $\Phi(\mathbf{r}_{i1}, \mathbf{r}_{i2}, ..., \mathbf{r}_{iN})$ is one in which the function is a sum of pairwise terms as follows:

$$\Phi(r) = \sum_i \sum_{j \neq i} \phi(|\mathbf{r}_{ij}|) \tag{3.4}$$

The Lennard-Jones potential [58] is a simple pairwise potential in which the pairwise term is:

$$\phi_{LJ}(r) = 4\varepsilon \left[\left(\frac{\sigma}{r}\right)^{12} + \left(\frac{\sigma}{r}\right)^{6} \right] \tag{3.5}$$

A plot of this potential can be seen in figure 3.1. At short interatomic distances, r, the potential is repulsive as the first term, which is proportional to $1/r^{12}$, in equation 3.5 dominates. For large interatomic distances the second term (proportional to $1/r^6$) dominates and the resulting force is attractive.

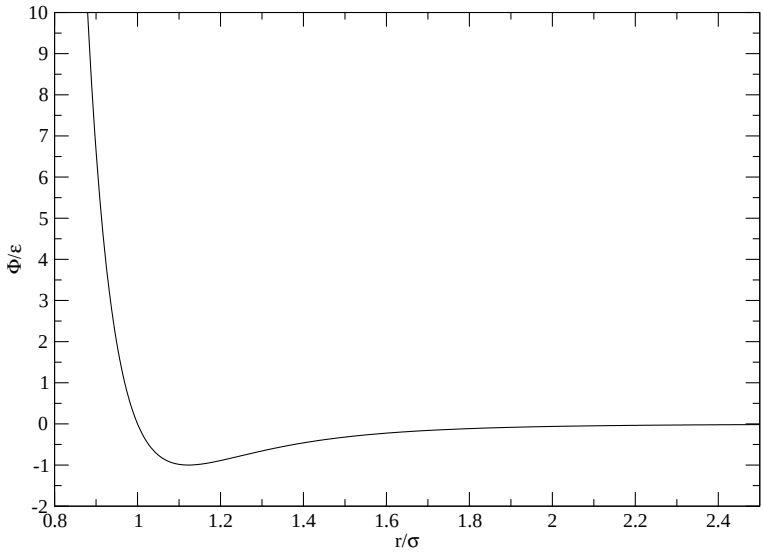

Figure 3.1 *The Lennard-Jones Potential.*

The potential was designed to be highly repulsive at short distances to mimic the repulsive forces experienced by atoms when their electron clouds begin to overlap. The motivation for the use of an exponent of 12 was purely practical. It was simply chosen to create a sudden rise in the repulsion as the interatomic distance became smaller. The exact form of the repulsive term does not have a physical basis.

The attractive (proportional to $1/r^6$) term was chosen to represent the van der Waals interaction. Van der Waals interactions are the dominant attractive interactions for closed shell atoms such as Ar and Kr. It is these kinds of atoms which the Lennard-Jones potential is most effective at representing. The potential can be set to mimic these materials by fitting the parameters σ and ε to the material properties.

As we will discuss in the next section, Lennard-Jones potentials cannot accurately represent materials where there is covalent or metallic bonding (i.e. whenever electrons in the solid move away from their atoms significantly). However, the Lennard-Jones potential is widely used in studies where representing a specific material is not important. The properties of Lennard-Jones systems in a variety of states have been studied extensively making the potential ideal for the creation of model systems for non material specific investigations.

3.2.2 Finnis Sinclair and Embedded Atom Type Potentials

To model metals, one needs potentials which are fit to material parameters for the given metal. The Lennard-Jones potential has only two parameters to fit which makes it an inappropriate functional form for this purpose. Furthermore, there are properties of a Lennard-Jones solid which are not true in general for metals. Consider for example the elastic constants of a metal. The elastic response of a cubic crystal, for small strains, can be described by three elastic constants; C_{11}, C_{12}, and C_{44} [60]. All pairwise potentials obey the Cauchy relation, namely that $C_{12} = C_{44}$. This is generally not the case for metals. In addition to this, the vacancy formation energy, E_v, is always equal to the cohesive energy, E_c, for pairwise potentials. Consider the number of nearest neighbour atoms a given atom in a crystal has. This number is known as the coordination number of an atom. If the coordination number of a crystalline solid is N, then the E_v is the energy cost of decreasing the coordination number of N atoms from N to $N-1$. E_c is the energy cost of reducing the coordination of a single atom from N to 0. In metals the measured value of the fraction $\frac{E_v}{E_c}$ is between $\frac{1}{4}$ and $\frac{1}{3}$. It is clear that cohesion in metals is fundamentally different from that described by a pair potential. When a vacancy is formed, the contribution to the total cohesive energy from some pairs of atoms must increase. This suggests that when a vacancy is formed, bonding between atoms becomes stronger in the region around the vacancy.

One can represent this effect by constructing a potential which consists of two parts. The internal energy of a collection of N atoms located at a set of points $\{R_{ij}\}$ is:

$$U_{tot} = U_N + U_P \tag{3.6}$$

where U_P is a sum of repulsive pairwise terms representing core repulsion. U_N is a sum of short ranged non-pairwise terms which only depend on distances between neighbouring pairs of atoms. This function represents bonding between neighbouring atoms. U_P and U_N are described as follows:

$$U_P = \frac{1}{2}\sum_{ij}\Phi(r_{ij}) \tag{3.7}$$

$$U_N = -\sum_i F(\rho_i) \tag{3.8}$$

$$\rho_i = \sum_j \phi(R_{ij}) \tag{3.9}$$

Here $\phi(R_{ij})$ is a short ranged decreasing function of interatomic distance. $\Phi(r_{ij})$ is a pairwise function representing core repulsion. $\Phi(r_{ij})$, $F(\rho_i)$, and $\phi(R_{ij})$ are functions to be fitted empirically. Note that if $F(\rho_i)$ is a linear function, the potential becomes a pairwise potential. As long as $F(\rho_i)$ is not a linear function, the potential will be non-pairwise allowing for the Cauchy relation to be broken and for the vacancy formation energy and cohesive energy to differ. The fact that $\phi(R_{ij})$ is a short ranged function means that the contribution to U_N from each atom will depend on the coordination of that atom, as $\phi(R_{ij})$ will only be non-zero for interactions between neighbouring atoms. The function $F(\rho_i)$ is chosen as a monotonically increasing function of coordination for each atom. The magnitude of the change in $F(\rho_i)$ when the coordination increases by one decreases as the coordination increases. This makes the vacancy formation energy less than the cohesive energy as required.

There are many different physical interpretations for potentials of this kind. The two most commonly cited are that by Finnis and Sinclair [61] and another by Daw and Baskes [62].

The Finnis interpretation is based on the tight binding model. In this interpretation, U_N is a band energy which results in bonding. U_P is a repulsive interaction between atomic cores consisting of nuclei and valence electrons. Finnis chose $F(\rho_i)$ to be $\sqrt{\rho_i}$ as this comes from the second moment tight binding approximation [63, 64].

The Daw and Baskes interpretation is known as the embedded atom method. In this interpretation U_N is the energy change one gets from placing an atom in a uniform electron gas. In this case, U_P is again a repulsive interaction between cores. $F(\rho)$ is an embedding function representing the energy due to embedding an atom in an electron gas of density ρ. The charge density at site i is given by ρ_i and this is calculated from a superposition of the atomic charge densities, ϕ, from atoms within a short range of the atom in question.

Both of these interpretations result in a similar functional form for the potential.

The only difference being that $F(\rho_i)$ was set as $\sqrt{\rho_i}$ in the Finnis interpretation and was kept as a function to be fitted in the Daw and Baskes interpretation. To develop potentials representing real materials, the functions are fitted to real material parameters (for example melting temperature, thermal expansion coefficients, and elastic constants).

In this thesis we will make use of a potential for Iron developed by Ackland and others [65]. In this potential the fitting was implemented by using a polynomial spline functional form for the functions $\Phi(r)$ and $\phi(r)$. The repulsive interaction, $\Phi(r)$ incorporates the screened electrostatic potential of Biersack and Ziegler [66] for extremely short ranged interactions (i.e. where r is less than 2.05 Å). The full form of this interaction is given by:

$$\Phi_{Fe}(r) = \sum_{k=1}^{13} a_k (r - r_k)^{n_k} H(r_k - r) H(r - r_2) \tag{3.10}$$

Here $H(x)$ is the Heaviside step function and r_k represent cutoff radii for each term in the function. Note that if $i > j$ then $r_i > r_j$.

The short ranged bonding interaction functions for this potential are:

$$\phi_{Fe}(r) = \sum_{k=1}^{3} A_k (R_k - r)^3 H(R_k - r) \tag{3.11}$$

$$F_{Fe}(\rho) = -\sqrt{\rho} + a_2\rho^2 + a_4\rho^4 \tag{3.12}$$

It should be noted that for interatomic distances shorter than 2.05Å this potential function has a different functional form. However, interatomic distances this small were never encountered in the simulations described in this thesis. The details of this part of the potential are therefore omitted here for simplicity. Full details of this potential can be found in ref [65].

A potential for Copper is also utilised in this thesis. This potential was developed by Ackland *et al* [67]. This potential uses a square root function for $F(\rho)$ as in the original Finnis Sinclair potential. Like the Fe potential, the functions $\Phi(r)$ and $\phi(r)$ are fitted using polynomial spline functions although fewer cutoff radii

are used. The functions are:

$$\Phi_{Cu}(r) = \sum_{k=1}^{6} a_k (r - r_k)^3 H(r_k - r) \tag{3.13}$$

$$\phi_{Cu}(r) = \sum_{k=1}^{2} A_k (R_k - r)^3 H(R_k - r) \tag{3.14}$$

Full details of this potential can be found in [67].

3.3 Measurements

Total potential energy in the system is simply calculated from the potential function supplied as described previously.

The total kinetic energy can simply be calculated using:

$$K(t) = \frac{1}{2} \sum_i m_i |\mathbf{v}_i(t)|^2 \tag{3.15}$$

where m_i and $\mathbf{v}_i$ are the mass and velocity of atom i.

Once the kinetic energy is known, the temperature of the system can be calculated from:

$$K = \frac{3}{2} N k_b T \tag{3.16}$$

The pressure can be calculated from a Virial relation as follows:

$$PV = N k_B T + \frac{1}{D} \langle \sum_{i=1}^{N} \mathbf{r}_i \cdot \mathbf{F}_i \rangle \tag{3.17}$$

where D is the number of dimensions in the system. The first term in the above expression represents a thermal contribution to the pressure. This term is the same as the pressure exerted by an ideal gas due to atomic collisions. The second term is a potential energy term which is due to interatomic forces in the system.

A stress tensor can be computed for a system of atoms which is equivalent to

the Cauchy stress tensor in continuum mechanics [68]. The so called virial stress tensor is a 3×3 matrix whose components, $\sigma_{\alpha\beta}$, are given by [69, 70]:

$$\sigma_{\alpha\beta} = \frac{1}{V} \sum_i \left[m_i v_i^\alpha v_i^\beta + \frac{1}{2} \sum_j \left(r_i^\beta - r_j^\beta \mathbf{F}_{ij}^\alpha \right) \right] \tag{3.18}$$

Here α and β represent the x, y, and z directions. V is the volume of the system and F_{ij} is the force on atom i due to atom j. m_i, r_i, and v_i represent respectively the mass, position, and velocity of atom i.

3.4 Integration

The most commonly used integration algorithm in molecular dynamics simulations is the Verlet algorithm [71]. This is the integration algorithm that was used in the simulations presented in this thesis. The algorithm is derived by first expanding the atomic position as a function of time in a third order Taylor expansion. This is expansion is done twice, one forward in time and one backwards. Doing this we have:

$$\mathbf{r}(t + \Delta t) = \mathbf{r}(t) + \mathbf{v}(t)\Delta t + \frac{1}{2}\mathbf{a}(t)\Delta t^2 + \frac{1}{6}\mathbf{b}(t)\Delta t^3 + O(\Delta t^4) \tag{3.19}$$

$$\mathbf{r}(t - \Delta t) = \mathbf{r}(t) - \mathbf{v}(t)\Delta t + \frac{1}{2}\mathbf{a}(t)\Delta t^2 - \frac{1}{6}\mathbf{b}(t)\Delta t^3 + O(\Delta t^4) \tag{3.20}$$

where $\mathbf{v}$ is the atomic velocity, $\mathbf{a}$ is the acceleration, and $\mathbf{b}$ is the third time derivative of the atomic position. Summing these two expressions gives:

$$\mathbf{r}(t + \Delta t) = 2\mathbf{r}(t) - \mathbf{r}(t - \Delta t) + \mathbf{a}(t)\Delta t^2 + O(\Delta t^4) \tag{3.21}$$

This is the original form of the Verlet algorithm. The error function for this algorithm is of order Δt^4. However, velocities are not explicitly calculated during this process. Velocities must be calculated from positions as follows:

$$\mathbf{v}(t) = \frac{\mathbf{r}(t + \Delta t) - \mathbf{r}(t - \Delta t)}{2\Delta t} \tag{3.22}$$

However the error for this calculation will be of order Δt^2. This problem is averted by using the velocity Verlet algorithm. In this algorithm, the velocity at time $t + \Delta t$ is calculated by integrating twice over a timestep of $\Delta t/2$. The algorithm is implemented via the following steps:

1. First calculate the positions of each atom at time $t + \Delta t$ by the expression:

$$\mathbf{r}(t + \Delta t) = \mathbf{r}(t) + \mathbf{v}(t)\Delta t + \frac{1}{2}\mathbf{a}(t)\Delta t^2 \tag{3.23}$$

2. The velocities at time $t + \Delta t/2$ are then calculated:

$$\mathbf{v}(t + \Delta t/2) = \mathbf{v}(t) + \frac{1}{2}\mathbf{a}(t)\Delta t \tag{3.24}$$

3. The accelerations on all atoms are then calculated at time $t + \Delta t$ using the potential function.

4. Now velocities are computed at the new at time $t + \Delta t$:

$$\mathbf{v}(t + \Delta t) = \mathbf{v}(t + \Delta t/2) + \frac{1}{2}\mathbf{a}(t + \Delta t)\Delta t \tag{3.25}$$

This integration algorithm is time reversible and therefore conserves the energy of the system very well.

3.5 Boundary Conditions

One must choose conditions at the boundaries of a simulated system. The simplest solution is to create surfaces at the system boundaries. However, molecular dynamics systems are small and consequently will have a large surface to volume ratio. This will result in surface energy and relaxation in the system which is not always desirable.

To represent a continuous system which behaves similarly to a bulk solid or liquid, one can implement periodic boundary conditions [58]. In this technique, the system is effectively replicated and translated in all three cartesian directions to fill all space. Consider a system of atoms located inside a parallelepiped, the edges of which are described by three vectors; **a**, **b**, and **c**. Periodic boundary conditions are imposed by replicating atoms in the system periodically. For any

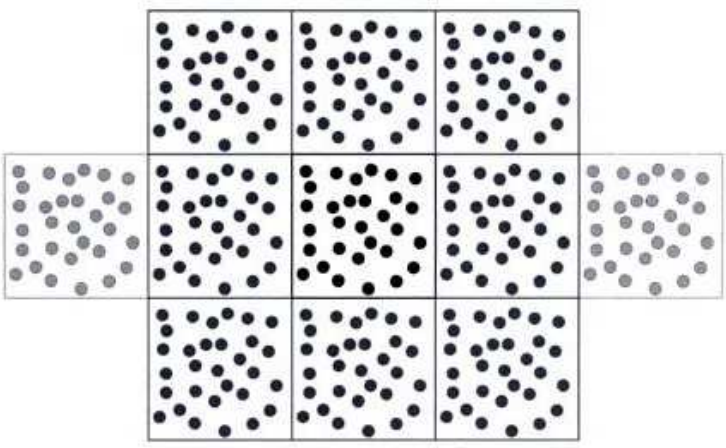

Figure 3.2 *Image illustrating periodic boundary conditions in two dimensions. Image taken from [58]*

atom located at $\mathbf{r}$ in the system, the atom is replicated at locations , $\mathbf{r}_{lmn}$, given by:

$$\mathbf{r}_{lmn} = \mathbf{r} + l\mathbf{a} + m\mathbf{b} + n\mathbf{c} \tag{3.26}$$

where l, m, and n are integers in the range $\{-\infty, \infty\}$. There are now no physical boundaries in the system and when an atom leaves the central cell, one of its images will enter the cell at the opposite side. An illustration of periodic boundary conditions in two dimensions can be seen in figure 3.2.

If the potential function used is infinite ranged, then the number of pair interactions becomes infinite as any atom, i, in the simulated system will interact with an infinite number of images of another atom, j, in the central cell. To avoid having to compute an infinite number of atomic pair interactions, the following condition is implemented. Consider an atom, i, in the central cell. For each atom j (where $j \neq i$), atom i only interacts with one atom in the set $\{j, j_1, j_2, j_3, \dots\}$, where $j_1, j_2, j_3, \dots$ are periodic images of atom j. Out of the set $\{j, j_1, j_2, j_3, \dots\}$, i interacts with the atom or image which it is closest to. This is known as the minimum image criterion. This criterion is often implemented by simply using a truncated or short ranged potential function with a limited range R_c. As long as one is using a truncated potential and a square cell of length L, then the minimum image criterion is exact if $R_c < L/2$. Note that many types of potential function have infinite range in theory. The Lennard-Jones potential, for example, is infinitely ranged and the part of Finnis Sinclair potentials representing core interactions is, in theory, infinitely ranged. In both these cases the value of the

function becomes negligible at large interatomic distances. These potentials are typically truncated when implemented in code to allow for periodic boundary conditions to be imposed. For the simulations presented in this thesis, truncated Finnis Sinclair potentials were used.

3.6 Ensembles and Thermostats

Molecular dynamics simulations implement the NVEp ensemble by default. This differs from slightly from the microcanonical ensemble as momentum (p) in the system is also conserved. To run a simulation in a different ensemble, additional degrees of freedom can be introduced which are coupled to the real system. The equations of motion for these extended systems can be derived from extended Lagrangians.

3.6.1 NVTp Ensemble

Constant temperature can be achieved in molecular dynamics by implementing a Nosé-Hoover Thermostat [72, 73]. Implementing this will produce the same conservation laws as the canonical ensemble. In this ensemble the number of atoms in the system is conserved as is the volume, temperature, and total momentum of the system. The thermostat is implemented by introducing an additional degree of freedom, s, into the system. The interaction between the physical system and the virtual degree of freedom, s, can be reduced to a rescaling of the real time variable t' to a virtual time variable, t:

$$dt = s(t')dt' \tag{3.27}$$

The virtual variables t, $\mathbf{r}_i$, and $\mathbf{p}_i$ are then related to real variables t, $\mathbf{r}_i$, and $\mathbf{p}_i$ as follows:

$$\mathbf{r}'_i = \mathbf{r}_i \tag{3.28}$$

$$\mathbf{p}'_i = \frac{\mathbf{p}_i}{s} \tag{3.29}$$

$$t' = \int^t \frac{dt}{s} \tag{3.30}$$

The following Lagrangian is then proposed for the system:

$$L = \frac{1}{2}\sum_i^N m_i s^2 \dot{\mathbf{r}}_i' - \Phi(\mathbf{r}) + \frac{Q}{2}\dot{s}^2 + gkT\ln s \tag{3.31}$$

Here Q is a parameter with units of energy$\times$(time)^2 which acts like an effective mass for the degree of freedom s. The number of degrees of freedom in the system is g, T is an externally set temperature, and k is Boltzmann's constant. We can now derive the equations of motion for this Lagrangian using the Lagrangian equation:

$$\frac{\mathrm{d}}{\mathrm{d}x}\left(\frac{\partial L}{\partial \dot{A}}\right) = \frac{\partial L}{\partial A'} \tag{3.32}$$

We then obtain the equations of motion:

$$\ddot{\mathbf{r}} = -\frac{1}{m_i s^2}\frac{\partial \Phi}{\partial \mathbf{r}_i} - \frac{2\dot{s}}{s}\dot{\mathbf{r}}_i \tag{3.33}$$

$$Q\ddot{s} = \sum_i^N m_i s \dot{\mathbf{r}}_i{}^2 - \frac{gkT}{s} \tag{3.34}$$

This system can be shown to produce the same conservation laws as the canonical ensemble [72, 73]. Momentum is also conserved using this thermostat. The Hamiltonian for this system is given by:

$$\mathscr{H} = \sum_i^N \frac{\mathbf{p}_i^2}{2m_i s^2} + \Phi(\mathbf{r}) + \frac{p_s^2}{2Q} + gkT\ln s \tag{3.35}$$

The variable s was interpreted by Nosé as a time-scaling variable. Hoover switched back to real time by replacing $\mathbf{p}_i$ in equation 3.35 with $s\mathbf{p}_i$ [72]. By introducing the variable $\xi = p_s/Q$, he eliminated the variable s from the equations

of motion. Hoovers equations of motion were:

$$\dot{\mathbf{p}}_i = \mathbf{F}_i - \xi \mathbf{p}_i \tag{3.36}$$

$$\dot{\xi} = \frac{2}{Q}\left(\frac{\mathbf{p}_i^2}{2m_i} - \frac{gkT}{2}\right) \tag{3.37}$$

The alteration to the dynamics of the real system depends on the thermostat variable, ξ, and the dynamics of ξ depends on the difference between the current system kinetic energy and the desired system kinetic energy. Rewriting equation 3.36 in terms of velocity rather than momentum, we get:

$$\dot{\mathbf{v}}_i = \frac{\mathbf{F}_i}{m_i} - \xi \mathbf{v}_i \tag{3.38}$$

At each time step in a simulation, the following calculation must be performed by numerical integration:

$$\mathbf{v}_i(t+\Delta t) = \mathbf{v}_i(t) + \int_t^{t+\Delta t} \frac{\mathbf{F}_i}{m_i} \mathrm{d}t - \int_t^{t+\Delta t} -\xi \mathbf{v}_i \mathrm{d}t \tag{3.39}$$

This is easy to implement in existing molecular dynamics codes as the first integral on the right hand side of equation 3.39 is the integral which is calculated in a molecular dynamics simulation without a thermostat. To implement the Nosé-Hoover Thermostat, the volocities can simply be adjusted at each time step by adding a term, $\Delta \mathbf{v}_i^{Nose}$, to the velocity of each particle in the system. This term, $\Delta \mathbf{v}_i^{Nose}$, is simply the second integral term in equation 3.39:

$$\Delta \mathbf{v}_i^{Nose} = -\int_t^{t+\Delta t} \xi \mathbf{v}_i \mathrm{d}t \tag{3.40}$$

The simulations presented in this thesis were performed using the MOLDY molecular dynamics code (see section 3.7). In this code, the integral in equation 3.40 was calculated using the Euler method. The velocity adjustment operation in the code at each tome step can therefore be represented as:

$$\mathbf{v}_i^{adjusted}(t) = \mathbf{v}_i(t) + \xi \mathbf{v}_i(t) \Delta t \tag{3.41}$$

where $\mathbf{v}_i^{adjusted}(t)$ represents the velocity of particle i after its velocity has been

adjusted by adding $\Delta \mathbf{v}_i^{Nose}$ for the given time step. The equation of motion for the thermostat variable, ξ, is also integrated using the Euler method in MOLDY. At each time step the following calculation is performed:

$$\xi(t + \Delta t) = \xi(t) + \dot{\xi}\Delta t \tag{3.42}$$

where $\dot{\xi}$ is simply calculated from equation 3.37.

The NVTp ensemble was used for most of the calculations reported in this thesis. Whenever simulations are carried out at constant volume with a Nosé-Hoover Thermostat implemented to preserve temperature, the simulation is carried out in the NVTp ensemble.

3.6.2 NPEp and NPTp Ensembles

The Parrinello-Rahman method [74] can be used to create an NPEp ensemble, in which the total number of atoms in the system, the pressure, the total energy, and the total momentum of the system are conserved. When used in combination with a Nosé-Hoover Thermostat, an NPTp ensemble is produced, in which the number of atoms in the system is conserved as well as the pressure, temperature, and total momentum of the system.

In this method we write the positions of all atoms in terms of fractional coordinates α_i, β_i, and γ_i. The system cell containing the atoms is a parallelepiped defined by three vectors $\mathbf{a}$, $\mathbf{b}$, and $\mathbf{c}$. The real space coordinates of the atoms are then given by:

$$\mathbf{r}_i = \alpha_i \mathbf{a} + \beta_i \mathbf{b} + \gamma_i \mathbf{c} \tag{3.43}$$

If we now define a boxmatrix, h, given by $h = [\mathbf{a}, \mathbf{b}, \mathbf{c}]$, and a fractional coordinate vector $\mathbf{s}_i = (\alpha_i, \beta_i, \gamma_i)$, the above relation simplifies to:

$$\mathbf{r}_i = h\mathbf{s}_i \tag{3.44}$$

The 9 variables which make up the matrix h are now treated as additional degrees

of freedom. The following Lagrangian is now proposed:

$$L = \frac{1}{2}\sum_{i=1}^{N} m_i \dot{\mathbf{s}}_i' h' h \dot{\mathbf{s}}_i - \sum_{i=1}^{N} \Phi_i(\{\mathbf{r}_j\}) + \frac{1}{2} W Tr \dot{h}' \dot{h} - PV \tag{3.45}$$

where P is the hydrostatic pressure and V is the volume of the system. Here Φ_i is the potential energy of atom i and it is a funtion of the set of the set of all atomic positions which is denoted $\{\mathbf{r}_j\}$. h' and $\mathbf{s}'$ denote the transposes of h and $\mathbf{s}$ respectively. From this we can use the Lagrangian equation to get the following equations of motion:

$$\ddot{\mathbf{s}}_i = -\sum_{j \neq i} m_i^{-1} \left(\frac{1}{r_{ij}} \frac{\mathrm{d}\Phi_i(\{\mathbf{r}_j\})}{\mathrm{d}r_{ij}} \right) (\mathbf{s}_i - \mathbf{s}_j) - \mathbf{G}^{-1} \dot{\mathbf{G}} \dot{\mathbf{s}}_i \tag{3.46}$$

$$W \ddot{h} = (\Pi - P) V h'^{-1} \tag{3.47}$$

Here Π is a matrix whose components, $\Pi_{\alpha\beta}$, are given by:

$$V \Pi_{\alpha\beta} = \sum_i m_i v_{i,\alpha} v_{i,\beta} - \frac{\partial \Phi}{\partial h_{\alpha\delta}} h'_{\delta\beta} \tag{3.48}$$

where $\mathbf{G} = h'h$. Here $v_{i,\alpha}$ and $v_{i,\beta}$ are components of the velocity of particle i and thus:

$$v_{i,\alpha} = h_{\alpha,\delta} \dot{s}_{i,\delta} \tag{3.49}$$

where $\dot{s}_{i,\delta}$ is the δ component of the $\dot{\mathbf{s}}$ vector. Note that in the last two equations we have assumed the convention of implicit summation over repeated indices.

The Hamiltonian for this system is:

$$\mathscr{H} = \frac{1}{2}\sum_{i=1}^{N} m_i \dot{\mathbf{s}}_i' h' h \dot{\mathbf{s}}_i + \sum_{i=1}^{N}\sum_{j>i}^{N} \Phi(r_{ij}) + \frac{1}{2} W \mathrm{Tr} \dot{h}' \dot{h} + PV \tag{3.50}$$

At temperature, T, the term containing W contributes just $9/2k_BT$ to the total Hamiltonian while the the atomic degrees of freedom contribute $3N/2k_BT$. The

W term is therefore negligible and the Hamiltonian can be approximated as the enthalpy of the system:

$$\mathscr{H} \approx H = E + PV \tag{3.51}$$

In the MOLDY code, the equations of motion (i.e. equations 3.46 and 3.47) are integrated using the velocity Verlet algorithm described in section 3.4. The variables $\mathbf{s}_i$ and $\dot{\mathbf{s}}_i$ are calculated via the following steps:

1. Values of $\dot{\mathbf{s}}_i$ at time $t + \Delta t$ are then calculated:

$$\mathbf{s}_i(t + \Delta t) = \mathbf{s}_i(t) + \dot{\mathbf{s}}_i(t)\Delta t + \frac{1}{2}\ddot{\mathbf{s}}_i(t)\Delta t^2 \tag{3.52}$$

2. The values of $\dot{\mathbf{s}}_i$ at time $t + \Delta t/2$ are calculated:

$$\mathbf{s}_i(t + \Delta t/2) = \dot{\mathbf{s}}_i(t) + \frac{1}{2}\mathbf{a}(t)\Delta t \tag{3.53}$$

3. For each atom $\ddot{\mathbf{s}}_i$ is calculated at time $t + \Delta t$ using equation 3.46.

4. The values of $\dot{\mathbf{s}}_i(t + \Delta t)$ are then calculated:

$$\dot{\mathbf{s}}_i(t + \Delta t) = \dot{\mathbf{s}}_i(t + \Delta t/2) + \frac{1}{2}\ddot{\mathbf{s}}_i(t + \Delta t)\Delta t \tag{3.54}$$

The time evolution of the components of the boxmatrix, h, are computed in the same manner with equation 3.47 used in step 3 to compute $\ddot{h}$.

For the work presented in this thesis, the NPTp ensemble was occasionally used to allow systems to relax to their equilibrium volume and shape at a given temperature. Whenever a simulation is carried out at constant pressure and a Nosé-Hoover Thermostat is used to preserve temperature, then the simulation is carried out in the NPTp ensemble.

3.7 Software

Many different molecular dynamics software packages now exist for simulating large systems. Some commonly used codes include LAMMPS and DL_POLY.

These codes are general purpose and are parallelised with MPI for use on distributed memory multicore machines.

In this thesis we use the MOLDY molecular dynamics program developed by Ackland *et al* [75]. MOLDY has been developed specifically for the purpose of simulating metals using Finnis Sinclair potentials or the embedded atom method type potentials developed by Daw and Baskes. The code is written in Fortran and is parallelised using OpenMP. This allows the code to run in parallel on a shared memory multicore machine.

A number of imaging and analysis software packages were also used in this thesis. The software used included BallViewer[76], Atomeye[77], and Ovito[78].

BallViewer is a software package specifically designed to read and image output files from MOLDY. Ackland-Jones analysis (see section 3.8.1) is built in to the software allowing for crystalline structures to be identified in the display. The system can be rotated and viewed with or without perspective. BallViewer is written in Java and can be downloaded as a jar file for use on multiple platforms.

Atomeye is a widely used imaging package developed by Ju Li. Centrosymmetry analysis is built in to the code allowing defects to be viewed easily. The package can run on most UNIX platforms and it is capable of rendering systems larger than a million atoms in size with little loss in performance.

Ovito is another imaging package developed by Alexander Stukowski. The package features a wide range of analysis tools including centrosymmetry analysis and Ackland-Jones structure identification. Ovito can also be used to create vector displacement maps displaying vector displacements of individual atoms between different points in a simulation. Ovito can read a large number of input file formats including LAMMPS dump files. The software can be downloaded for both Windows and Linux platforms.

3.8 Analysis Techniques

Here we present a list of techniques used in this thesis for the analyses of crystalline molecular dynamics samples. Such analyses techniques are usually used to produce visualisations which illustrate clearly defects, deformation mechanisms, and structural features in a sample. There are many practical details

to consider when creating an effective visualisation which clearly demonstrates the features of the system which you are trying to reveal. Certain software packages and analysis algorithms can take a long time to implement when using large samples. In addition to this subtle differences in analysis techniques and in the graphical features of the various software packages can result in significant differences in the quality of the visualisation. For these reasons a variety of different analysis techniques are used in this thesis.

3.8.1 Ackland-Jones Crystal Identification Method

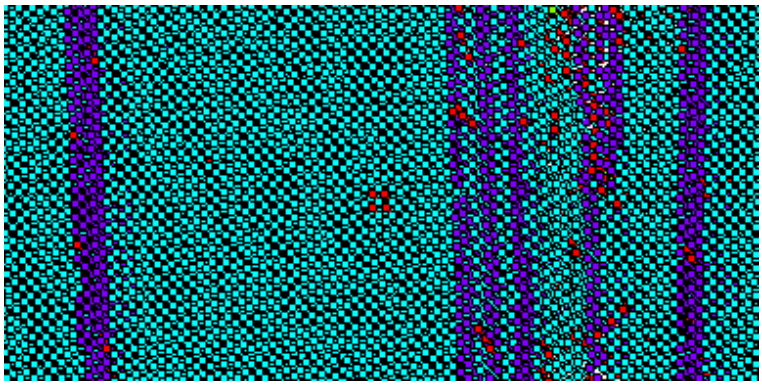

Figure 3.3 ⟨111⟩ *stacking faults in fcc Cu. Since the local stacking sequence changes, stacking fault planes are identified as hcp by the Ackland-Jones method. Here blue atoms are fcc and purple atoms are hcp. Red atoms are those which cannot be assigned a crystal structure as they are bordering vacancies.*

The method of crystal identification developed by Ackland and Jones [76] is an heuristic algorithm which can distinguish hcp, fcc, and bcc structures in an MD system. The algorithm is based on near neighbour characteristics as well as the angular distribution functions for different crystal structures. Although the samples analysed in this thesis are mostly of a single crystal structure, the Ackland-Jones method was used to detect defect atoms which generally are not assigned a crystal structure. The Ackland-Jones method can also be used to clearly distinguish amorphous regions from crystalline regions in a sample. This analysis can easily be applied to a sample using the BallViewer visualisation software.

The angular distribution function is a frequency distribution of the cosine of angles formed by an atom, i, and any two of its nearest neighbours, j and k.

Table 3.1 *Table illustrating the bins of* $\cos\theta_{ijk}$ *used during the analysis. The populations of each bin,* χ_l*, for ideal crystals of bcc, fcc, and hcp are shown where* $r_{ij}^2, r_{jk}^2 < 1.45r_0^2$*. Data taken from [76]*

bin no. (l)	lower bound ($\cos\theta_{ijk}$)	upper bound ($\cos\theta_{ijk}$)	χ_l for ideal crystal		
			bcc	fcc	hcp
0	-1.0	-0.945	7	6	3
1	-0.945	-0.915	0	0	0
2	-0.915	-0.755	0	0	6
3	-0.755	-0.705	36	24	21
4	-0.195	0.195	12	12	12
5	0.195	0.245	0	0	0
6	0.245	0.795	36	24	24
7	0.795	1.0	0	0	0

The angle cosine formed by these three atoms is then denoted θ_{ijk}. The range of $\cos\theta_{ijk}$ is now divided into eight bins labelled by a number, l, which runs from 0 to 7. The fact that the range of $\cos\theta_{ijk}$ is divided into this many bins has no apparent physical significance. It is an heuristic feature of the algorithm. The number of atom combinations whose value of $\cos\theta_{ijk}$ falls into each bin is denoted χ_l. The values of χ_i for ideal lattices are summarised in table 3.1

The following indices are also used to distinguish different structures:

$$\delta_{bcc} = \frac{0.35\chi_4}{\chi_5 + \chi_6 + \chi_7 - \chi_4} \tag{3.55}$$

$$\delta_{CP} = 0.61|1 - \frac{\chi_6}{24}| \tag{3.56}$$

$$\delta_{fcc} = 0.61\frac{|\chi_0 + \chi_1 - 6| + \chi_2}{6} \tag{3.57}$$

$$\delta_{hcp} = \frac{1}{12}(|\chi_0 - 3| + |\chi_0 + \chi_1 + \chi_2 + \chi_3 - 9|) \tag{3.58}$$

The algorithm is then summarised as follows:

1. Calculate mean squared separation, r_0^2, for six nearest atoms to i, where:

$$r_0^2 = \sum_{j=1}^{6} \frac{r_{ij}^2}{6} \tag{3.59}$$

2. Find N_0 near neighbours for which $r_{ij}^2 < 1.45 r_0^2$ and N_1 neighbours for which $r_{ij}^2 < 1.55 r_0^2$.

3. Calculate $\cos\theta_{jik}$ for all combinations of atom i with near neighbours j and k. There are $\frac{N_0(N_0-1)}{2}$ different combinations.

4. Find χ_i from reference table 3.1 using $\cos\theta_{jik}$ data.

5. If $N_0 < 11$ or if $\chi_0 > 0$ then structure of atom i is unassigned.

6. If $\chi_0 = 7$ atom is bcc. If $\chi_0 = 6$ atom is fcc. If $\chi_0 = 3$ atom is hcp.

7. Calculate δ_{bcc}, δ_{CP}, δ_{fcc}, and δ_{hcp}.

8. If none of these δ values are less than 0.1 then the structure is unassigned.

9. If $\delta_{bcc} < \delta_{CP}$ and $10 < N_1 < 13$ then the atom is assigned a bcc structure.

10. If $N_0 > 12$ then the structure is unassigned. If $N_0 \leq 12$ then the structure is hcp if $\delta_{hcp} < \delta_{fcc}$ and is fcc if $\delta_{fcc} < \delta_{hcp}$.

Figure 3.3 shows in an image of $\langle 111 \rangle$ stacking faults in fcc Cu. The change in stacking sequence due to these stacking faults mean that the atoms in the stacking fault planes are recognised as hcp atoms.

3.8.2 Neighbour List Comparison

In this thesis we employ neighbour list comparisons to detect slip planes in deformed crystals. This involves collecting lists of nearest neighbour atoms for each atom in the initial undeformed system. Neighbour lists are also collected for the deformed system and the lists are compared. Atoms for which the neighbour list has changed significantly can be recorded in an output file and can be viewed using imaging software. This technique can be used to detect slip planes as when a slip event occurs, the neighbour lists for all atoms on the active slip plane will change. The technique is effective at picking out slip planes in fcc crystals.

However, in bcc crystals it is sometimes difficult to detect slip planes, particularly when the crystal is elastically strained. This is due to the fact that the distance from a given atom in a bcc crystal to one of its nearest neighbours is close to the distance to a second nearest neighbour. As a result of this, thermal motion of atoms and elastic strain fields can cause second nearest neighbours to be detected as one of the nearest neighbours during the neighbour list collection.

Changes in neighbour lists can be used as a general metric of local plasticity. The regions where plastic deformation occurs in a system will generally contain more atoms for which the neighbour list has changed. In the work presented in this thesis, this technique was used to detect slip planes and regions in a a crystal which had turned amorphous during deformation. The technique is easy to use in combination with any visualisation software as it is relatively straightforward to write code which will apply the technique to a simulation output file.

This technique has previously been used by Galloway and Ackland to detect vacancies in radiation damage simulations [79].

3.8.3 Centrosymmetry Parameter

Many crystal structures, such as bcc and fcc, exhibit central symmetry about any atom in the lattice. This means that for every near neighbour of a given atom, there is also a near neighbour located in the exact opposite direction from the central atom. The vectors connecting the central atom to these two near neighbours will sum to zero. This is illustrated in a bcc lattice in figure 3.4. The figure shows two vectors, $\mathbf{a}$ and $\mathbf{b}$, pointing to near neighbours on opposite sides of the central atom. As a consequence of central symmetry $\mathbf{a} + \mathbf{b} = 0$. The centrosymmetry parameter was designed to take advantage of this feature of fcc and bcc crystals. The parameter was constructed so that it would be zero in a crystal with perfect central symmetry and would increase in magnitude when defects are introduced which break the central symmetry of the crystal in a specific region.

The original centrosymmetry parameter, c_i, introduced by Kelchner *et al* [80] is

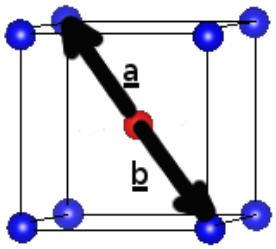

Figure 3.4 *Vectors (**a** and **b**) connecting an atom in a bcc lattice to two of its nearest neighbours. The central atom is coloured red and the near neighbours are black. These vectors point to near neighbours on opposite sides of the central atom. The bcc lattice exhibits central symmetry about any atom in the lattice. As a consequence* $\boldsymbol{a} = -\boldsymbol{b}$*. For each near neighbour of the central atom there is a near neighbour on the opposite side. The vectors connecting the central atom to two such atoms will always sum to zero.*

defined as:

$$c_i = \sum_{j=1}^{N/2} |\mathbf{R}_j + \mathbf{R}_{j+\frac{N}{2}}|^2 \tag{3.60}$$

The parameter is defined for all atoms (indexed by the letter i) in a system. Here the $\mathbf{R}_i$ and $\mathbf{R}_{i+\frac{N}{2}}$ are vectors connecting opposite nearest neighbours in an fcc or bcc lattice and N is the number of nearest neighbours for the crystal structure in question. For a perfect fcc or bcc crystal, the centrosymmetry parameter will be equal to zero. Deviations from central symmetry caused by elastic strain fields, thermal motion of atoms, or defects in the material will result in atoms with non-zero centrosymmetry parameters. There will be a characteristic value for atoms on different types of defects within a specific material. Using imaging software we can display only atoms with centrosymmetry parameters within a specific range or colour atoms according to their centrosymmetry values.

The characteristic values of c_i for various defects in a specific crystal structure will not be the same for different materials. As one can see from equation 3.60, the values of c_i depend not just on the type of defect but also on the lattice constant for the material. We can define a normalised centrosymmetry parameter which will give more or less the same values for a given defect in any material with the

same crystal structure. The normalised centrosymmetry parameter is defined as:

$$c_{n,i} = \frac{\sum_{j=1}^{N/2} |\mathbf{R}_j + \mathbf{R}_{j+\frac{N}{2}}|^2}{2\sum_{j=1}^{N} |\mathbf{R}_j|^2} \tag{3.61}$$

This parameter is dimensionless and is always valued between zero and one. By including only atoms with centrosymmetry values in a specific range, it is possible to pick out different defects in a sample. In this thesis, the centrosymmetry parameter is used to detect dislocation lines, twin boundaries, grain boundaries, and amorphous regions in crystals. This analysis technique can easily be implemented using the Atomeye visualisation software package. The range of defects which can be identified using this metric makes it very useful for getting a comprehensive overview of defects in a sample. However, samples with a high density of defects and nanocrystalline samples can appear cluttered and individual defects can therefore be difficult to distinguish.

Calculating the centrosymmetry parameter for an atom is not a trivial process as there is no obvious way of determining which atoms are opposite near neighbours for a given atom. The normalised centrosymmetry parameter is implemented in the Atomeye using the following algorithm:

1. Pick the N closest atoms to the atom in question. These atoms are identified by the index j. These atoms are arranged in ascending order according to their distance to the central atom, $|\mathbf{R}_j|$.

2. Take the closest atom the central atom located at $|\mathbf{R}_1|$ relative to the central atom. Now search through the other $N-1$ neighbours for the atom, j', which minimizes:
$$\tilde{D}_{j'} \equiv |\mathbf{R}_1 + \mathbf{R}_j|^2 \tag{3.62}$$

3. Remove atoms 1 and j' and repeat step 2 until the values for $D_1, D_2, \ldots, D_{N/2}$ have been calculated. The normalised centrosymmetry parameter can then be calculated from:
$$c_{n,i} = \frac{\sum_{k=1}^{m_i/2} D_k}{2\sum_{j=1}^{m_i} |\mathbf{d}_j|^2} \tag{3.63}$$

By removing atoms with close to zero centrosymmetry from the system in question, we can observe many defects in the system at the same time. Figure 3.5 shows dislocations and twin boundaries in a system of bcc Fe revealed by analysis of the centrosymmetry parameter.

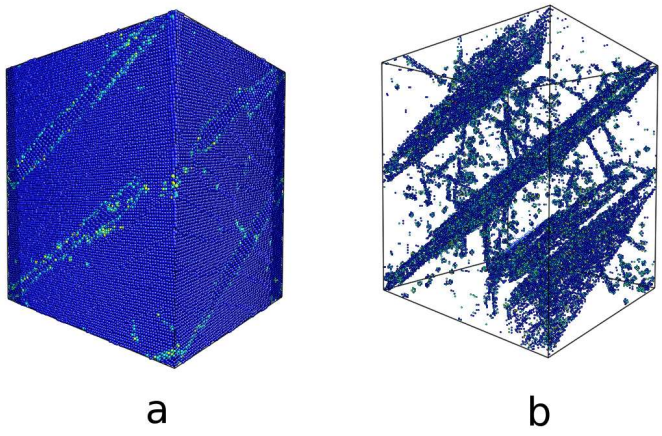

Figure 3.5 *(a) A block of bcc Fe containing twin boundaries and dislocations with atoms coloured by centrosymmetry parameter. (b) The same system where atoms with centrosymmetry parameter close to zero removed.*

3.8.4 Common Neighbour Analysis

Common neighbour analysis (CNA) is a method for identifying local crystal structure [81, 82]. The technique was not used in this thesis directly. However, CNA is performed as part of the Dislocation Extraction algorithm presented in the next section. We include details of the CNA here for completeness. In the CNA method, pairs of atoms in the crystal are characterised by three indices. Each pair of atoms in the system produces a set of indices and the distribution of these sets of indices is compared to a reference table to determine the structure. The distinguishing indices are:

1. The number of common neighbours shared by the pair of atoms.
2. The number of near neighbour relationships among the common neighbours.
3. The number of bonds in the longest continuous chain of bonds which can be formed from these common neighbours.

Table 3.2 *CNA signatures for hcp, fcc, and bcc structures.*

fcc	hcp	bcc
12 × (421)	6 × (421)	8 × (666)
	6 × (422)	6 × (444)

For each atom in a sample, indices are collected for all atom pairs consisting of the atom in question and another atom within a specific cutoff distance of the atom in question. For fcc and hcp structures, this cutoff distance is set to be half way between the distance to a first nearest neighbour and the distance to a second nearest neighbour. For bcc structures, the cutoff distance is half way between the distance to a second nearest neighbour and the distance to a third nearest neighbour. The distribution of indices is then compared to a reference table to determine the crystal structure. Table 3.2 shows the indices for various difference crystal structures in the CNA.

3.8.5 Dislocation Extraction Algorithm

The dislocation extraction algorithm is a tool for detecting dislocations and grain boundaries in molecular dynamics systems [83]. The technique was used in the work presented in this thesis as in addition to producing visualisations of dislocation lines and grain boundaries, the algorithm also determines the Burgers vector for each dislocation line. It should be noted that for large samples with a million or more atoms, it can take several minutes to process a single simulation output file. This can make this technique cumbersome to use if output files corresponding to many different points in time in a simulation have to be analysed. A code which implements this algorithm is available from Alexander Stukowski of Darmstadt University of Technology [83]. This code produces an output which can easily be visualised using the ParaView visualisation package. When DXA is performed on a system, an output is generated containing dislocation lines for each dislocation segment in the sample as well as their associated Burgers vectors.

Performing CNA allows defect atoms to be identified and separated from crystalline atoms. This is illustrated in figure 3.6. Atoms in the dislocation core are identified as defect atoms. However some atoms are identified as not being crystalline by CNA despite sitting on lattice sites. These are designated as interface atoms and are defined as any atoms not identified as crystalline by CNA which have at least one crystalline atom among their nearest neighbours.

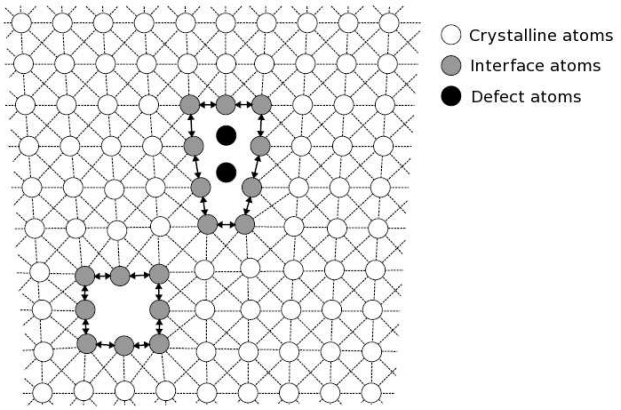

Figure 3.6 *Illustration showing classification of atoms in a crystal. The CNA categorises atoms as being crystalline or defect atoms. Atoms categorised as defect atoms which have at least one crystalline atom in their list of near neighbours are then designated as interface atoms. Image taken from paper by Stukowski and Albe [83]*

As the CNA is performed, lists of nearest neighbour atoms are collected and stored for each atom. Using this neighbour list data, one can map the atoms from a crystalline cluster in the input file to a corresponding location on an ideal reference lattice. This reference lattice is an ideal lattice i.e. one where atoms sit exactly on lattice sites and atoms are separated exactly by combinations of lattice basis vectors. In this way we remove any complications in the analysis caused by thermal motion of atoms and elastic strain fields.

To demonstrate how the near neighbour data can be used to map atoms from the input crystal to the reference lattice consider the case of a bcc crystal. During CNA, a list of 14 atoms consisting of the nearest neighbours and second nearest neighbours is generated for each atom. Figure 3.7 shows an atom in a bcc crystal along with its nearest and second nearest neighbours. By looking at the neighbour list for each of the atoms in the neighbour list of the central atom we can derive much information with respect to their positions in the reference crystal. We know which atoms in the neighbour list of the central atom are second nearest neighbours as these atoms only share four atoms with the central atom. Each second nearest neighbour is uniquely defined by the four nearest neighbours it shares with the central atom. We can now assign an arbitrary crystalline orientation to the reference lattice and calculate the lattice vectors connecting each atom to its neighbours. We can now move set one of the second nearest neighbours as a new central atom and repeat this analysis. Note that when we repeat the analysis, we do not set the orientation of the reference crystal as

arbitrary anymore. The orientation is inherited from the previous step.

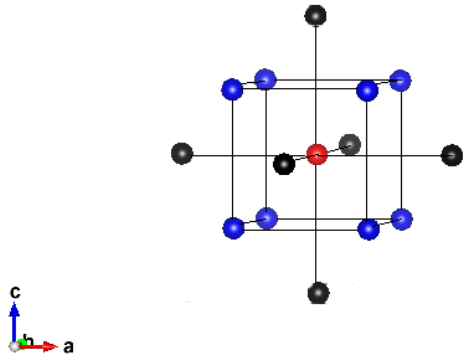

Figure 3.7 *Illustration of first and second nearest neighbours in a bcc crystal. The central atom is coloured red. First nearest neighbours are blue and second nearest neighbours are cloured black.*

As this analysis is performed the lattice vectors in the reference lattice connecting each atom to its neighbours are recorded in memory. We therefore have the following stored in memory at this point in the algorithm:

- a list of neighbours for each atom in the sample.
- the relative lattice vectors connecting each atom to each of its neighbours in the reference lattice.

From figure 3.6, one can see that a surface mesh made up of interface atoms will enclose any dislocation line in the sample. This surface mesh traces the dislocation line allowing the shape of the line to be printed in the output. A Burgers circuit can now be formed consisting of vectors connecting neighbouring atoms which are located on this mesh surface of interface atoms. In this manner the Burgers vector of a dislocation can be calculated. Full details of the dislocation line tracing and Burgers vector calculation can be found in appendix A.

A code for running the DXA algorithm and more information on the algorithm can be found at dxa.ovito.org. Outputs from this code can be imaged using the ParaView software package. An example of an output viewed in ParaView is shown in figure 3.8.

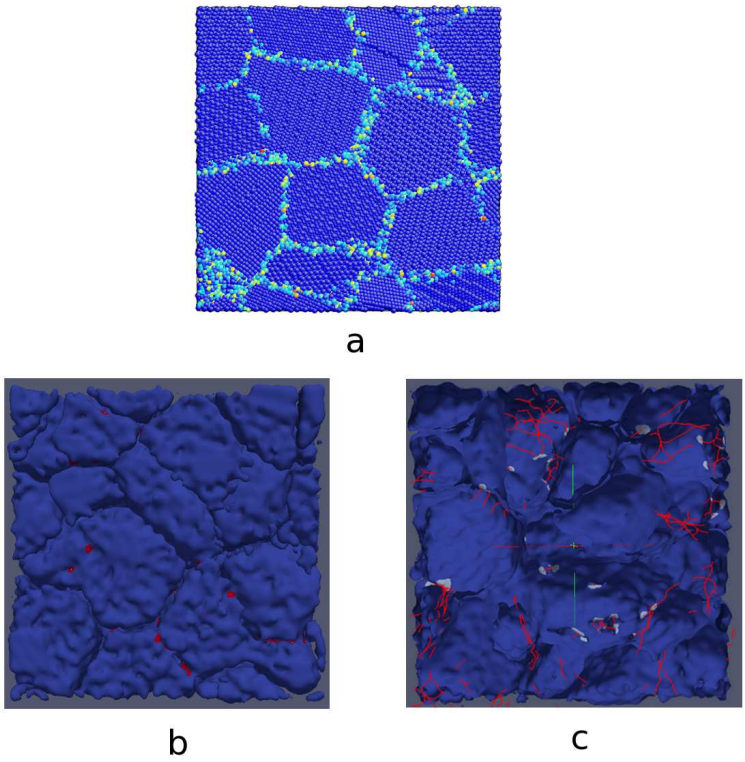

Figure 3.8 *Figure showing typical DXA output displayed in ParaView. (a) Image taken with BallViewer showing a nanocrystalline sample. Atoms are coloured by centrosymmery parameter. (b) The same sample images with DXA and ParaView. Each grain is represented by a blue surface. (c) A cross section of the graphic in (b). Red lines are dislocation lines.*

3.8.6 Atomic strain

The atomic strain tensor [84] is a metric which identifies regions where there is local plastic deformation. It was used in this thesis mainly to identify slip planes in simulations. The technique is easily implemented using either Atomeye or OVITO. This tensor is defined for each atom in the sample. The atomic strain for each atom is computed by comparing relative positions in a deformed system with those in an undeformed reference system. Here we represent the distance between two atoms in the deformed system by the row vector $\mathbf{d}_{ij}$. The corresponding vectors in the reference system are represented by the row vectors

$\mathbf{d}_{ij}^0$ A matrix, $\mathbf{J}_i$ is defined as the one for which the following is minimised:

$$\sum_{j \in N_i} |\mathbf{d}_{ij}^0 \mathbf{J}_i - \mathbf{d}_{ij}|^2 \tag{3.64}$$

where N_i is the coordination of atom i. $\mathbf{J}_i$ is the matrix which best maps the transformation:

$$\{\mathbf{d}_{ij}^0\} \rightarrow \{\mathbf{d}_{ij}\} \tag{3.65}$$

$\mathbf{J}_i$ is therefore the matrix which best maps neighbouring atoms in the deformed system to their positions in the undeformed system. In this sense in is similar to a strain tensor in a continuous system.

The quantity in equation 3.64 is minimised when $\mathbf{J}_i$ is given by [84]:

$$\mathbf{J}_i = \left(\sum_j^{N_i} \mathbf{d}_{ij}^{0T} \mathbf{d}_{ij}^0 \right)^{-1} \left(\sum_j^{N_i} \mathbf{d}_{ij}^{0T} \mathbf{d}_{ij} \right) \tag{3.66}$$

From this the atomic strain tensor, η_i, is defined for each atom as:

$$\eta_i = \frac{1}{2} \left(\mathbf{J}_i \mathbf{J}_i^T - \mathbf{I} \right) \tag{3.67}$$

A metric, η_i^{shear}, is used to measure local shear strain and this is defined as:

$$\eta_i^{shear} = \sqrt{\eta_{yz}^2 + \eta_{xz}^2 + \eta_{xy}^2 + \frac{(\eta_{yy} - \eta_{zz})^2 + (\eta_{xx} - \eta_{zz})^2 + (\eta_{xx} - \eta_{yy})^2}{6}} \tag{3.68}$$

This metric has been found to be a good measure of local plastic shear deformation. Figure 3.9 shows how slip planes and twinned regions of a crystal can be revealed using atomic strain as a metric.

3.8.7 Summary of Analysis Techniques

In this section we have presented various analysis techniques used to identify defects and deformation mechanisms in simulated crystalline samples. The centrosymmetry parameter and the dislocation extraction algorithm can be used to identify dislocations and grain boundaries. The Ackland-Jones method is used to determine crystal structures and disordered regions in simulated systems. Neighbour list analysis and atomic strain analysis can be used to identify local plastic deformation in samples. These techniques are summarised in table 3.3.

Table 3.3 *Table summarising various analysis techniques used in this thesis.*

Analysis Technique	**Description**
Centrosymmetry Parameter	Can detect any defect by measuring deviations from central symmetry for each atom in a sample. Can be implemented quickly and easily when using the Atomeye visualisaton package. Can be used to get a complete overview of defects present in a sample. However, nanocrystalline samples and samples with a high density of defects can appear cluttered making individual defects hard to distinguish.
Dislocation Extraction Algorithm (DXA)	Detects dislocations, twin boundaries, and grain boundaries in a sample. Burgers vectors are computed and returned in the output for each dislocation line. Computing time can make this technique cumbersome when analysing large samples.
Atomic Strain	Metric which measures local strain in a sample. Can be used to identify slip planes and is easily implemented in Atomeye and OVITO.
Neighbour list Comparison	Measures local plasticity by measuring changes in near neighbours for each atom between two points in time during a simulation. This metric can be intuitively understood and can be easily used to create visualisations with almost any visualisation software. Slip planes can be difficult to determine when using this metric on bcc samples.
Ackland-Jones Crystal Identification	Technique primarily used for determining the crystal structures present in a sample. Can be used to clearly illustrate crystalline and amorphous regions in a sample. This technique is easily implemented using BallViewer.

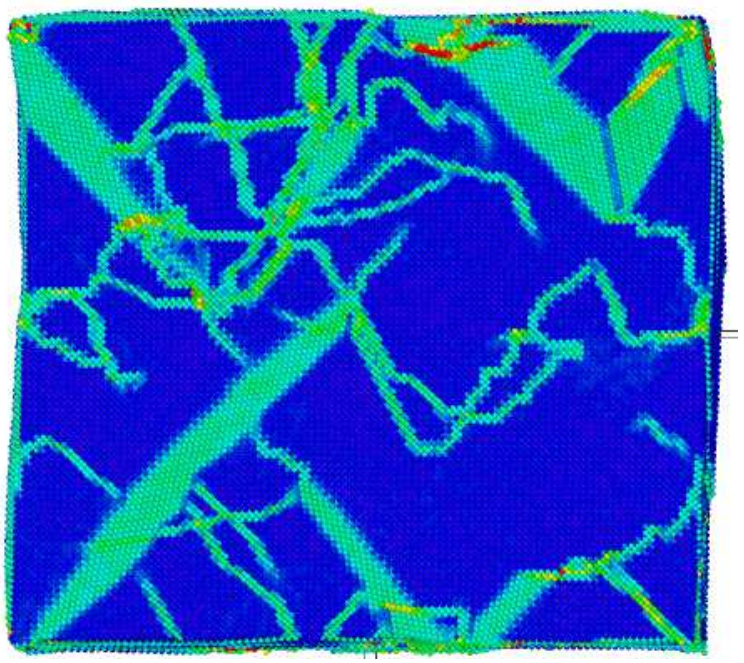

Figure 3.9 *Compressed block of Fe coloured according to atomic shear strain. Slip lines and twinned regions are clearly visible.*

Chapter 4

Spurious Behaviour in Simulations of Nanowire Plasticity

4.1 Introduction

Molecular dynamics simulations are commonly used in the study of plasticity in metals [27, 85–92]. Nanowires and nanopillars are often the basis of these studies due to their small size and an abundance of related experimental research. [4, 93–97] However, length scale limitations in Molecular Dynamics simulations prohibit one from practically simulating anything on length scales larger than tens of nanometers. This results in nanopillar simulations often being compared with experiments on much larger nanopillars or micropillars [96, 98]. In addition to this, strain rates applied in MD simulations are far higher than those studied experimentally. This can make it difficult to reproduce experimentally observed plasticity behaviour in simulations. However as experimental and computational techniques progress, molecular dynamics simulations are being performed on larger length scales and experimental nanopillar samples are becoming smaller. A recent study by Jang *et al* [95] involved molecular dynamics simulations and experiments at the same length scale.

MD simulations can also be sensitive to technical details such as choice of integration algorithms or use of periodic boundary conditions [99, 100]. In addition to this, one must take care when creating a complicated input system. It is inevitable that the construction of the input configuration can result in the

system being out of equilibrium, which will affect the outcome of the simulation, as it will show a transformation to the equilibrium state rather than a response to external forces. For example it is essential to remove vibrations in the sample caused by starting with a slightly different lattice parameter to the equilibrium value even if one starts with a stable configuration.

In the case of simulations of nanopillars, the input system has a large surface area and lack of surface stability in particular could therefore have a considerable effect on the simulation results. Many studies of MD simulations of nanopillars have now been published and in most cases the choice of crystallographic surface planes on the pillars seems to be arbitrary [93, 96, 97, 101–103]. Most commonly, pillars are created to have square or circular cross sections with less concern for how the choice of crystallographic surfaces might affect the results. However, given the high surface to volume ratio in simulated nanopillars, one might expect that higher energy surfaces on the faces of these nanopillars would have a disproportionate effect on the outcome of the simulation in comparison with experiments. These configurations are metastable and may retain their structure under static relaxation. Under the influence of applied stresses, however, surface reconstrucions may occur to bring the system to a more stable state. It is worth noting that the surface energy is higher than the the energy of the defects which cause plasticity and for that reason surface instabilities may have a disproportionate impact on the behaviour of the system.

Surfaces of as-synthesised crystals often contain facets or other surface reconstructions. These surfaces will often reconstruct or facet so that only close packed planes are exposed on the surface [104–109]. Ackland *et al* showed that, under compression, nanopillars with {100} surfaces deformed by recrystallization assisted by surface reconstruction in MD simulations[75].

Here we present some results from MD simulations of Fe nanopillars showing that the manner in which one applies strain in the simulations and the surface stability of the faces of the pillars can significantly affect the simulation results. We demonstrate that implementing strain by rescaling the coordinates periodically leads to conservation of net momentum in the system and consequently constrains the plasticity behaviour. We also find that surface stability has a significant effect on the plasticity behaviour. Pillars with {100} surfaces deformed by turning amorphous in the deformed region. Pillars with close packed {110} surfaces deformed by slip and twinning. In addition to this we find that performing the simulation at temperatures high enough to cause wetting on the surfaces of the

pillars results in the pillars deforming by amorphization.

4.2 Results

4.2.1 Momentum conservation effects

In this section we show that enforcing momentum conservation on a nanopillar has dramatic and spurious effects on the results.

We constructed a pillar with a square cross-section as seen in figure 4.1. The pillar had approximate dimensions of 4.3 nm × 4.3 nm × 34.3 nm and contained 50520 atoms. Typical nanopillars fabricated for experiments have diameters of 100nm or more [40, 43]. However, computing times for nanopillars of these sizes are prohibitively large. The side faces of the pillar were {100} type faces and the pillar were compressed in the [001] direction. Periodic boundary conditions were applied along the z axis to simulate a long continuous pillar.

Prior to loading, the pillar was heated to 300K by running a simulation for 50 picoseconds with a Nosé-Hoover thermostat[72, 73]. This heating was carried out to bring the pillar to a state in which the atomic displacements relative to their equilibrium positions reflected those of a pillar at 300K. The rest of the simulation was also carried out at 300K. Uniaxial strain was applied by rescaling the atomic coordinates in the direction of loading by 0.05% at 200 femtosecond intervals. The resulting strain rate is $2.5\times10^{9}\ s^{-1}$. Such large strain rates are necessary in molecular dynamics simulations due to the small time scales involved. Typical strain rates in nanopillar compression experiments are between $10^{-6}\ s^{-1}$ and $10^{-3}\ s^{-1}$ [40, 44]. This is a common means by which strain is applied in MD simulations. Simulations were carried out using the MOLDY molecular dynamics code[75]. The potential function used was that developed by Hepburn and Ackland [65].

Figure 4.2(a) shows this pillar after strain of 26%. The pillar has buckled due to the applied strain. Figure 4.2(b) shows a plot of the normal component of the stress on top surface of the MD cell vs strain. This is simply the component σ_{zz} of the virial stress tensor defined in equation 3.18. The top and bottom surfaces of the MD cell measure 8.57 nm × 8.57 nm. We measure this stress rather than the stress at the top of the pillar as the cross sectional area of the pillar is variable and

difficult to define. This graph shows a rise in stress as strain is applied followed by a sudden drop when the pillar begins to buckle. No plastic deformation takes place and the stress in the pillar increases linearly prior to buckling. The stress shows small periodic increases and decreases in stress giving the graph in figure 4.2(b) a jagged texture. This is due to the strain increments applied during the simulation.

The shape of the pillar in figure 4.2(a) is, unusually, an "S" shape. This is quite an unusual morphology. In experiments on nanowires and on macroscale structures such as metal beams, buckled structures form a "C" shape [110–112]. This discrepancy between experiments and simulations is due to the way in which strain was applied. At each strain increment the z component of the atoms were all rescaled uniformly. Each atom movement resulted in an additional force on the moved atom due to all other atoms in the pillar and an equal but opposite additional force on all other atoms due to the moved atom. For this reason, strain increments do not change the net momentum of the pillar. The formation of a "C" shape buckle requires motion of the centre of mass of the system. This is not possible if the overall momentum of the system is constrained to be zero. Instead, as the pillar buckles, atoms in the upper half of the pillar move in the opposite direction to those in the lower half to compensate for any momentum change. In this way the pillar bends into an "S" shape.

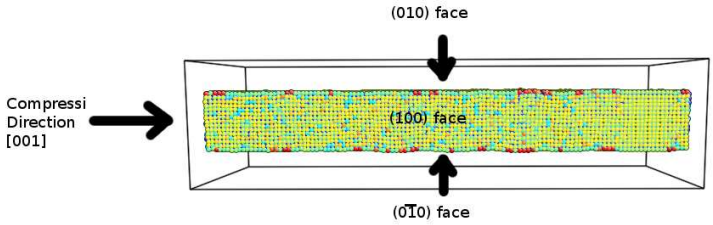

Figure 4.1 *Image of pillar prior to being strained. The pillar has been heated to 300K by coupling to a Nose-Hoover thermostat for 50 ps. Atoms are coloured according to centrosymmetry parameter. This pillar had* {100} *type side faces and the compression direction was* [001]

One can allow net momentum to change in the pillar by constraining some atoms in the pillar. These constrained atoms act as a source of external forces to the system.

We repeated the simulation detailed above after constraining atoms within a distance of 1.7 nm from either end of the pillar. Since the constrained atoms

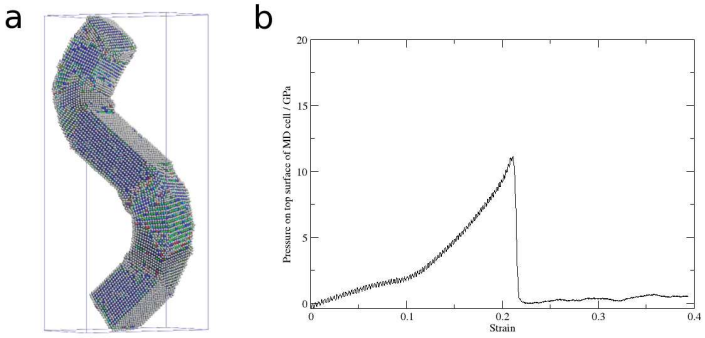

Figure 4.2 *(a)Image of buckled pillar following a strain of 26%. The method of applying strain causes total momentum in the pillar to be conserved. This results in the pillar buckling to form an "S" shape. Atoms are coloured according to the Ackland-Jones identification technique. Blue atoms represent bcc atoms while all other colours represent atoms which have been misidentified due to the presence of defects or surfaces. (b) Plot of stress normal to the upper surface of the MD cell vs. strain. The large drop in stress is the point at which the pillar begins to buckle.*

do not move, we are effectively applying external forces to each of them in order to keep them in place. This allowed the remaining atoms in the system to acquire non-zero total momentum during the simulation. This pillar now had 4856 constrained atoms and 45664 unconstrained atoms. Periodic boundary conditions were no longer imposed in the simulation. All other simulation details were the same as before.

Figure 4.3(a) shows an image of this pillar following a strain of 26%. The pillar deforms through amorphisation and slip and buckles to form a more typical "C" shape. The stress and strain values at the point at which which buckling occurs are lower than that in the previous simulation as there are fewer constraints on how the buckling occurs. The "C" buckle requires less stress to occur and stress therefore rises more in the previous simulation where the "C" buckle is prohibited by the simulation conditions.

It is worth noting that many published studies have implemented strain on nanowires in such a way that momentum is conserved in the system [3, 93, 94, 97, 102, 113–118].

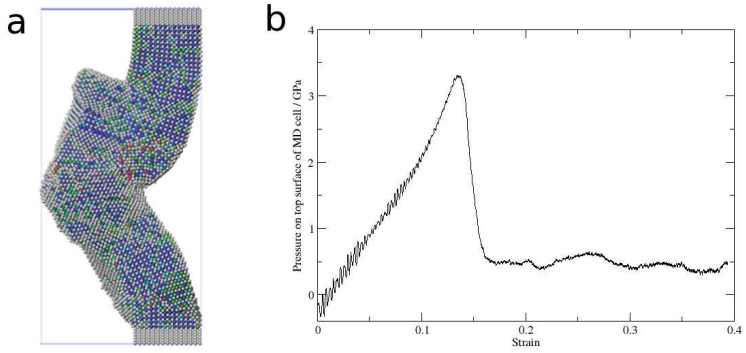

Figure 4.3 *(a)Image of pillar with* {100} *faces containing constrained atoms at the ends following a strain of 26%. Constrained atoms are a source of external forces in the system and total momentum in the pillar is therefore no longer conserved. Pillar now buckles to form a more common "C" shape. Atoms are coloured according to the Ackland-Jones identification technique. Blue atoms represent bcc atoms while all other colours represent atoms which have been misidentified due to the presence of defects or surfaces. (b) Plot of stress normal to the upper surface of the MD cell vs. strain. The peak stress in the pillar is now lower as the shape of the buckle is no longer constrained.*

4.2.2 Creating nanopillars with unstable surfaces

In this section we show that starting the simulation with metastable surfaces leads to a spurious deformation mechanism.

Further investigation of the "C" buckle simulation detailed in the previous reveals that the region near the buckle point turns amorphous as the pillar buckles. Figure 4.4 shows images of the pillar following a strain of 18%. At this point the pillar has begun to buckle. Images of the inside of the pillar in the amorphous region and centrosymmetry parameter analysis show that the region is amorphous. There is some heat localization in the amorphous region but it is difficult to say whether or not the amorphous region is above the melting temperature as temperature is not easily defined for such small numbers of atoms.

In order to test whether or not constructing a pillar with {100} surfaces affects how the pillar deforms, we performed a similar simualation with a pillar of similar dimensions. This time the pillar was constructed with stable {110} faces. This pillar had approximate dimensions of 8.0 nm $\times$ 8.0 nm $\times$ 34.3 nm. Atoms within a distance of 1.7 nm from each end of the pillar were constrained. The pillar

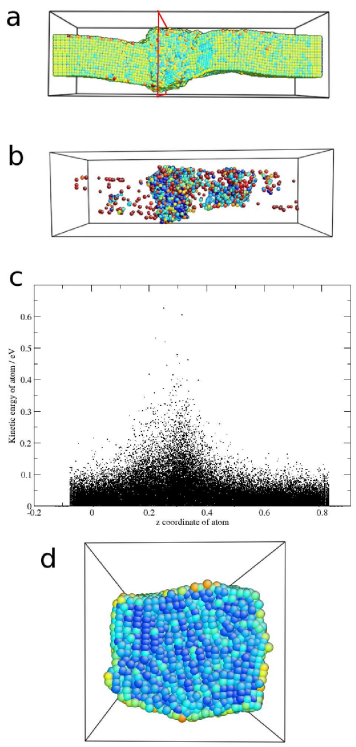

Figure 4.4 *(a) Pillar with* {100} *faces following strain of 18%. The bulged region near the centre has deformed plastically by turning amorphous. (b) The same pillar showing only atoms high centrosymmetry parameter. The loss of central symmetry in the deformed region indicates that this region has turned amorphous. (c) Plot of kinetic energy vs positional z component for each atom in the pillar. There is some heat localization in the amorphous region of the pillar. (d) Image showing the inside of the inside of the amorphous region. The location of this cross section is indicated by the red frame in (a). Atoms coloured according to centrosymmetry parameter.*

consequently contained 3307 constrained atoms and 49613 unconstrained atoms. These constrained atoms form plates at either end of the pillar. These plates effectively allow external forces to be applied to the system and confine the unconstrained atoms in between the plates. When uniaxial strain is applied to the pillar, the plates act much like an indenter in a micropillar compression experiment. Plates of constrained atoms such as this shall be referred to as indenter plates in the remainder of this thesis. Periodic boundary conditions were not applied in this simulation as the indenter plates necessarily break the periodicity.

Compression of the pillar was carried out as in the previous simulations. Prior to loading the pillar was heated to 300K by running a simulation for 50 picoseconds with a Nosé-Hoover thermostat[72, 73]. Uniaxial strain was applied by moving the indenter plates and rescaling the atomic coordinates for all atoms in the direction of loading by 0.05% at 200 femtosecond intervals. The resulting strain rate is $2.5\times10^{9}\ s^{-1}$. Simply moving the indenter plates incrementally and allowing the unconstrained atoms in the system to react to the new indenter positions might seem like the most appropriate way of representing a nanopillar compression experiment in a simulation. However, as the strain is applied incrementally, there will be a discontinuity in the stress and strain immediately below the indenter plates following each strain increment when applying strain in this way. This results in the propagation of shock waves in the system which are simulation artefacts. Similar techniques are in fact used to intentionally create shock waves in simulations [119, 120]. Applying strain by incrementally rescaling the coordinates of all atoms in the system (rather than just the indenter plate atoms) allows one to avoid creating shock waves in the system.

Figure 4.5(a) shows the pillar following a strain of 18%. Unlike the pillar with {100} faces, this pillar has not yet buckled at 18% strain. All plastic deformation has taken place at the ends of the pillars via dislocation glide with dislocations nucleated from the edges of the pillar. The pillar eventually buckles as seen in figure 4.5(c). No region of the pillar turns amorphous at any point during the compression.

The change in plasticity behaviour in this pillar from the pillar with {100} surfaces may be due to the fact that {100} surfaces have a higher surfaces energy than {110} surfaces. Figure 4.6 shows the energy per atom vs. strain for the nanopillar with {100} faces and that of the nanopillar with {110} faces calculated by static relaxation. This graph samples only small elastic strains so a buckling event is not visible on the graph. Overall the energy per atom of the energy per atom in the pillar with {100} faces is about 0.01 eV greater than that of the pillar with {110} faces. The energy difference between a single atom on a {100} surface was found to be 0.11 eV greater than that on a {110} surface.

Many previous studies of nanopillar and nanowire plasticity have used pillars with high energy surfaces such as {100} [3, 93, 97, 102, 113–118, 121].

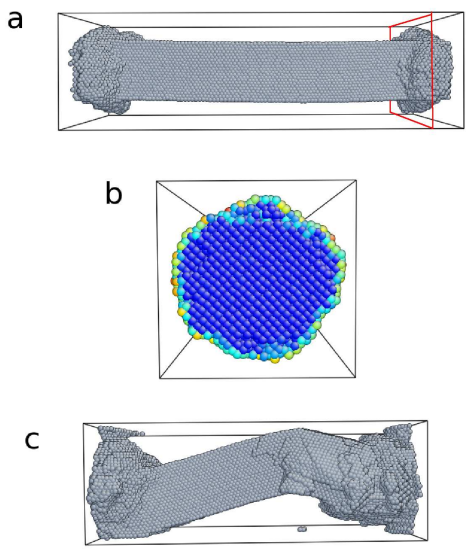

Figure 4.5 *(a)Pillar with* {110} *faces following a compressive strain of 18%. No amorphous region is present. Deformed regions at the ends of the pillars have deformed by dislocation glide. (b) Image showing the inside of one of the deformed regions in (a). Atoms are coloured according to the Ackland-Jones identification technique. Blue atoms represent bcc atoms while all other colours represent atoms which have been misidentified due to the presence of defects or surfaces. The location of this cross section is indicated by the red frame in (a). (c) Image of pillar with* {110} *faces following a strain of 33%. Again, no amorphous region is present.*

4.2.3 Pillar Compression at 1200K

Surface premelting occurs in MD simulations and can affect how deformation occurs, in particular when surface area is large in comparison to volume. Here we present results from a simulation of a pillar compression carried out at 1200K. The melting temperature for the potential used was 1750K [65].

This system consisted of a pillar with a square cross-section in between two "indenter plates" as seen in figure 4.7(a). The pillars had approximate dimensions of 5.8 nm $\times$ 5.8 nm $\times$ 15.4 nm and contained 45513 atoms. The sample is confined by indenter plates, each containing 9901 atoms (12.1 nm $\times$ 12.1 nm $\times$ 0.9 nm), Movement of indenter plate atoms is constrained in order to apply external forces. This allowed total momentum of the system to change during the simulation. The side faces of the pillar were {110} type faces, which are the most stable surfaces for bcc materials.

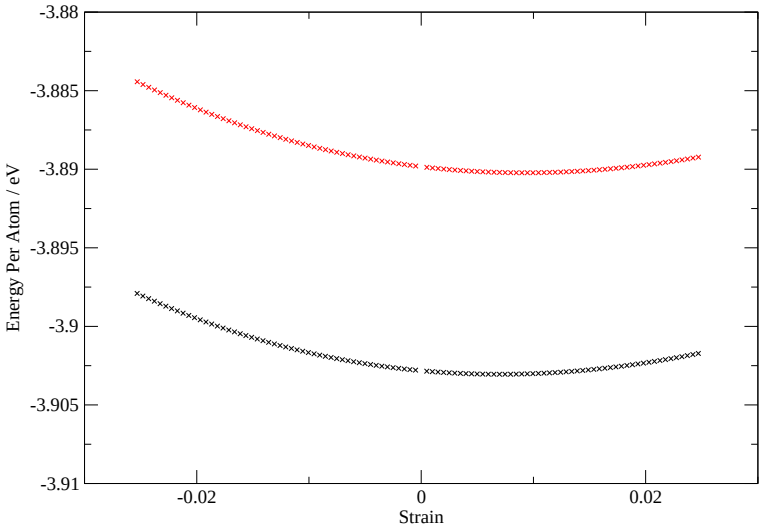

Figure 4.6 *Plot of energy per atom vs strain for pillar with* {110} *surfaces (black) and* {100} *surfaces (red). Here negative strain implies tension and positive strain implies compression relative to the bulk lattice parameter. The minimum energy of each wire does not occur exactly at zero strain due to surface tension in the nanopillars. Note that this graph shows data for small elastic strains. There is therefore no sudden drops in energy due to bursts of plasticity such as buckling events.*

Figure 4.7 shows how heating of this pillar causes premelting on the surfaces. The pillar was heated by coupling to a Nosé-Hoover thermostat at 1200K. Following 50 ps of heating, the pillars show some surface premelting. The simulations detailed previously in this chapter, in contrast, showed no surface premelting following 50 ps of heating at 300K. After 1 ns of heating the cross section of the pillar has rounded due to surface tension. The centre of the pillar remains crystalline.

We performed compression simulations on this pillar. Prior to loading, all pillars were heated to 1200K by running a simulation for 50 picoseconds with a Nosé-Hoover thermostat[72, 73]. The Nosé-Hoover constant was set to 1000 which was sufficient to keep the temperature of the pillar at 1200K throughout the simulation. Uniaxial strain was applied by moving the indenter plates and rescaling the atomic coordinates in the direction of loading by 0.05% at 2 picosecond intervals. The resulting strain rate is $2.5\times10^{8}\ s^{-1}$.

Compression causes the entire pillar to turn amorphous. Surface tension subsequently causes the pillar to narrow in the centre until the pillar has eventually split in two. This can be seen in figure 4.8. When this compression simulation is carried out at 300K, the pillar deforms by dislocation glide. Further

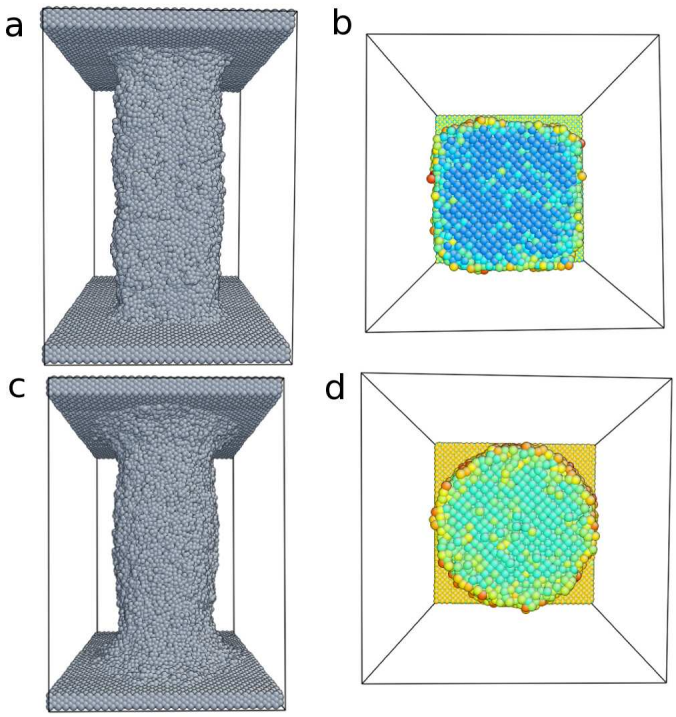

Figure 4.7 *(a)Pillar with* {110} *faces following heating to 1200K by coupling to a Nosé-Hoover thermostat for 50 ps. The pillar shows some surface premelting. (b) Profile of the inside of the pillar in (a). (c) Pillar in (a) following heating for 1 ns by coupling to Nose-Hoover thermostat at 1200K. Surface premelting and surface tension cause the pillar to form a circular profile. (d) Image showing the inside of the pillar in (c). The inside of the pillar is still crystalline. Atoms in (b) and (d) are coloured according to centrosymmetry parameter.*

details of this will be given in the following chapter.

4.3 Discussion

Many molecular dynamics studies have now been published on the subject of plasticity of nanowires and nanopillars [122]. The reported plasticity behaviour from these structures is diverse. Some studies have reported dislocation glide as the dominant deformation mechanism while others have reported lattice and surface reorientation, twinning, and a transition to an amorphous phase at high strain rates [4, 94, 122, 123]. However, practices such as constructing pillars/wires with high energy surfaces and not including sources of external forces in the system are commonly reported. Here we will review some of these studies.

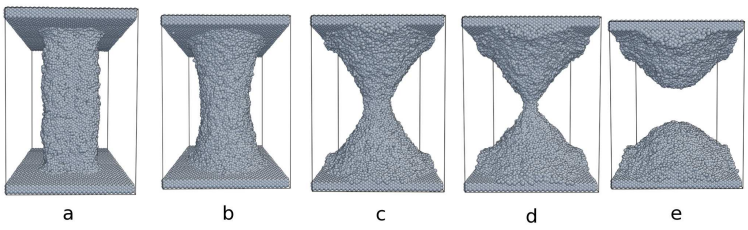

Figure 4.8 *Images of pillar with* {110} *faces following compression of (a) 0%, (b) 5%, (c) 10%, (d) 14%, (e) 18%. Compression was carried out at 1200K. Compression induces a strong surface reconstrucion process which causes the pillar to turn amorphous and adopt a hemispherical shape to minimise surface area.*

The results of many simulations in the existing literature report deformation by glide of Shockley partials in fcc nanopillars. Simulations by Cao and Ma [123] for example, found that nanopillars of copper deform by glide of Shockley partials. They carried out simulations of strain on two types of $\langle 111 \rangle$ oriented pillars, one with a square cross section containing two $\{110\}$ side surfaces and two $\{112\}$ side surfaces, and another with a circular cross section. They found a significant difference in the surface stresses for these two pillars, despite them having the same length and width. The yield stress was also significantly different for these two pillars suggesting that the stress at which partial dislocations are created at the surfaces depends sensitively on the surface structure and orientation. Experimental nanowire samples in fcc materials typically contain a large number of $\{111\}$ facets when the surface orientations are not $\{111\}$. The nanowires often have a jagged surface texture which arises from surface reconstructions which create low energy surfaces (such as $\{111\}$) on the face of the wires. Facets such as this can be seen on the gold nanowire in figure 2.21. For relevance to experiments, molecular dynamcs simulations should therefore be carried out on pillars with low energy $\{111\}$ surfaces. Many more published studies reporting glide in fcc nanopillars were carried out using pillars with unstable surfaces.

Rabkin *et al* reported on simulations of plasticity in fcc gold nanopillars in two papers [113, 114]. They reported plasticity dominated by glide of Shockley partials. All simulations in these studies were carried out on pillars with circular cross sections. In all of these simulations, no constrained atoms or other sources of external forces were present in the pillars which, as we have shown above, can effect the plasticity behaviour and constrains the possible final geometries of the nanopillars.

Diao *et al* also published two papers reporting on simulations of plasticity in fcc gold nanowires [115, 116]. Similarly, they reported plasticity mediated by glide of Shockley partials. Again, nanowires were constructed with unstable surfaces. The simulations in these papers were carried out on $\langle 111 \rangle$ oriented nanowires with $\{110\}$ and $\{112\}$ side surfaces, and on $\langle 100 \rangle$ oriented nanowires with $\{100\}$ side surfaces. These simulations were also carried out on systems without any constrained atoms to provide a source of external forces in the system.

Afanasyev and Sanzoz reported on the effect of twins on dislocation mediated deformation in fcc gold nanowires [121]. They found that their nanopillars were strengthened by the presence of twin boundaries in the pillars. These simulations were carried out on nanopillars with circular cross sections.

Hou and Melikhova also reported deformation mediated by glide of Shockley partials in fcc aluminium nanowires [97]. The constructed their pillars with circular cross sections and included no source of external forces in the system.

Kotrechko and Ovsjannikov published a study on the temperature effect on yield stress in nanowires of bcc Mo, Fe, and W [117]. They found that the yield stress varied as a parabolic function of temperature. This is different from the bulk materials where yield stresses vary exponentially with temperature. However, they constructed nanowires in various orientations with circular cross sections and carry out the simulations at temperatures up to 1000K. As we have shown, at this temperature, plasticity in nanowires of Fe will be strongly affected by surface tension. Over time scales longer than those in MD simulations, it is questionable whether these nanowires would be stable, even if constructed with low energy surfaces.

Deformation by amorphization has frequently been reported to occur in fcc nanostructures when subject to high strain rates. In a paper by Ikeda *et al* [94], amorphization was found to occur in nickel nanowires subject to strain rates above a critical value. These simulations were carried out without any source of external forces in the nanowires. Similar effects were found by Koh *et al* [3, 93] in platinum and aluminium nanowires. Images from the Koh *et al* paper showing amorphization in the pillars can be seen in figure 4.9. These nanowires also contained no source of external forces (hence conserving total momentum in the system) and were constructed with high energy surfaces. Some were constructed with a circular cross section while others were constructed so as to contain $\{100\}$ side surfaces. This amorphization effect was also reported by Sankaranarayanan

et al [102] and by Wen *et al* [118]. They also constructed their nanowires with {100} side surfaces and neglected to include any source of external forces in their systems.

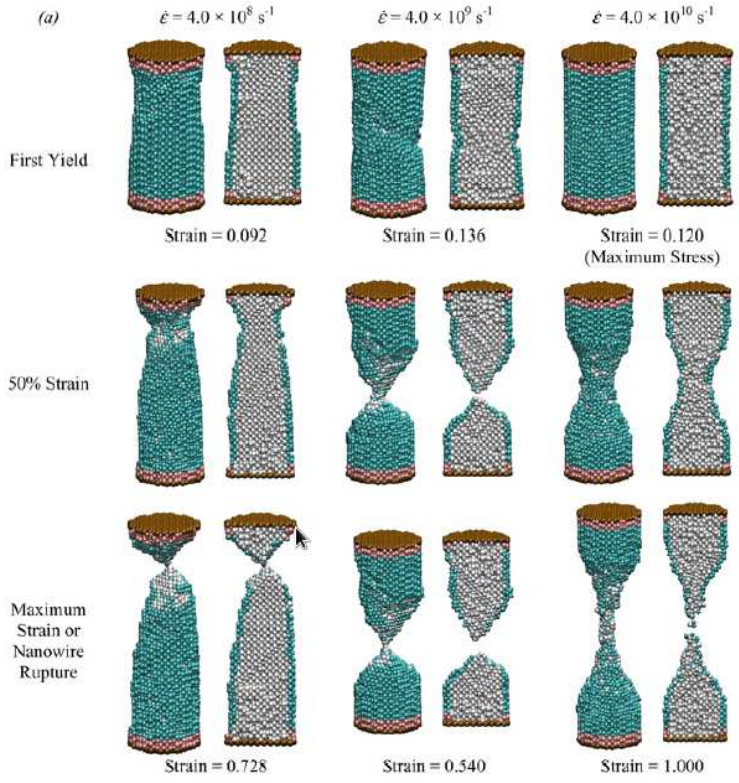

Figure 4.9 *Images showing pillars subject to tensile strain at various strain rates from paper by Koh and Lee [3]. One the right, a pillar can be seen deforming by amorphization at high strain rate. This amorphisation effect may be influenced by the unstable surfaces on the pillars (see table 4.1).*

In recent years, pseudoelasticity has also been reported numerous times in both fcc and bcc nanowires. These pseudoelasticity phenomena are usually characterised by a reversible lattice reorientation and/or surface reorientation. These processes usually involve a reorientation which occurs when the strain is applied, resulting in a pillar with high energy surfaces in a stressed state. The reorientation in the wires is reversed when a strain is then applied in the opposite direction. For fcc materials, Park *et al* [124] demonstrated that nanowires oriented along $\langle 110 \rangle$ with $\{111\}$ type side surfaces underwent a reorientation when subject to tensile strains. The nanowires were found to transform to a $\langle 100 \rangle$ orientation with $\{100\}$ type side surfaces. When a strain was applied in the opposite direction immediately following the application of the tensile strain, the nanowires recovered their initial orientation. It should be noted that the

circumstances in which this pseudoelasticity occurs is probably limited by the stability of the {100} side surfaces. Similar behaviour was found in nanowires of bcc Fe by Li *et al* [4, 125]. They demonstrated reversible plasticity in $< 110 >$ oriented nanowires with {110} side surfaces. Two of the four side surfaces of these nanowires changed orientation from {110} to {100} via a twin mechanism upon application of a tensile strain. The nanowires recovered their original shape when a strain in the reverse direction was applied immediately following this tensile strain. Li *et al* claim that these nanopillars could be used for energy storage by applying a fixed tensile strain [4]. We have tested the stability of the reoriented nanowires after the initial tensile strain is applied. We find that the {100} surfaces undergo reconstruction if the strain is held fixed for more than a few nanoseconds. An image of this surface reconstruction can be seen in figure 4.10.

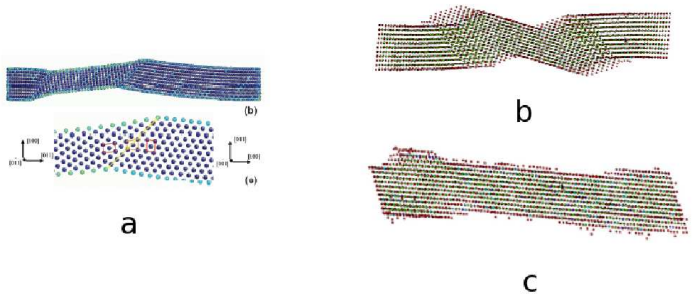

Figure 4.10 *(a) Nanowire from paper by Li et al [4] following tensile strain. The authors claimed that this nanowire to be superelastic. The narrow section on the left of the nanowire has undergone a surface reconstruction and consequently has two* {100} *surfaces. (b) We repeated this simulation and found that if the strain was held at a fixed value once the surface reconstruction had taken place, the surface reconsructed again to relieve stress. The image here shows the surface reconstruction after the strain was held fixed for 3 ns. (c) We also found that the nanowire did not recover its initial shape if allowed to relax at constant pressure rather than being subject to an applied compressive strain. The image here shows the final shape of the nanowire once the relaxation was complete. The nanowire contracted in length but relaxed to a shape different from the initial configuration of the nanowire. Atoms in (b) and (c) are coloured according to the Ackland-Jones identification technique. Green atoms represent bcc atoms while all other colours represent atoms which have been misidentified due to the presence of defects or surfaces.*

There is some evidence from the literature on nanostructures that unstable high

energy surfaces can strongly affect the outcome of deformation simulation. Park *et al* [5] reported the creation of {111} facets in gold nanowires as tensile strains were applied. An image showing creation of these facets can be seen in figure 4.11. Ackland [75] showed that surface reconstruction can be a deformation mechanism in fcc nanowires. He found a nanopillar of Cu oriented along ⟨100⟩ with {100} side faces reconstructed to form a pillar with {111} side faces. Park *et al* [124] showed that fcc nanowires with {100} side surfaces can spontaneously reorient if the size of the nanowires is small enough. The surface reconstructions from these studies can be seen in figure 4.12

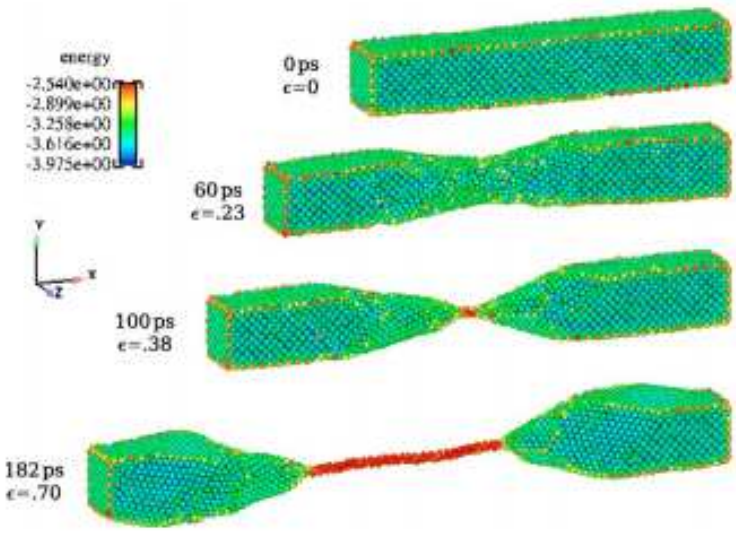

Figure 4.11 *Image taken from paper by Park et al [5]. {111} facets were formed when these fcc nanowires were subject to tensile strains.*

Table 4.1 *Table summarising previous studies which employed simulation practices which can have unphysical consequences.*

Author(s)	Title of Paper	Bad Practices
Cao and Ma [123]	Sample shape and temperature strongly influence the yield strength of metallic nanopillars.	Pillars had high energy surfaces.
Rabkin *et al* [113]	Atomistic simulation of the deformation of gold nanopillars.	Pillars had high energy surfaces and contained no constrained atoms.

Continued on next page

Table 4.1 – continued from previous page

Author(s)	Title of Study	Bad Practices
Rabkin *et al* [114]	Onset of plasticity in gold nanopillar compression.	Pillars had high energy surfaces and contained no constrained atoms.
Diao *et al* [115]	Yield strength asymmetry in metal nanowires.	Pillars had high energy surfaces and contained no constrained atoms.
Diao *et al* [116]	Atomistic simulations of the yielding of gold nanowires.	Pillars had high energy surfaces and contained no constrained atoms.
Afanasyev and Sanzoz [121]	Strengthening in gold nanopillars with nanoscale twins.	Pillars had high energy surfaces.
Hou and Melikhova [97]	Internal stress and mechanical deformation of al and Al/Ni multilayered nanowires.	Pillars had high energy surfaces and contained no constrained atoms.
Kotrechko and Ovsjannikov [117]	Temperature dependence of the yield stress of metallic nano-sized crystals.	Pillars contained no constrained atoms and simulations carried out at high temperatures.
Ikeda *et al* [94]	Strain rate induced amorphization in metallic nanowires.	Pillars contained no constrained atoms.
Koh *et al* [3]	Molecular dynamics simulation of size and strain rate dependent mechanical response of fcc metallic nanowires.	Pillars had high energy surfaces and contained no constrained atoms.
Koh *et al* [93]	Molecular dynamics simulation of a solid platinum nanowire under uniaxial tensile strain: Temperature and strain-rate effects.	Pillars had high energy surfaces and contained no constrained atoms.

Continued on next page

Table 4.1 – continued from previous page

Author(s)	Title of Study	Bad Practices
Sankaranarayanan *et al* [102]	Molecular dynamics simulation of temperature and strain rate effects on the elastic properties of bimetallic Pd-Pt nanowires.	Pillars had high energy surfaces and contained no constrained atoms.
Wen *et al* [118]	Surface stress driven reorientation of gold nanowires.	Pillars had high energy surfaces and contained no constrained atoms.
Park *et al* [5]	Modeling inelasticity and failure in gold nanowires.	Pillars had high energy surfaces.
Li *et al* [125]	High-efficiency mechanical energy storage and retrieval using interfaces in nanowires.	Pillars had high energy surfaces.
Li *et al* [4]	Superelasticity in bcc nanowires by a reversible twinning mechanism.	Pillars had high energy surfaces.

4.4 Conclusion

We have demonstrated that deformation processes observed in MD simulations can be dominated by initial conditions and configuration. In particular, deformation processes can depend sensitively on the method by which strain is applied in the simulation. Incrementally moving subsets of the atoms in the MD cell is known to produce shock waves in the system [119]. The more common method of rescaling all fractional atomic positions in the MD cell periodically, results in net conservation of momentum in the system in the absence of constrained atoms. We have shown that this can lead to constraints on deformation processes if no constrained atoms are introduced in the system. In particular, the lack of constrained atoms in the nanopillars presented here resulted

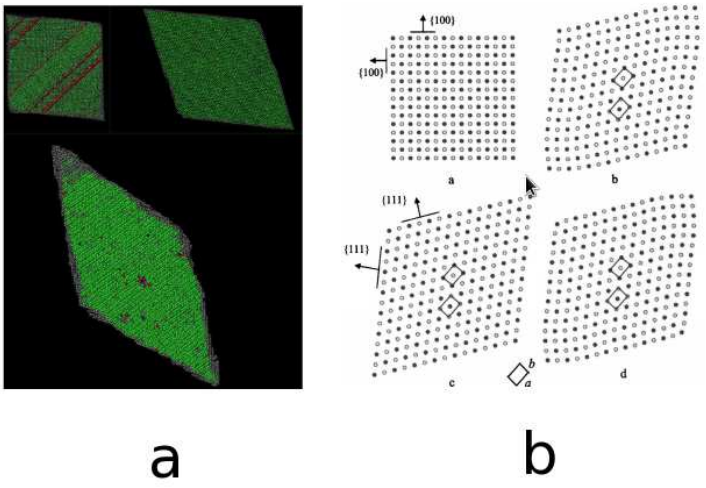

Figure 4.12 *(a) Image taken from paper by Ackland et al [75] showing surface reconstruction as a* $< 100 >$ *oriented nanopillar with* $\{100\}$ *side faces. (b) Surface reconstruction reported by Park et al [124]. This* $< 100 >$ *oriented nanopillar with* $\{100\}$ *side faces was found to spontaneously reconstruct so that the pillar had* $\{111\}$.

in "S" shaped buckling rather than "C" shaped.

MD is typically used to simulate systems on length scales of the order of tens of nanometers or smaller. At these length scales, introducing surfaces in the system leads to large surface to volume ratios. We have demonstrated that surface stability can have significant effects on plasticity. One must be cautious of surface stability in MD simulations. Construction of unstable or metastable surfaces in the system can affect the simulated plasticity behaviour.

There are many published studies on MD simulations of nanopillars. However, the majority of these studies were on pillars constructed with high energy surfaces. It is therefore particularly noteworthy that constructing pillars with high energy surfaces can change the plasticity behaviour.

Chapter 5

Compression-Tension Asymmetry in bcc-Fe Nanowires

5.1 Introduction

The experimental development of micro-mechanical testing on single crystals [40] has enabled the study of plastic deformation to be taken to the microscopic level. Under uniaxial compression of single crystals, yield can be observed on a single slip plane. Samples can now be tested in both tension and compression, and recent work has shifted to bcc materials where a tension-compression asymmetry is observed [54]. Schmid's law (which was introduced in section 2.2.1) states that the critical resolved shear stress required to initiate dislocation glide is constant for a given material. FCC materials generally obey Schmid's law, which has no tension-compression asymmetry and it is interesting to examine how the asymmetry appears in bcc materials which have intrinsic asymmetry arising from the core stucture of dislocations.

As discussed in section 2.7.4, recent experiments by Kim and Greer revealed a tension-compression asymmetry in the plasticity of bcc nanopillars [52–54, 126]. In compression, plastic deformation was confined mostly to narrow slip bands and the stress vs strain behaviour was characterised by many strain bursts. This stress vs. strain signature would suggest deformation by dislocation glide. In tension, deformation resulted in necking and the stress vs strain behaviour revealed larger periods of almost constant flow stress. Kim and Greer suggested

that the twinning-antitwinning asymmetry could be a cause for the compression-tension asymmetry[54]. However, it was unclear from experiments what processes were occuring at the atomic level. Molecular dynamics simulations can be used to study such atomic level processes.

Compression-tension asymmetry manifest as the dependence of the critical resolved shear stress (CRSS) on the sense of shear (i.e. tension or compression) is a feature of bcc single crystals [127–129]. Initial explanations for this phenomenon focused on what is called the twinning-antitwinning slip asymmetry. $\{112\}\langle 111\rangle$ type twins are created in bcc crystals when $\frac{1}{2}\langle 111\rangle$ dislocations split into $\frac{1}{6}\langle 111\rangle$ fractional dislocations which spread out on subsequent planes to create a twin plane [11]. The movement of these fractional dislocations must be in one specific direction on a given $\langle 111\rangle$ axis in order to create a twin boundary. Glide in the opposite direction (the anti-twinning direction) creates an unstable stacking fault which is not a twin plane. The CRSS for glide of $\frac{1}{6}\langle 111\rangle$ fractional dislocations in the twinning direction is therefore lower. Work by Vitek *et al* gives further weight to this argument. In this study, the γ-surface for a $\{112\}$ plane was calculated using a Finnis-Sinclair potential, and an asymmetry in the surface in the $\langle 111\rangle$ direction was found [27]. For a crystal in a fixed orientation, relative motion of subsequent slip planes in compression will always be in the opposite direction to relative motion of subsequent slip planes in tension. The directional asymmetry in the glide of dislocations is consequently thought to result in a compression-tension asymmetry for single crystals [27, 52–54, 128].

Further studies by Vitek *et al*[27, 130, 131] revealed another mechanism for CRSS dependence on the sense of shear. Molecular dynamics calculations showed that the core structure of dislocations in bcc materials was altered by non-glide shear stresses (i.e. components of the shear stress which do not alter the value of the resolved shear stress defined by equation 2.4). Non-glide shear stresses can alter the CRSS differently depending on whether the applied stress is compressive or tensile. Due to a three-fold symmetry in the core structure of $\frac{1}{2}\langle 111\rangle$ screw dislocations in bcc, the change in the core structure depends on the direction of the shear stress. This change in the core structure affects the CRSS for glide of the dislocations. Unlike the twinning-antitwinning asymmetry, these changes in the core structure affect slip on all slip planes, not just glide on $\{112\}$ planes.

One might speculate that the observed tension-compression asymmetry in bcc nanopillars is related to the intrinsic non-Schmid behaviour of the dislocations. Alternately, one might argue that the effects due to the asymmetry in the γ-

surface and the altered core structures should be negligible and the mechanism should therefore be the same as for fcc materials. Here we use molecular dynamics simulations to simulate the tension-compression asymmetry in nanopillars of bcc Fe. We show that the asymmetry is due to different deformation mechanisms: dislocation glide in compression and twinning in tension.

5.2 Simulation Details

Our system consists of a pillar with a square cross-section in between two "indenter plates" as seen in figure 5.1(a). The pillars had approximate dimensions of 5.8 nm × 5.8 nm × 15.4 nm and contained 45513 atoms. The sample is confined by indenter plates, each containing 9901 atoms (12.1 nm × 12.1 nm × 0.9 nm), Movement of indenter plate atoms is constrained in order to apply external forces. The side faces of the pillar were {110} type faces and the pillars were compressed in the [001] direction. It is necessary to have {110} faces on the pillar as these are the lowest energy surfaces. Creating a pillar with higher energy surfaces will result in recrystallization during the simulation and this has been shown to create spurious deformation behaviour[75] as we saw in chapter 4.

Prior to loading, all pillars were heated to 300K by running a simulation for 50 picoseconds with a Nosé-Hoover thermostat[72, 73]. Uniaxial strain was applied by moving the indenter plates and rescaling the atomic coordinates in the direction of loading by 0.05% at 2 picosecond intervals. The resulting strain rate is $2.5\times10^{8}\ s^{-1}$. This method of compressing the system, by rescaling the coordinates of the atoms in the compression direction, is required so that a shock wave is not produced in the pillar. Since the thickness of the pillar may change through the simulation, "stress" on the sample is not easily defined: we measure the force required to hold the indenter plate in position, converted to a stress by dividing by the indenter area. As the indenter plates covered the entire upper surface of the simulation cell, the pressure on the indenter plates could simply be calculated from the component σ_{zz} of the virial stress tensor defined in equation 3.18. It is worth noting that in micropillar compression simulations, the stress in the samples is measured in a similar way to our method (i.e. by recording the force on the indenter during compression) [40]. Simulations were carried out using the MOLDY molecular dynamics code[75]. The potential function used was that developed by Hepburn and Ackland [65].

Images were created using AtomEye[77] and BallViewer [76]. Some analysis of dislocations was carried out using the OVITO package [78].

5.3 Results

5.3.1 Compression

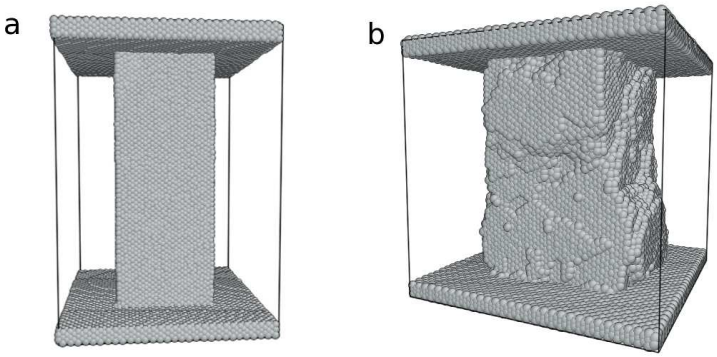

Figure 5.1 *(a)Pillar prior to applied strain. The atoms in the plates at the top and bottom of the pillar are constrained. (b) Pillar following a compressive strain of 26%*

Under compressive strain-loading, deformation in the pillars was mediated mainly by dislocation glide. Dislocations are created at the surfaces of the pillars when the stress is high and move quickly through the pillar through glide. This gives characteristic bursts of deformation leading to sudden decreases in stress. This can be seen in the graph in figure 5.2(a). As the indenter plate covered the entire upper surface of the simulation cell, this pressure was calculated simply by computing the normal component of the virial stress on the top surface of the cell (i.e. the term σ_{zz} defined in equation 3.18) Each sudden drop in pressure on the indenter plate happens when a dislocation is created and moves through the pillar, creating a discrete strain burst. Each dislocation glide event creates a step on the surface of the pillar. Figure 5.1(b) shows an image of a pillar following a strain of 26%. Many steps in the surface of the pillar due to dislocation glide activity can be seen in this figure.

The first dislocation creation event occurs at a relatively predictable strain and at a stress built up through elastic deformation. Many dislocations are created

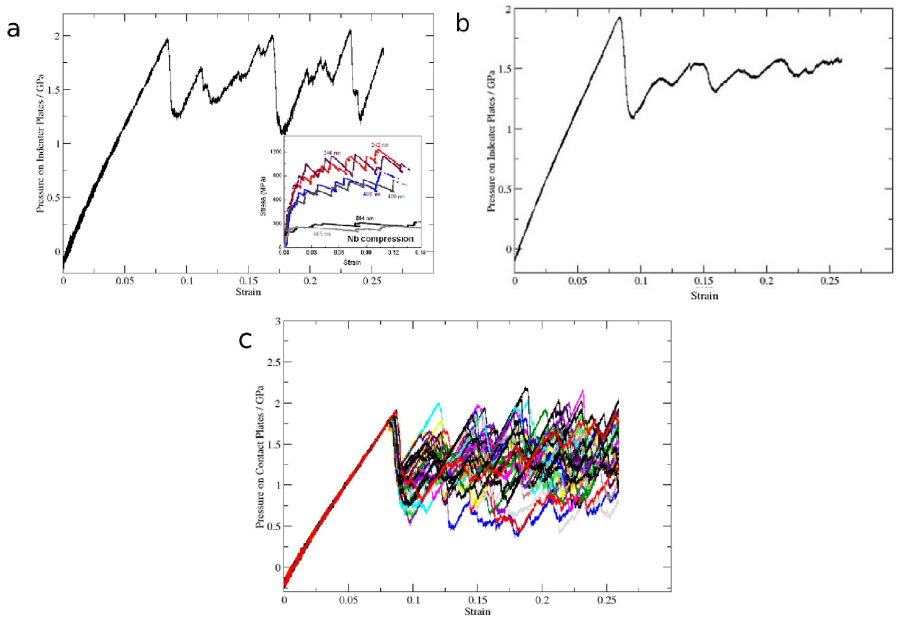

Figure 5.2 *(a) Plot of Pressure on indenter plates vs strain for pillar in compression. The inset image shows a graph of Stress vs Strain for Nb micropillar compression experiments under stress control performed by Kim et al[52]. The pressure on the indenter plates does not start at zero due to surface tension. (b) Average pressure on indenter plates vs strain over 60 pillar compression simulations. (c) Pressure on indenter plates vs strain for 60 different compression simulations on one graph.*

almost simultaneously at this point. This simultaneous dislocation nucleation event is illustrated in the sequence of images in figure 5.3 The following dislocation creation and glide events occur at less predictable points and can happen when the stress is within a range of values. This is illustrated by figure 5.2(b), which shows the stress at various strain values averaged over for 60 different pillar compression simulations, and by figure 5.2(c), which shows the pressure on the indenter plates for the 60 different simulations on the same graph. Comparing with nanopillar experiments we see similar bursts of deformation: in our *strain* controlled experiments this manifests as a sharp drop in stress at fixed strain, whereas under *stress* control the same mechanism would give sharp increase in strain at fixed stress. The experimental boundary conditions mix stress and strain control, hence the mechanism manifests as simultaneous strain increase and stress drop. The lower stresses observed for subsequent bursts is due to the roughening of the pillar having lowered the potential energy barrier for dislocation creation at the surface. The dislocation creation events after the first one typically involve the creation of just one dislocation.

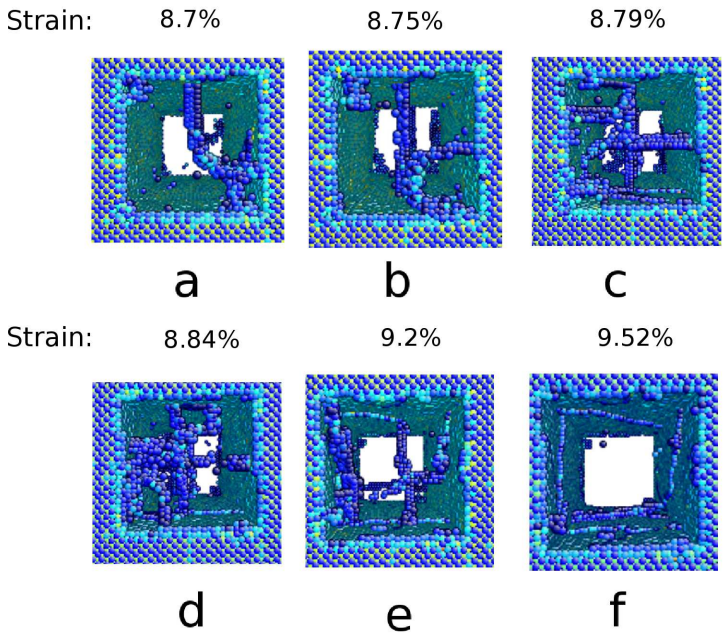

Figure 5.3 *Sequence showing the initial nucleation of dislocations in the the nanopillar. Only atoms with high centrostmmetry parameter are shown. At this point in the simulation, several dislocation lines are created simultaneously at the pillar faces. The dislocations subsequently glide until they reach another one of the pillar faces and are thus removed from the pillar. Atoms are coloured according to centrosymmetry parameter.*

The sequence of images in figure 5.4 shows a typical occurrence of dislocation glide. Dislocations are created at the corners of the pillars. Intitially the dislocation lines are curved and have a mixed edge/screw character. As the dislocation lines grow in length the dislocation line becomes straight and the dislocation has pure screw character. Each dislocation glides on many different {110} planes as a high degree of cross slip occurs. The dislocations continue to glide until they meet one of the pillar faces.

Dislocation Geometry

The compression mechanism is clearly dislocation-based. Using the *dislocation extraction algorithm* (DXA) developed by Stukowski and Albe [83] (see section 3.8.5) we find that all dislocations have $\frac{1}{2}\langle 111 \rangle$ Burgers vectors. This is the most common Burgers vector detected experimentally in bcc materials, which indicates that the potential we are using is accurately simulating dislocation glide

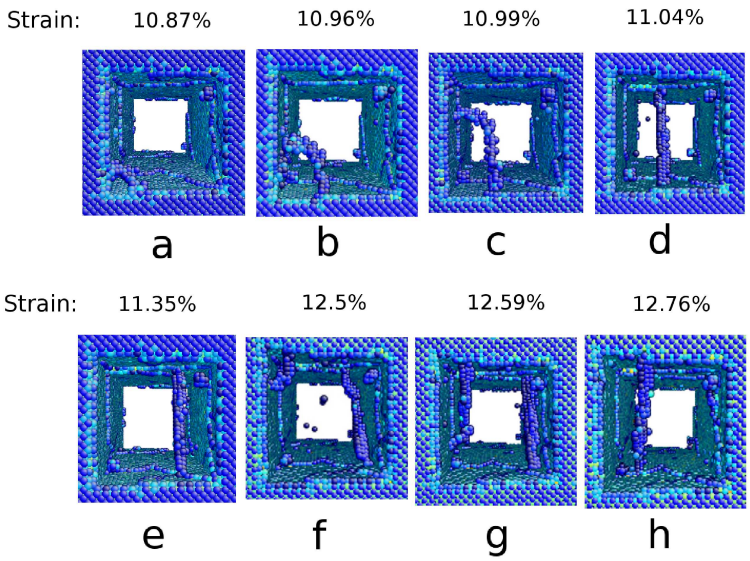

Figure 5.4 *View from the top of the pillar as a dislocation runs through the pillar. Only atoms with high centrostmmetry parameter are shown. Frames (a)-(d) show a dislocation emerge from the corner of the pillar. The dislocation initially has mixed edge and screw character. However by frame (d) the dislocation forms a straight line and has pure screw character. Frames (e)-(h) show this dislocation move through the pillar until it meets one of the sides. A second dislocation can be seen emerging from another corner from frame (f) onwards. Atoms are coloured according to centrosymmetry parameter.*

in Iron. Dislocations could also be identified by measuring centrosymmetry of nearest and second nearest neighbours of atoms with respect to the atom in question. A numerical measure of this central symmetry can be found using the centrosymmetry parameter which we have presented in section 3.8.2

Neighbour List Analysis and Slip Planes

Slip planes can be identified by comparing neighbour lists in the initial and final configurations as we have discussed in section 3.8.2. This technique was described recently by Lane *et al* [79]. We define a neighbour list containing 8 of the nearest atoms to the atom in question. When a dislocation moves on a slip plane, the nearest neighbours of each atom change. Dislocation glide causes the neighbour lists for atoms on the slip planes to change. Here we will define a "slip event" as the creation of a dislocation at one of the pillar faces and the subsequent glide of the given dislocation until it reaches another one of the pillar faces and is hence removed from the system. For bcc materials, a slip event will only change

the neighbour lists for each atom on the slip plane by 2 atoms. However, due to atomic movements, thermal motion, and stress induced changes in atomic seperations, we find a large number of atoms whose neighbour lists change by 2 atoms or more between slip events. Most of these atoms are not located on an active slip plane and this makes it difficult to resolve the active slip planes. We look at atoms whose neighbour lists change by 4 or more. Such atoms may not include all atoms on a slip plane. However, atoms with such a change in their neighbour list are more likely to be located on a slip plane or near a vacancy or interstitial and applying this criterion allows us to resolve slip planes when these atoms are imaged. Figure 5.5 shows the atoms in a pillar whose neighbour lists changed by 4 atoms or more. These atoms are concentrated on the slip bands.

The atoms in figure 5.5 do not form large close packed planes as one would expect given the neighbour list change criterion. The image identifies slip bands where numerous dislocation glide events have occured. The large degree of cross slip means that each slip band contains small segments of individual active slip planes. The slip bands have varied crystalline orientations, but a large number of them are oriented at approximately 45 ° to the direction of compression. This would allow the dislocations to travel in the direction of maximum shear stress rather than on any particular crystallographic slip plane.

Atomic strain tensor analysis confirms the interpretation that a significant amount of cross slip occurs in the sample. Slip was found to occur on a series of connected {110} planes for each dislocation. Figure 3.9 shows a cross section of the pillar following a compressive strain of 14%. Atoms are coloured according to the local atomic shear strain metric as defined in section 3.8.6. Cross sectional slices were taken across two faces of the pillar and the viewing direction is a ⟨100⟩ direction which runs diagonally through the centre of the pillar. Atoms coloured light blue and green have high local atomic shear strains and are located on slip planes on which dislocation glide has occurred. The jagged profile of these slip plane atoms indicates that a significant amount of cross slip has occurred. Closer inspection of the slip plane atoms reveals that their profile is jagged on one side of the pillar and generally straight on the other side. This is due to the orientation of the dislocations being perfect straight screw dislocations as seen in figure 6.3. The straight lines formed by the dislocation lines were always parallel to one of the side faces of the pillar and therefore the slip path cross sections seen in figure 3.9 must always be straight on one face of the pillar cross section even when a significant amount of cross slip has occurred.

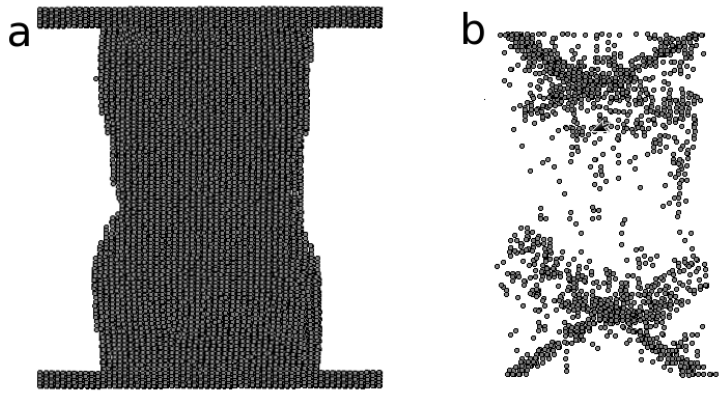

Figure 5.5 *(a)Side profile of compressed pillar following strain of 26% and (b) the same pillar showing only atoms for which the neighbour list changed by 4 or more.*

5.3.2 Tension

The deformation mechanism in the tensile case is different: it occurs by twinning. A mechanism whereby fractional dislocations with Burgers vector $\frac{1}{6}\langle 112\rangle$ move on successive planes creating a twin boundary on a $\{112\}$ plane has been described [11] and reported in similar molecular dynamics simulations recently by Li *et al* [125]. Although consistent with this mechanism, in our simulations the twin formation is very rapid, and it is not possible to identify individual fractional dislocation events. An image of a pillar following a tensile strain of 16% is shown in 5.7(a). The warped section in the middle of this pillar is the region which has twinned in a single event - as shown in the massive yield event in 5.7(b). It should be noted that this process results in the creation of $\{100\}$ surfaces on the pillar in the plastically deformed region in the centre. These surfaces are unstable and our nanosample will recrystallize if held at this strain and allowed to relax.

Twinning deformation is a more continuous and predictable process in the tensile case as shown by the plot of indenter plate pressure vs strain in figure 5.7(b). A large stress is required to create the twin, but following the initial twin creation the stress remains almost constant as more strain is applied to the pillar. This stress is lower than that required for compression.

The sequence of images in figure 5.8 shows the creation of pairs of twin boundaries during the tensile strain simulation. When the pillar first begins to deform plastically, three pairs of twin boundaries are created. As the separation between the twins in the middle of the pillar grows, the other two pairs of twins shrink in

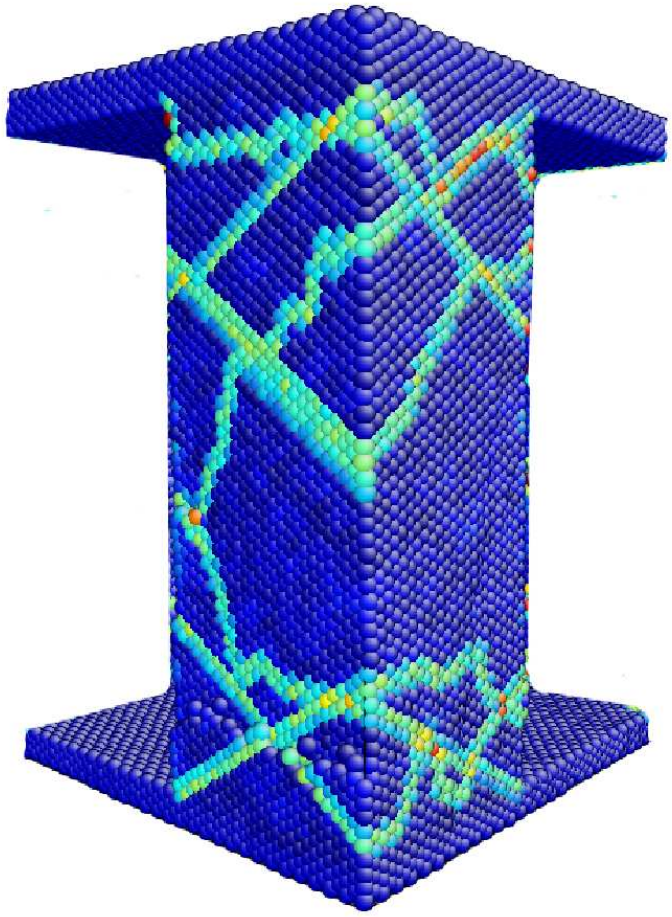

Figure 5.6 *Cross section of the pillar following a strain of 14%. Atoms are coloured according to atomic shear strain. The light blue and green atoms have high atomic shear strains while the dark blue atoms have low atomic shear strains. Note that a cross section is shown on both of the visible sides of the pillar in this image.*

size to allow the central twins to move.

5.4 Discussion

In the compressive case, our Fe pillars deform by glide of $\frac{1}{2}\langle 111\rangle$ dislocations on slip planes. This is consistent with much experimental evidence including that of Kim and Greer [52–54, 126] which showed bursts of dislocation motion punctuated by periods of rising stress (as shown by the inset in figure 5.2(a)). There are some differences in the behaviour between our MD simulations and experimental results. Experimental results for compression of bcc nanopillars often reveal strain

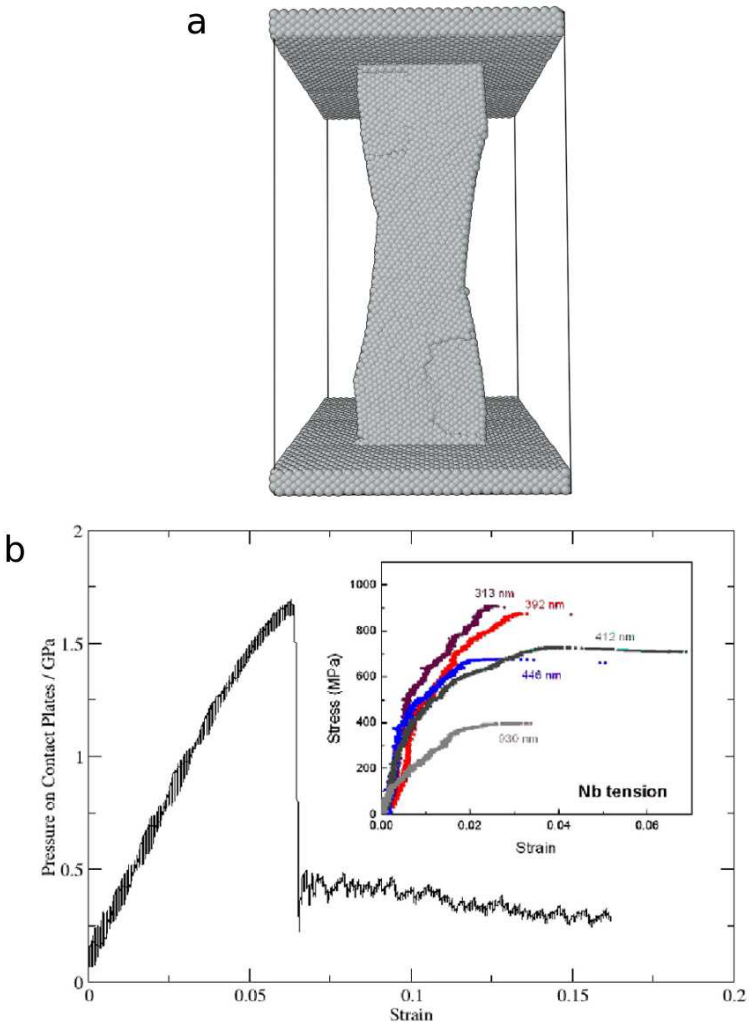

Figure 5.7 *(a) Image of pillar following strain of 16%. (b) Pressure on intenter plates vs strain for pillar tension. The inset image shows a graph of Stress vs. Strain for micopillar tension experimants on Nb performed by Kim et al[52].*

bursts in the stress vs strain behaviour. In contrast we see a series of sudden stress drops. This is mainly due to the boundary conditions: we use strain control which means that events involving large strain are impossible. There may be some difference due to the small size of our pillars, the high strain rates which we have to work with in MD: in particular the surface-driven recrystallization may well be a size effect. It is not clear whether indentation in the experiments by Kim and Greer was performed with load control or strain control. This was not specified in the relevant publications and the stress vs strain signature shown in the inset in the inset in figure 5.2 (a) seems to show signs of a response to both an applied load and an applied strain.

Very large steps on the surface of compressed nanopillars in experiments indicate that many dislocations glide on the same slip plane. It is likely that this is due to the presence of dislocation sources which provide many dislocations on certain slip planes. This does not happen in our simulations due to high levels of cross slip and a lack of dislocation sources in our pillars. This may be a result of our high strain rates, which allow sufficient stress to build up to nucleate additional dislocation sources before the first source can release the stress. The fact that figure 5.2(a) shows the stress sometimes returning to the value required to initiate the first dislocation supports this interpretation.

In the tensile case, the twinning we observe is a possible mechanism by which the necking seen in Kim and Greer's experiments could occur. The long periods of constant flow stress observed in these experiments corresponds to that seen in simulations which is illustrated in figure 5.7(b). The biggest difference between simulations and experiment in this case is the large initial stress required to nucleate the twin in our simulations. This is because, unlike the experiments, we have an atomically-flat surface, on a dislocation free sample. Such high yield stresses are observed in experiments on so called single-crystal whiskers. These whiskers are long filaments of single crystal which are typically a few microns in length but can have diameters as small as 20 nm [132].

The twinning-antitwinning asymmetry is not present in fcc crystals as formation of twins is not mediated by fractional dislocations as in bcc materials. The change in the core structure under stress in bcc materials is dependent on the presence of edge components in fractional dislocations[27]. Due to the lack of fractional dislocations in fcc materials, this effect is not observed in fcc materials. For these reasons we would not expect to see a compression-tension asymmetry in fcc caused by these deformation mechanisms.

5.5 Conclusion

We have performed molecular dynamics simulations of nanoscale Iron pillars subject to compressive and tensile strains. A deformation mechanism asymmetry has been observed between tension and compression. In the compressive case, plastic deformation is mediated by dislocations. Plastic deformation occurs in discrete bursts when one or more dislocations are created at the pillar surfaces and move through the pillar by glide. A large amount of cross slip is observed

in this deformation regime allowing for the dislocations to move in the direction of maximum shear stress. By contrast, in the tensile case deformation occurs through the creation of twin boundaries. This is consistent with asymmetry observed in various experiments.

This compression-tension asymmetry could potentially be exploited to improve the performance of high speed cutting apparatuses. FEM simulations have revealed that a complicated distribution of tensile and compressive stresses is present in a chip during high speed cutting [57, 133]. The stress distribution in the chip has also been found to depend on the shape of the cutting tool used [134]. We found that the stresses required to deform nanopillars of Fe were lower in tension than in compression. It may therefore be beneficial to design a cutting tool which maximises the amount of tensile stress in a chip during the chip formation process. FEM simulations could potentially be used to determine the optimal cutting tool design.

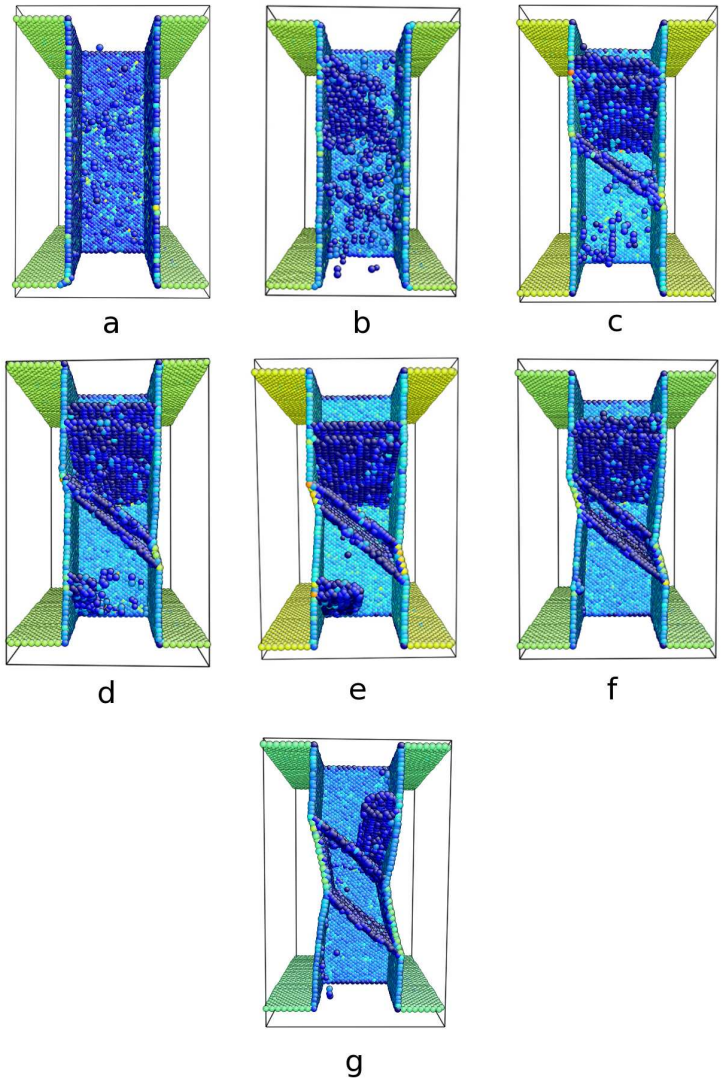

Figure 5.8 *Side view cross section of the pillar during tension. Atoms are coloured according to centrosymmetry parameter. Only atoms with high centrosymmetry parameter are shown. Frames (a)-(f) show the creation of three pairs of twin boundaries following 7% tensile strain. The pair of twin boundaries near the bottom of the pillar move towards each other until they meet and are hence eliminated from the pillar. This allows the distance between the pair of twins in the middle of the pillar to grow. The pair of twins at the top of the pillar begin to shrink as more tension is applied. This can be seen in frame (g) which shows the pillar following 11% tensile strain.*

Chapter 6

Plasticity in Nanopillars of FCC Cu

6.1 Introduction

As we found out in chapter 4, fcc nanopillars have displayed a wide range of different plasticity behaviours in MD simulations. While some studies have reported amorphous regions in the pillars during deformation [3, 93, 94], others have reported deformation to occur through twinning [135–137] and dislocation glide [113, 114, 123]. Some simulations have also reported surface reconstruction during plastic deformation [124, 138]. Pillars of Cu, for example, have been reported to deform by amorphization [135], slip [138], and twinning [137]. Some of these differences may be due to the geometry and scale of the pillars as well as differences in strain rates and deformation methods. We have seen in chapter 4 that the way in which strain is applied can affect the deformation mechanisms. We also saw in that chapter that constructing pillars with high energy surfaces can give dubious results. This is paticularly noteworthy as few of the published studies on MD simulations of fcc pillars use pillars with stable {111} surfaces on the faces of the pillars. Several studies have reported surface reconstruction during deformation of pillars with square cross sections and {100} face surfaces. This suggests that surface effects due to the presence of these high energy surfaces can strongly affect the outcome of the plasticity.

Here we have carried out simulations of compressive and tensile strains on a Cu nanopillar with {111} face surfaces. These simulations should show deformation mechanisms which are more likely to resemble those seen experimentally in

plasticity of nanowires, nanopillars, and micropillars. We choose to simulate Cu as a model fcc material due to the availabilty of a high quality and well understood potential function [67, 75].

6.2 Simulations

Our system consisted of a pillar of Cu atoms with {111} side faces. The pillar therefore had a parallelogram-shaped cross section. The pillar was placed in between two 'indenter plates' which consisted of constrained atoms. Constrained atoms are necessary as they provide external forces to the system and prevent any conservation of momentum effects effects like those described in section 4.2.1. The side faces of the pillar were 8 nm in width and the pillar was 18 nm in length. The system consequently contained 97547 atoms. The indenter plates also had a parallelogram shaped cross section. The sides of each plate were 16 nm long and each plate was 2 nm thick. Each indenter plate contained 12168 atoms. An image of the pillar prior to deformation can be seen in figure 6.1 (a). This pillar construction has a slightly higher energy than the Wulff construction for this pillar. However, the difference in energy should be small and the time taken before reconstruction will be very large as moving individual atoms from the corners of the pillar is not energetically favourable. Construction a Wulff construction for the pillar would require calculating surface free energies for the various crystallographic surfaces (at the desired temperature) exposed on the faces of the pillar. The structure which minimised the free energy of the system could then be determined [139]. This structure will depend on the potential function used as surface energies can differ, even between potential functions designed to simulate the same material. Finding a global equilibrium structure is further complicated by the fact that the presence of twin boundaries in a nanostructure can lower the energy of the structure by allowing more low energy surfaces to be present on the structure [140]. For the sake of simplicity, we restrict out focus in this study to the nanopillar structure containing only {111} side faces.

Prior to compressive and tensile straining, the pillars were heated to 300K via a Nosé-Hoover thermostat[72, 73]. Compressive and tensile straining were also carried out at 300K. Uniaxial strain was applied by moving the indenter plates and rescaling the atomic coordinates in the direction of loading by 0.05% at 2 picosecond intervals. The resulting strain rate is $2.5\times10^{8}\ s^{-1}$. This method

of compressing the system, by rescaling the coordinates of the atoms in the compression direction, is required so that a shock wave is not produced in the pillar. As described in section 5.2, we measure pressure on the indenter plate surfaces as stress is not easy to define stress in the sample due to the changing width of the pillar. Simulations were carried out using the MOLDY program [75] and the potential used was a Finnis-Sinclair potential fitted to the properties of copper and developed by Ackland *et al* [67]. Note that copper has a relatively low stacking fault energy and the stable dislocation for bulk copper is a $\frac{1}{2}\langle 110\rangle$ dislocation split into two Shockley partials to form an extended dislocation. These features of copper are accurately represented in the potential just mentioned [67].

Images were created using AtomEye[77] and BallViewer [76]. Some analysis of dislocations was carried out using the OVITO package [78].

6.2.1 Compression

We find that, in compression, plasticity occurs through glide of Shockley partials on $\{111\}$ planes. Stacking faults are thereby created on the $\{111\}$ planes on which slip occurs. Dislocations were identified using the Dislocation Extraction Algorithm described in section 3.8.5. Stacking faults were identified by looking for atoms with significantly high centrosymmetry parameter as described in section 3.8.3. Partials are created at the obtuse angled corners where two surface faces of the pillar meet as illustrated in figure 6.2. The shape of the pillar prior to compression and at a strain of 22% can be seen in figure 6.1. All dislocation glide events occured on a small number of $\{111\}$ planes located near the the indenter plates. This may be the result of higher stresses near the indenter plates as atoms in the indenter plates are constrained and do not relax in between loading steps. This results in atoms in the indenter plates being slightly closer together. However, we note that Diao *et al* also found slip to be confined to slip planes near the ends of compressed nanowires of gold, despite not placing any constrained atoms in the nanowires [115]. As the number of active slip planes was small, several dislocations moved on each slip plane. As a result of this, stacking faults were created and destroyed by the movement of partials on these planes several times over the course of the compression.

Figure 6.3 shows a cross-section of the pillar taken over the course of the compression simulation, showing only atoms with a centrosymmetry parameter significantly greater than zero. One can see the creation and subsequent removal

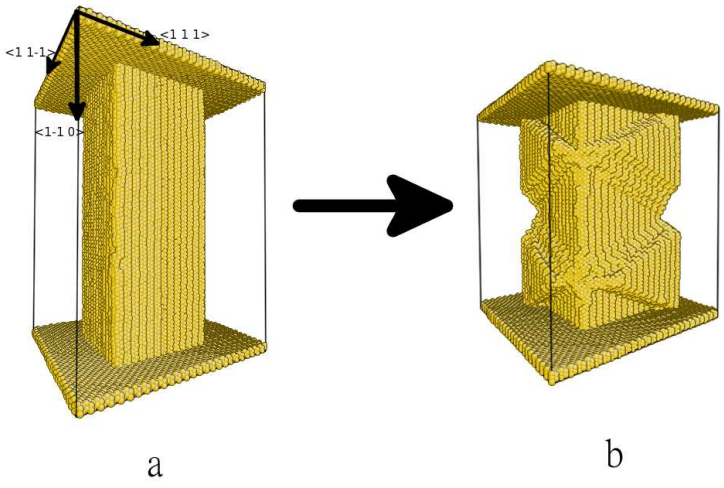

Figure 6.1 *(a) Initial configuration of pillar and indenter plates. (b) Pillar following a compressive strain of 22%.*

of stacking faults in this sequence. In figure 6.3 (c), one can see short segments of stacking fault near the corners of the pillar. These stacking faults are bounded by Shockley partials and the surfaces of the pillar. In figure 6.3 (d), one can see the removal of a stacking fault by the movement of a Shockley partial across a plane containing a stacking fault.

The stress vs strain signature is characterised by increasing stress as the pillar is compressed followed by sudden decreases in the stress when a dislocation is generated and moves through the pillar. This can be seen in figure 6.4.

6.2.2 Tension

In tension, plasticity is relatively similar to that seen in compression. In contrast to the compressive case, there are many more active slip planes spread more evenly throughout the pillar. Figure 6.5 shows the initial shape of the pillar and the pillar after 28% tensile strain. The reasons for the high number of active slip planes in tension remain unclear. However, these results are consistent with results obtained by Diao *et al* [115].

As there are many more active {111} slip planes in tension, a given plane is less likely to see more than one dislocation traverse it and the pillar consequently contains many more stacking faults at any given time in the later stages of the compression. In addition to this, a number of vacancies are created as the tensile

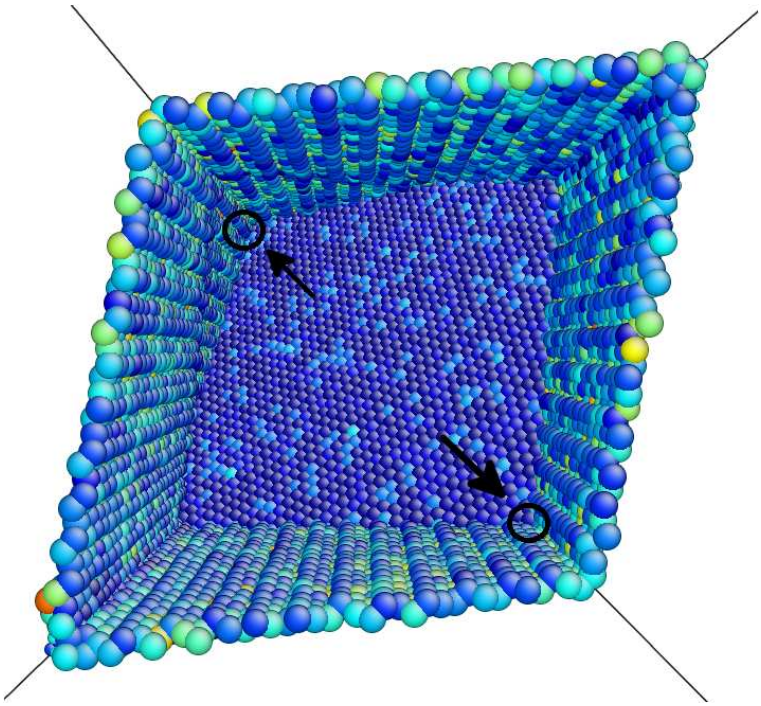

Figure 6.2 *Top view cross section of the pillar following 10% compressive strain. Only images with high centrosymmetry parameter are shown. Atoms are coloured according to centrosymmery parameter. A stacking fault on a* $\{111\}$ *can be seen in the pillar. This was the result of glide of a Shockley partial on this plane. The obtuse angled edges of the pillar from which dislocations are created are indicated by circles and arrows.*

strain is applied. These defects are illustrated in the centrosymmetry profiles shown in figure 6.6.

The stress vs strain signature is shown in figure 6.7. The behaviour is qualitavely similar to that in the compression case with a series of sudden decreases in the stress value corresponding to glide of a single dislocation through the pillar. However the indenter plate pressure immediately prior to glide of a dislocation is about half of its corresponding value for compression case. This may be partly due to the changing width of the pillar. During the tension simulation necking occurs in the regions where most of the plasticity occurs. This means that while the yield stress for dislocation glide may remain constant, the pressure on the indenter plates at the yield points may change.

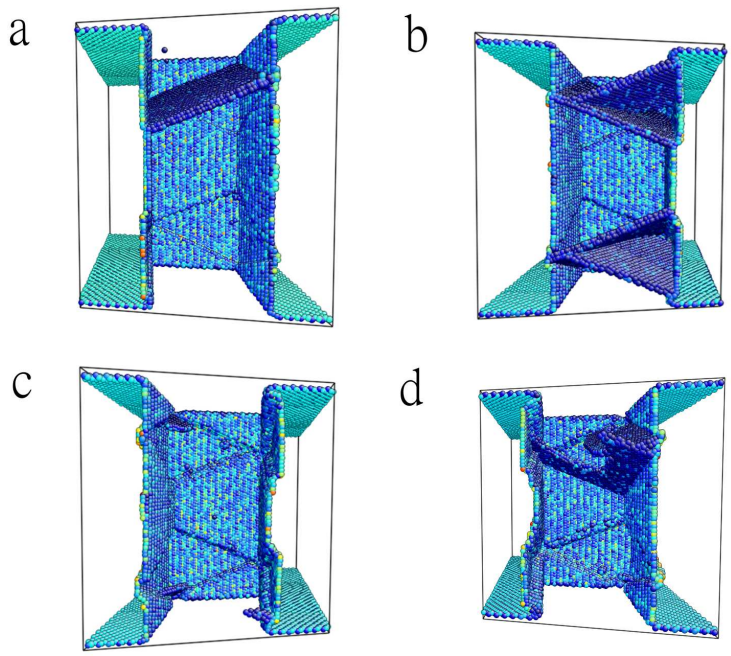

Figure 6.3 *Images of pillar following compressive strains of (a) 5%, (b)10%, (c)15%, and (d) 18%. Atoms are coloured according to centrosymmetry parameter and only atoms with high centrosymmetry parameter are shown. The glide of partials creates stacking faults in the pillar. Partials which glide over existing stacking fault planes remove the stacking fault. Small segments of stacking fault near the edges in image (c) indicate the emergence of partials from these edges. In image (d) movement of a partial across an existing stacking fault plane is removing this stacking fault while a dislocation emerging from of the top corners of the pillar is creating a new stacking fault.*

6.3 Discussion

The pillar we created was relatively simple in construction but is not the low energy Wulff construction for an fcc pillar. The pillar we have constructed should, however, be relatively stable for the following reasons. Reconstruction to Wulff structure requires movement of atoms from the acute angled edge to create a {110} face. Movement of single atoms from this edge are not energetically favourable. This means that reconstruction requires simultaneous movement of a line of atoms from the edge. The time to relaxation to the Wulff shape is therefore very large in practice. The lack of surface reconstruction over the course of our simulations, unlike previous studies [75, 124, 138], confirms that the pillar structure is stable with its {111} faces. In section 4.2.2, we found that

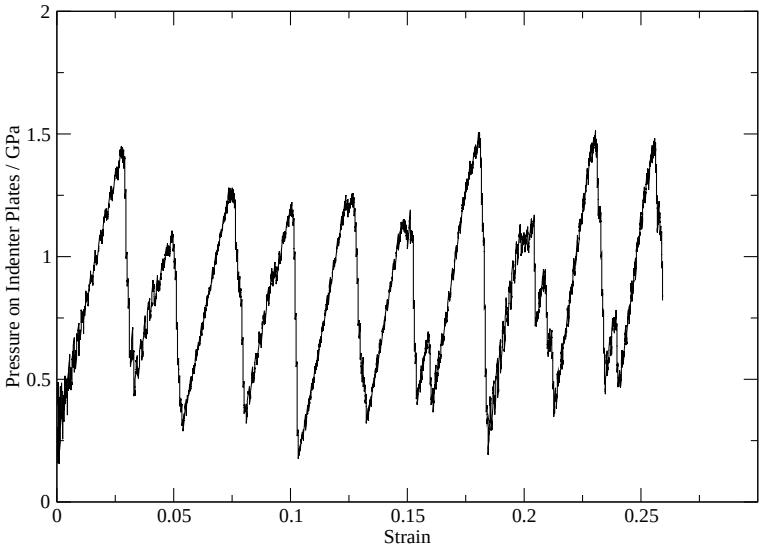

Figure 6.4 *Plot of pressure on indenter plates vs strain for pillar in compression. The pressure on the indenter plates increases with strain until a dislocation is created at one of the edges of the pillar. The pressure then drops as the dislocation moves through the pillar and the pillar deforms plastically.*

the type of faces a nanopillar was constructed with had a significant impact on the deformation mechanisms in the nanipillar when it was compressed. Nanopillars of bcc Fe with high energy {100} side faces were found to deform by amorphisation while pillars with stable {100} side faces deformed by dislocation glide. We therefore expect that the results of the nanopillar compression presented in this chapter will more closely resemble experimental results as we constructed our pillars with low energy {111} faces. Previous molecular dynamics studies on fcc nanopillars (detailed in section 4.3) reported a wide range of different plasticity behaviours but were based on nanopillars with high energy surfaces.

The plasticity behaviour of these pillars is relatively similar in tension and compression, at least qualitatively. The yield stress is lower and more vacancies are created in tension. Slip is restricted to a few slip planes near the indenter plates in the compressive case.

These results differ to some previous studies of nanopillars and nanowires of Cu (and other fcc materials) with Molecular Dynamics. We do not see amorphous regions appearing as found by Wang *et al* [141]. Their use of pillars with unstable {100} surfaces in this study is likely to have caused, at least in part, this deformation by amorphization behaviour. However, the small size of the pillars and the higher strain rate ($1.3\times10^9\ s^{-1}$) used in this study may also have played a

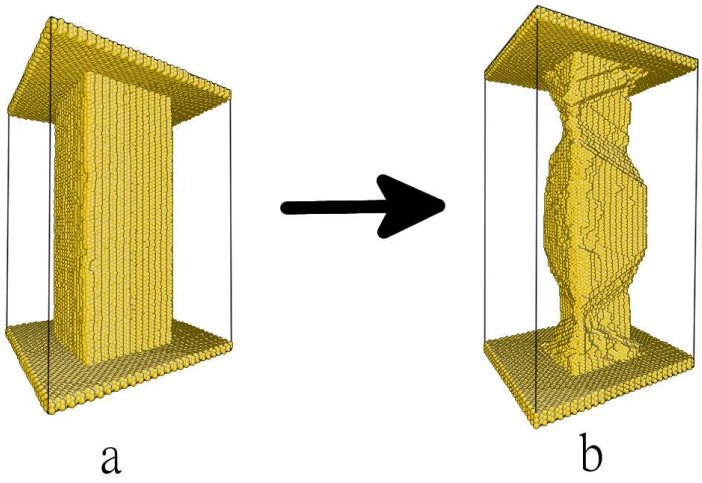

Figure 6.5 *(a) Initial configuration of pillar and indenter plates. (b) Pillar following a tensile strain of 28%.*

part in causing this plasticity behaviour. We also don't see deformation by surface reconstruction as seen previously [124, 138]. This is a result of construction of stable surfaces on the faces of the pillar.

The previous study which demonstrates results most like those seen above is that by Cao and Ma [123]. They used pillars with unstable surfaces. However, they saw deformation by dislocation glide. In compression, glide of full {110} dislocations. In tension, they saw glide of Shockley partials. The paper presents a convincing explanation for this compression-tension asymmetry. The orientation of their pillars and the dislocation behaviour they observed was such that the slip system for the leading partial had a lower Schmid factor than that for the trailing partial. This meant that as soon as the leading partial was nucleated, the stress was high enough to nucleate the trailing partial immediately afterwards. The leading and trailing partials were then so close together that, they effectively constituted a full dislocation. We do not see this asymmetry. This is likely due to the orientation of our pillars. However, one can't eliminate the possibility that the unstable structures of the pillars in the Cao and Ma study may have played a part in the obeserved behaviour, paticularly when, like in our simulations, dislocations were created at the edges of the pillars.

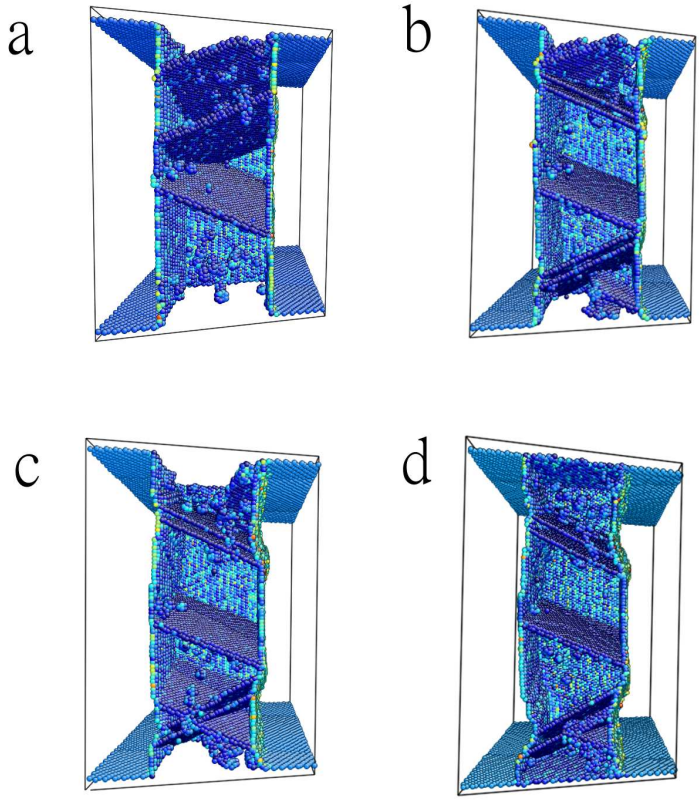

Figure 6.6 *Images of pillar following tensile strains of (a) 5%, (b)11%, (c)16%, and (d) 22%. Atoms are coloured according to centrosymmetry parameter and only atoms with high centrosymmetry parameter are shown. The point defects in the pillars are vacancies. In tension, dislocations are found to glide on slip planes throughout the pillar, unlike in comression where the slip all occurs on planes located near the ends of the pillar.*

6.4 Conclusion

We have performed MD simulations of tensile and compressive strains applied to a nanopillar of Cu. The nanopillar was constructed with low energy {111} surfaces. We find that plasticity is mediated by glide of Shockley partials on {111} planes. The stress-strain signature differs slightly in tension from that of compression and we find that the yield stress in tension is lower. However, there is no qualitative difference between deformation mechanisms in the tensile case and those in the compressive case. This distinguishes fcc nanopillars from their bcc counterparts. We also find that many vacancies are created in the pillar during the tension simulations.

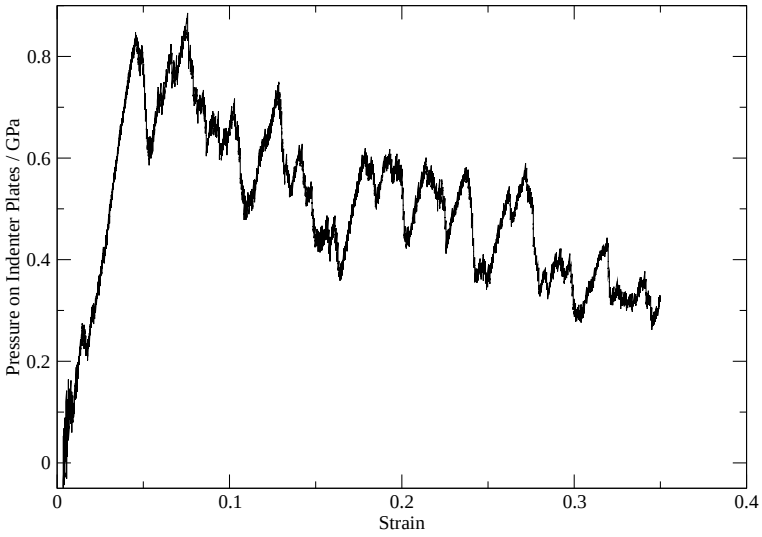

Figure 6.7 *Plot of pressure on indenter plates vs strain for pillar in tension. The yield stress differs from the compressive case and the profile looks slightly different from the compressive case. However, the qualitative behaviour is the same with sudden drops in pressure corresponding to dislocation glide events. The pressure immediately prior to dislocation glide events changes during the simulation. This may be due to necking in the regions where the plasticity takes place, because the ratio of the stress on the sample to indenter pressure is proportional to the ratio between the indenter plate area and the and the sample cross section. If the sample gets smaller, the sample stress increases even if indenter pressure is constant.*

If vacancies are present in regions of fcc crystals which have been subject to tensile strains, then the vacancy concentration could be a useful proxy for local tensile strain in experiments. This is particularly significant when one considers the compression-tension asymmetry found in the bcc nanopillars in the previous chapter. Designing cutting tools which take advantage of the compression-tension asymmetry would require an understanding of the distribution of local compressive and tensile strains in machining chips. If regions of local tensile strain could be identified in a material, that material could be used to test cutting tools to see how much local tensile strain is delivered to the machined material during chip formation.

Chapter 7

Plasticity of Nanocrystalline Fe

7.1 Introduction

There have now been numerous studies carried out involving atomistic simulations of polycrystalline materials under compression [142–150]. The majority of these studies have been on compression of fcc materials. Most notably, Van Swygenhoven and others have contributed a large amount to this area of research [142, 143, 148–150]. Due to length limitations in molecular dynamics, grain sizes are limited to the nanocrystalline regime. Plasticity has been found to occur through a combination of grain boundary sliding and dislocation glide [151]. Dislocations are emitted from the grain boundaries and are generally absorbed by grain boundaries after traversing a grain by glide [152]. As grain boundaries inhibit the motion of dislocations, small grain sizes limit the amount of plastic deformation which can occur by dislocation glide and hence make the materials harder. However, below a critical grain size (20 nm in Cu for example) the simulated nanocrystalline samples begin to become softer with decreasing grain size. This trend reversal is due to a shift in the dominant deformation mechanism from dislocation glide to grain boundary sliding when the grain size drops below the critical value. This effect was first observed in molecular dynamics simulations by Shiotz *et al* [153] As the grain boundaries become smaller the fraction of grain boundary atoms in the sample increases. The large amount of grain boundary surface in samples with small grain size can accommodate more grain boundary sliding, leading to the observed softening effect. These simulation results agree with experimental observations in nanocrystalline metals [154].

The amount of published work on plasticity of bcc polycrystalline samples is more limited. Most of the previously reported simulations of bcc polycrystals have applied compression and tension to the samples in such a way that the volume of the MD cell changes [86, 87, 155, 156]. In tension, this results in fracture occuring to create free space in the cell to fill the additional volume [87, 155, 156]. In compression, it results in pressure in the MD cell reaching 60 GPa or more [86, 156]. In both tension and compression, these simulations demonstrated significant levels of grain boundary sliding and recrystallization. A far more common case in nature and in industry is shear strain where the overall volume of the sample is conserved. The only study which applied strain to a polycrystalline sample of a bcc material which allowed the shape of the cell to change, while fixing the volume, was that by Pan *et al* [157]. They applied tensile strain along one axis while allowing the cell to expand at constant pressure along the other two axes. In this study fracture was also observed in the material.

In these molecular dynamics studies of nanocrystalline bcc metals, deformation was found to occur through a combination of dislocation glide, twinning, and grain boundary sliding [156]. Similarly to fcc nanocrystalline samples, the dominant deformation mechanism is found to change from dislocation glide to grain boundary sliding below a critical grain size and the samples soften as the grain size decreases below this critical size [88].

Applying shear while conserving the volume of the cell may be particularly relevant to plasticity in shear bands formed during high strain rate deformation of metals. These shear bands are particularly relevant to machining processes in metals. During high speed cutting, metal chips which are produced containing many shear bands [34, 158]. The type of shear band which forms strongly influences the macroscopic form of the chip. So called continuous chips result when shear bands are closer together and the amount of shear in each shear band is small [158]. These chips remain attached to the bulk for a long time and can grow to metres in length. Segmented chips on the other hand usually have more or less constant spacing between shear bands [34, 158]. Shear bands in segmented chips are spaced further apart and each shear band typically acounts for more shear than shear bands in continuous chips. These chips break from the bulk material frequently resulting in many chips which are short in length. As discussed in section 2.7.2, the type of chip which forms during machining processes has significant practical impacts on the machining process. Images of a continuous and a segmented chip of a Ti V15 Al3 Cr3 Sn3 alloy can be seen in

figure 7.1.

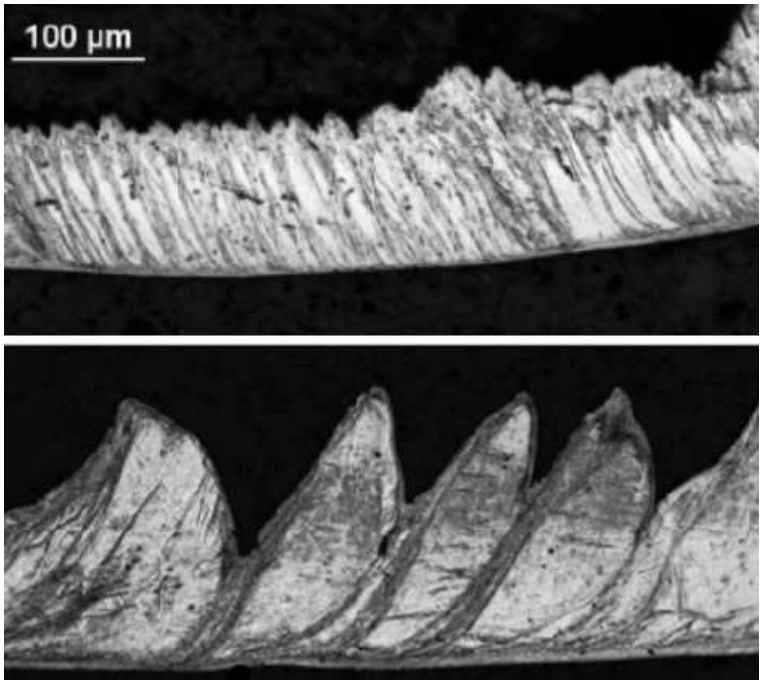

Figure 7.1 *Images of continuous (top) and segmented (bottom) chips of Ti V15 Al3 Cr3 Sn3 alloy produced during a high speed cutting experiment. Image courtesy of Pawel Rockicki.*

Experimentally, investigating plasticity in shear bands is difficult to do in situ. In practice, all analyses on shear bands are carried out after the deformation has occured [34, 158]. At this point the shear bands have cooled significantly and the microstructure in the shear band will have altered as a result. This is of particular significance in Ti alloys where thermal conduction of heat is poor and local temperatures in the shear band may therefore vary considerably.

A wide variety of microstructures have been found in shear bands in machining chips [34, 159] and in shear bands from Split-Hopkinson bar experiments [160–162]. Some shear bands consist of grains which are elongated in the direction of shear [159, 162]. Others contain fine grained and nanograined microstructures [34]. In Hopkinson-split bar experiments, stainless steel has been found to contain amorphous material with nanoscale crystallites embedded within [160, 161]. In bcc materials, shear bands have been reported as containing elongated grains and nanograined microstructures. An image of a shear band from a study by Siemers *et al* [34] of machining chips of a bcc Ti V15 Al3 Cr3 Sn3 alloy can be seen in figure 7.2. In this study, the shear bands were found to consist of nanocrystalline material.

Here we carry out molecular dynamics simulations of pure shear on a polycrystalline sample of Fe. We chose Fe as a model bcc material due to the availability of a high quality and well understood potential function for this material [65, 163]. We carry out simulations at five different temperatures (300K, 600K, 900K, 1200K, and 1500K). Local temperatures can vary significantly in a shear band during chip formation [57] and temperatures as high as 1300K are thought to be reached in parts of the shear bands of bcc alloys of Ti [34]. We test an array of temperatures to get a good overview of plasticity behaviour at high strain rates. We start with a cubic MD cell 23nm in length. This is much smaller than the width of a shear band which is typically $\sim 5\mu m$ [34]. Our system therefore represents a small part within a shear band. Plasticity within shear bands this small is difficult to study experimentally and is impossible to resolve in FEM simulations as a single element in an FEM simulation is usually far bigger than $\sim 5\mu m$ in size. We find that for high temperatures (1200K and 1500K), the deformation mechanisms change. At these temperatures, twinning and dislocation glide are rare and the plasticity is dominated by grain boundary sliding and recrystallization. At high strains and at these temperatures, the deformation is characterized by amorphization and movement of crystalline segments through amorphous regions in the cell. Amorphization has previously been demonstrated in MD simulations of fcc nanowires when they are subject to high strain rates. However, this is the first time to our knowledge that amorphization has been observed in a bcc material or a polycrystalline material in MD simulations.

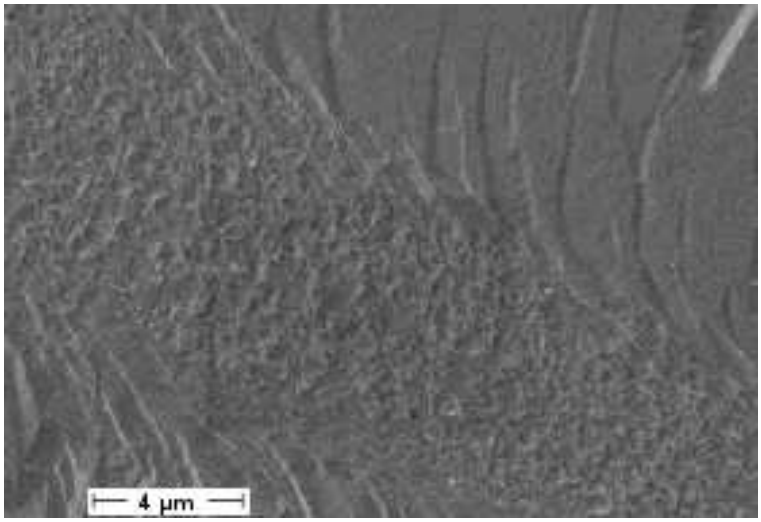

Figure 7.2 *Image of shear band in a bcc Ti V15 Al3 Cr3 Sn3 alloy produced during a high speed cutting experiment. The shear band consists of nanocrystalline material. Image produced by Siemers et al [34]*

7.2 Results

7.2.1 Creation of Polycrystalline Sample

To create a nanocrystalline sample, a single crystal sample of Fe with dimensions of 23 nm by 23 nm by 23 nm and consequently containing 1024000 atoms was first created. Periodic boundary conditions were applied in all directions and the sample was heated to 2000 K using a Nosé-Hoover thermostat until the system consisted of melted Fe.

The simulation was then stopped and the system was altered by removing clusters of atoms within the sample. 30 randomly located points were then chosen within the simulation cell. At each of these randomly chosen points, a small piece of crystalline Fe was then introduced. These small pieces of crystalline Fe consisted of 48 atoms and measured 0.5 nm by 1.4 nm by 0.8 nm. Each of these crystallites had a random crystalline orientation in the cell. The crystallites act as nucleation sites for crystal growth as the system is cooled down, producing a solid with many crystal grains. Atoms from the melted part of the system were removed if they were located within 2.5Å of an inserted crystalline atom. This was necessary as placing atoms closer together will produce enough energy to melt the introduced pieces of crystalline Fe before the thermostat has a chance to cool the system back to a solid state.

The sample was first cooled at 1000K (note that the melting temperature for this potential is 1772K) for 80 ps until a clear grain structure could be seen. The system was then cooled further to 300K for 10 ps. Performing the crystallisation at the relatively high temperature of 1000K ensures that the velocities of the atoms during the crytallization process were large enought to bring the system to a solid phase in a managable timescale for molecular dynamics. Figure 7.3 shows a cross section of the system after the crystallisation process was completed. Many $\frac{1}{2} < 111 >$ dislocations were created in the sample during the crystallization. The average grain size in the sample was approximtely 7 nm. This grain size is similar to that of some recently developed nanocrystalline alloys [164]. However, grain sizes in coarse grained metals used for machining typically have grain sizes in the order of tens of microns [11, 34].

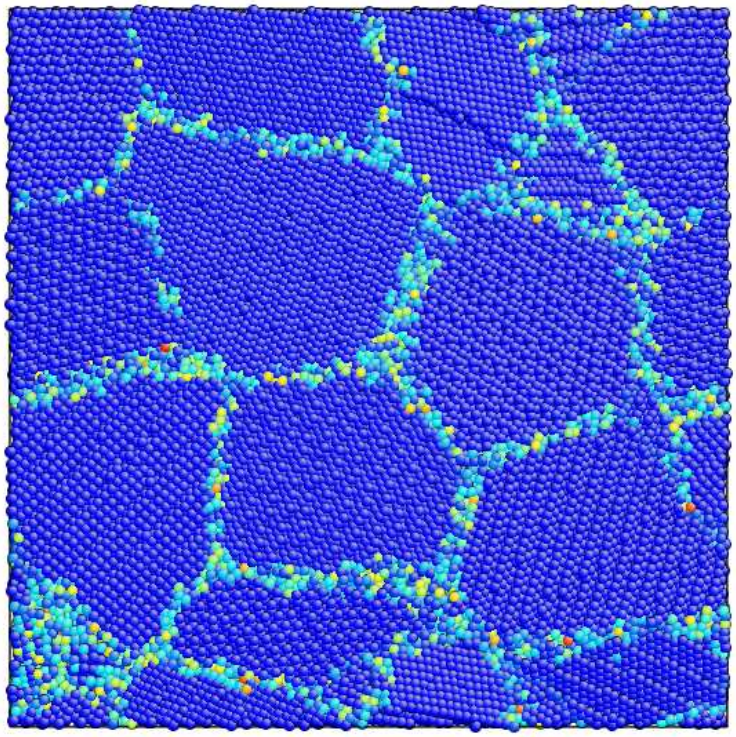

Figure 7.3 *Cross section of the polycrystalline structure after cooling to 300K. Atoms are coloured according to centrosymmetry parameter. The average grain size is ∼7nm. This grain size is similar to those in some nanocrystalline alloys [164]. However, grain sizes in coarse grained metals typically used for machining have grain sizes in the order of tens of microns [11, 34].*

7.2.2 Simulation Details

We performed simulations of pure shear on the system detailed above. We performed this shear simulation at temperatures of 300K, 600K, 900K, 1200K, and 1500K.

We applied pure shear to our system[165]. This is the shear which results from uniaxially compressing a system. Pure shear is illustrated in figure 7.4. Consider the black rectangle in this image. When this rectangle is compressed in the direction represented by the red arrows, then a shear strain is applied in the direction of the blue arrows. When we refer to the strain in these simulations, we refer to the fractional change in the length of the system in the direction of compression. Shear was applied by rescaling the y and z coordinates periodically during the simulations. The simulation cell was also rescaled in this manner allowing periodic boundary conditions to be preserved throughout the

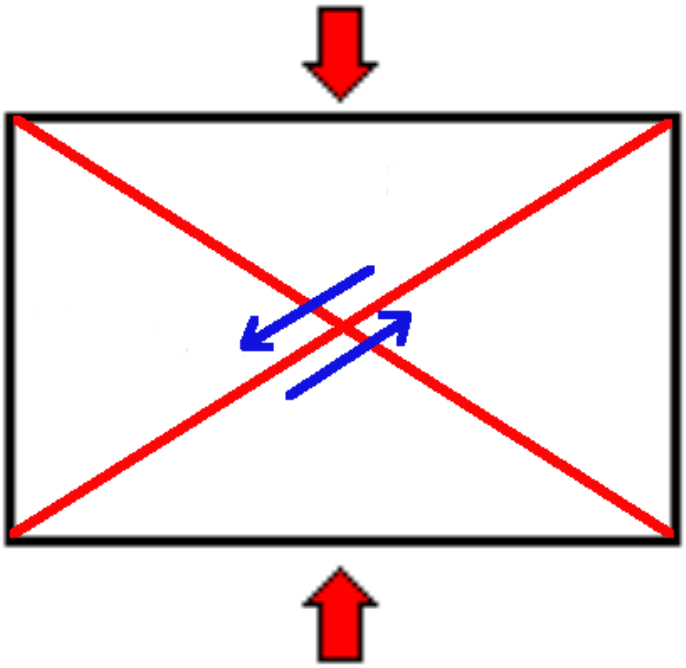

Figure 7.4 *Illustration of pure shear. If the black rectangle is compressed in the direction of the red arrows, then shear occurs in the directions of the blue arrows.*

simulation. Strain increments were applied at 2 ps intervals and were applied by multiplying the z coordinates by 0.9995 and the y coordinates by 1.0005 at each increment. The applied strain rate was consequently 2.5×10^{8} s^{-1}. This is close to experimental values of strain rate within the shear band which are known to be a minimum of $10^{7}s^{-1}$, but cannot be measured effectively [34]. This method of applying strain allows for a strain to be applied without introducing shock waves in the system [166]. As there are no constrained atoms in the system, we cannot avoid conservation of momentum effects in this simulation like those described in chapter 4. However, introducing constrained atoms to this system would either break the periodic boundary conditions or create a region in the system which would be prohibited from deforming plastically. Furthermore, there are no obvious constraints on the final morphology of this system due to the lack of constrained atoms in the system.

We continued to apply periodic boundary conditions during these simulations. The timestep used was 1 fs and the Nosé-Hoover coupling parameter was 1000. The potential used was that developed by Hepburn and Ackland [65].

7.2.3 Low Temperature Plasticity

Plasticity behaviour during the simulations at 300K, 600K, and 900K were similar. Deformation occurs through a variety of mechanisms including slip, twinning, recrystallization, and grain boundary sliding. Figure 7.5 shows some twins and dislocations present in the sample as a result of the deformation.

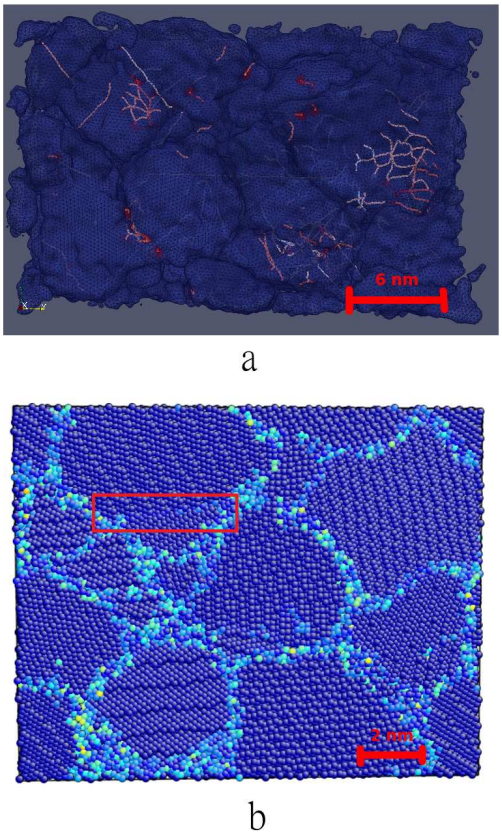

Figure 7.5 *Images of the sample following strain of 20%. Both images show the same sample. (a) shows the output from DXA analysis on the sample imaged using Paraview. (b) shows a cross section of the system imaged using Atomeye. These images illustrate the presence of dislocations and twins in the sample. In (a) the red and pink lines are* $\frac{1}{2} < 111 >$ *dislocations and the blue surfaces are grain boundaries. This is a 3 dimensional image and the blue surfaces representing the grain boundaries are partially transparent. These defects were detected by the DXA algorithm. In (b) atoms are coloured according to centrosymmetry parameter. A twin boundary can be seen in the red box.*

Grain boundary sliding and grain rotation were detected by looking at displacement vectors for each atom in the system as seen in figure 7.6. We

find abrupt changes in the directions of the displacement vectors across grain boundaries indicating that grain boundary sliding is occuring. The pattern of the displacement vectors indicates that some grain rotation is also taking place.

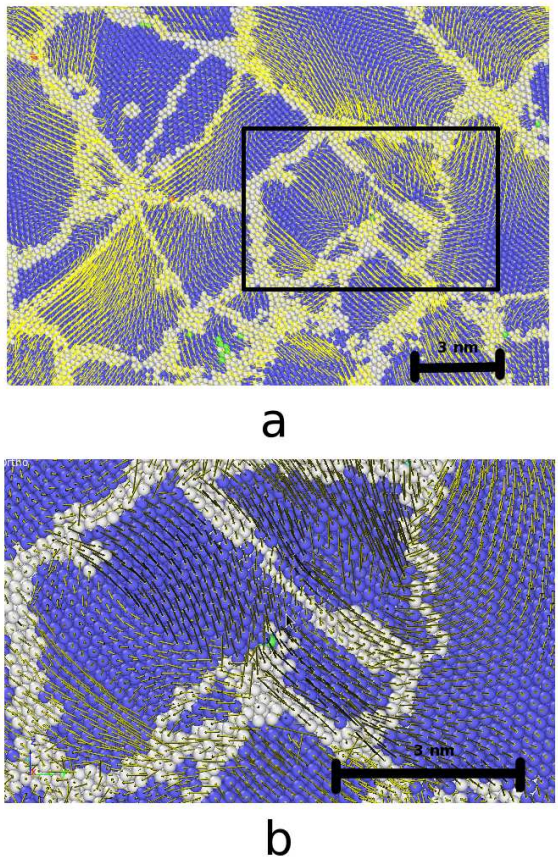

Figure 7.6 *(a) Vector displacement map of the system at 300K following a strain of 16%. Atoms are coloured according to centrosymmetry parameter. The yellow lines represent displacement vectors for movements of each atom over a 100 ps interval. A close up of the section contained in the black box can be seen in (b). Abrupt changes in the displacement vectors across grain boundaries indicate grain boundary sliding. Flow lines running in and out of amorphous areas or grain boundaries indicates recrystallization. Both images were generated using the Ovito software package. Atoms in are coloured according to the Ackland-Jones identification technique. Blue atoms represent bcc atoms while grey atoms are unidentified atoms.*

We see grain elongation in the direction of shear as seen in many experiments. The evolution of the grain structure can be seen in figure 7.7.

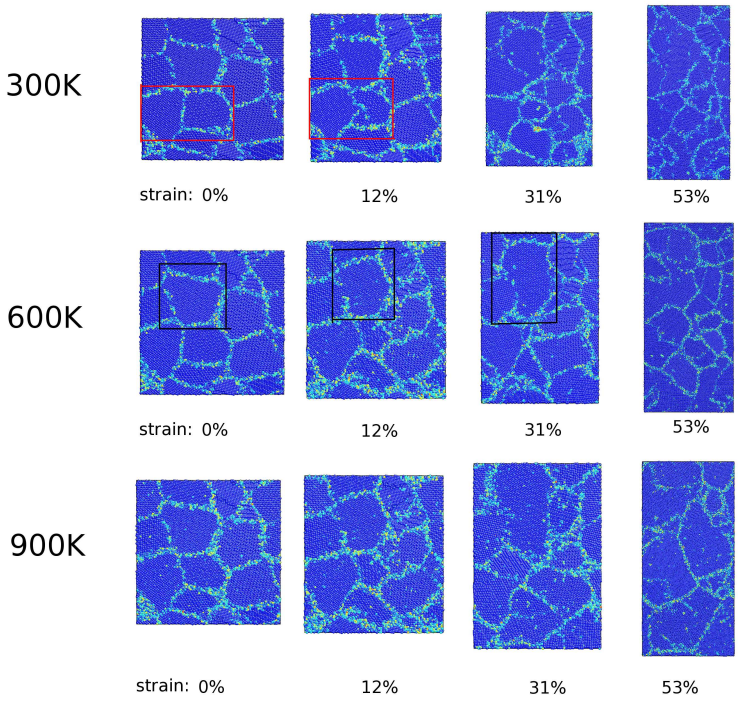

Figure 7.7 *Images showing evolution of grain structure for shear at low temperatures generated using AtomEye. Each image shows a cross section of the full system viewed in the direction of compression. Atoms are coloured according to centrosymmetry parameter. Dark blue atoms are bcc atoms and all other colours represent disordered atoms. The samples remain crystalline even at high strain. Two grains can be seen in the red squares in the 300K sequence. The grain boundary between these two grains moves as the grains recrystallise. Similarly a single grain is shown in the red squares in the 600K sequence. A significant amount of grain elongation is visible in this grain.*

7.2.4 High Temperature Plasticity

In the simulations at 1200K and 1500K the deformation regime changed. Slip and twinning no longer took place and the deformation was dominated by grain boundary sliding. At very high strains, the deformation occurs by much of the sample turning amorphous. Figure 7.8 shows the evolution of the grain structure for these simulations. In contrast to the low temperature deformation regime, the number of grains in the simulation reduces as the shear takes place. At very high strains the amount of crystalline material reduces and much of the material becomes amorphous.

In the initial stages of shear, grain boundary sliding is the dominant means of

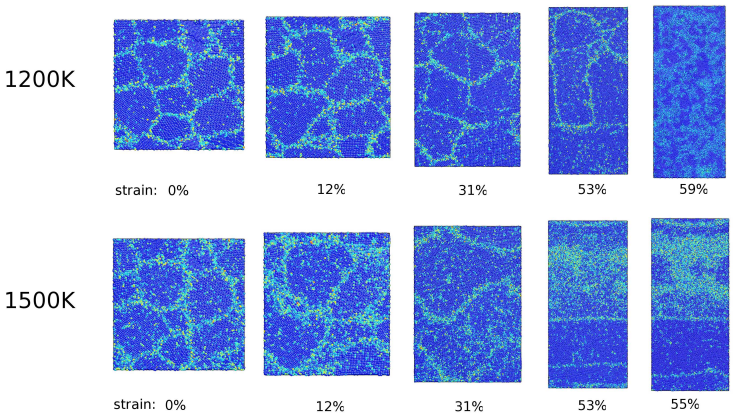

Figure 7.8 *Images showing evolution of grain structure for shear at high temperatures generated using AtomEye. Each image shows a cross section of the full system viewed in the direction of compression. Atoms are coloured according to centrosymmetry parameter. Dark blue atoms are bcc atoms and all other colours represent disordered atoms. Large segments of the samples become amorphous at high strain.*

deformation. This can be seen in the vector displacement map seen in figure 7.9. The abrupt changes in the direction of the displacement vectors are more clearly defined than in the low temperature case.

At high strains, when much of the system has turned amorphous, the plasticity takes place mostly in the amorphous parts. This can be seen from the vector displacement map in figure 7.10. The displacement vectors in the crystalline part are all in the same direction indicating that the crystalline atoms move together and no deformation takes place in the inner parts of these crystalline segments. The displacement vectors in the amorphous parts are varied, indicating that the shape of the crystalline parts change to accommodate the movement of the crystalline parts.

The fact that the plasticity takes place mostly in the amorphous parts can also be seen by looking at neighbour list changes for each atom as described in section 3.8.2. An image of the sample after 55% strain can be seen in figure 7.11. Only the atoms for which the neighbour list has changed by more than four are shown in figure 7.11(c). The atoms with large neighbourlist changes are located overwhelmingly in the amorphous region.

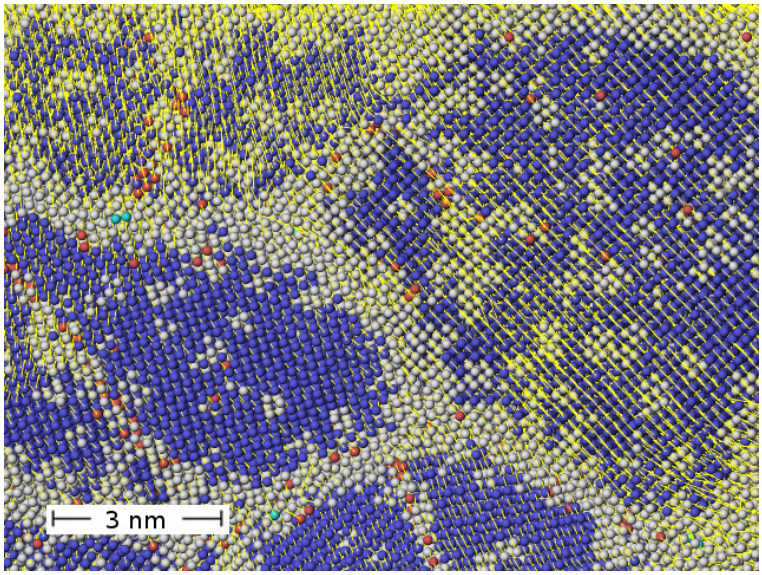

Figure 7.9 *Cross section and vector dislacement map for system strained by 22% at 1200K. Atoms are coloured according to centrosymmetry parameter. The yellow lines represent displacement vectors for atom movements over a 100 ps interval. Abrupt changes in displacement vectors across grain boundaries are more clearly defined at this temperature.*

7.2.5 Stress vs Strain Behaviour

In the early stages of the simulations (in both low and high temperature regimes), the stress vs strain signatures are similar to those observed by Shiotz *et al* for fcc nanocrystalline samples[153]. The stress initially increases linearly then levels off when plastic deformation begins to take place. However, at high strains the the stress rises again considerably. The stress vs strain curves can be seen in figure 7.12.

The effective hardening of the material can be explained by the change in grain structure in the cell. At low strains, grain boundary sliding accounts for much of the plasticity. With periodic boundary conditions imposed, grain boundary sliding can no longer provide the plastic deformation needed to reduce stress if the grain boundaries run parallel to the direction of compression. At high strains the length of the cell in the direction of compression becomes smaller and most of the grain boundaries lying normal to direction of compression have disappeared. This can be seen in figure 7.13 which shows one of the smaller faces of the cell after a strain of 57%.

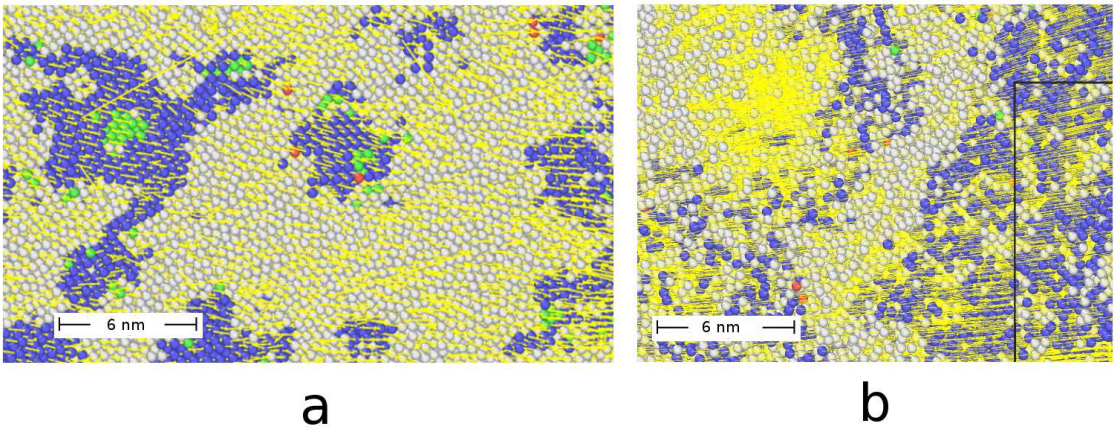

Figure 7.10 *Vector displacement maps for (a) system strained by 57% at 1200K and (b) system strained by 55% at 1500K. Yellow lines represent displacement vectors for atom movements over a 100 ps interval and atoms are coloured according to centrosymmetry parameter. Here the blue atoms are bcc and the grey atoms are amorphous. In these images the crystalline atoms have displacement vectors which are alligned while the displacement vectors for the amorphous atoms are more disordered. This indicates that most of the plastic deformation is taking place in the amorphous regions.*

7.3 Discussion

The length scales in these simulations are smaller than those for a shear band in an experimental sample. Both the grain size and the width of the shear band are larger experimentally. Our grain sizes were ∼7 nm while typical alloys used in machining experiments have grain sizes in the order of tens of microns [34]. After machining chips were formed, nanocrystalline (grain sizes less than 100 nm) structure was observed in shear bands of Ti-15V-3Al-3Sn-3Cr alloys. Typical shear bands in chips produced from machining are a few microns in width[34] while our system was just 23 nm in width. The implementation of periodic boundary conditions means that our simulations represent a small segment within a shear band. The differences between plasticity behaviour in nanocrystalline and coarse grained metals is well understood. We can therefore separate the qualitative features of the simulation which are due to grain size and those which are due to high strain rates and temperatures. In our sample the total grain boundary surface area is large and we are therefore likely to see more grain boundary sliding than in experiments. The stresses we measure may be higher than in shear bands experimentally, as strain rates in MD are necessarily large.

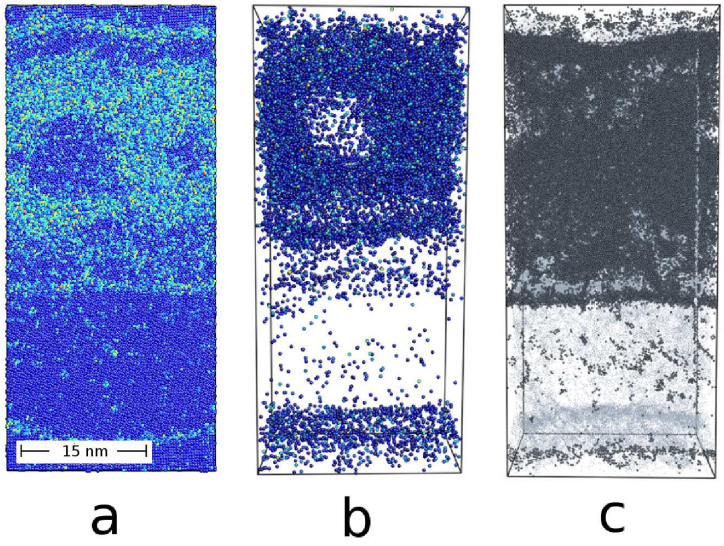

Figure 7.11 *(a) Images of sample strained by 55% at 1500K. Atoms coloured according to centrosymmetry parameter. (b) Same as (a) but only atoms with high centrosymmetry parameter are shown (c) Same as (a) but only showing atoms whose neighbour lists have changed by more than 4. It can be seen that the plasticity is taking place mostly in the amorphous parts of the system. Images created using AtomEye.*

However, some qualitative information gathered from these simulations may still be relevant to experiments. The transition in deformation mechanisms at high temperatures is likely to apply to experimental samples at high strain rates. Furthermore, there is now an trend towards producing alloys with nanoscale grains [7].

At all temperatures the stress begins to rise considerably at high strains. At this point most of the remaining grain boundaries run parallel to the direction of compression. Grain boundary sliding at this point cannot cause the desired shear. The plasticity at high strains is therefore quite different to that at lower strains. This is effectively a finite size effect, as the small size of the cell in one direction is preventing grain boundary sliding. However both of these plasticity behaviours may be relevant to shear bands in metals. At low strains the deformation is dominated by grain boundary sliding. This is due to the small size of our grains and consequent large amount of grain boundary surface area. Although the level of grain boundary sliding may be exaggerated, the transition away from slip and twinning may still hold in materials with larger grain sizes. At higher strains, grain boundary sliding contributes little to the

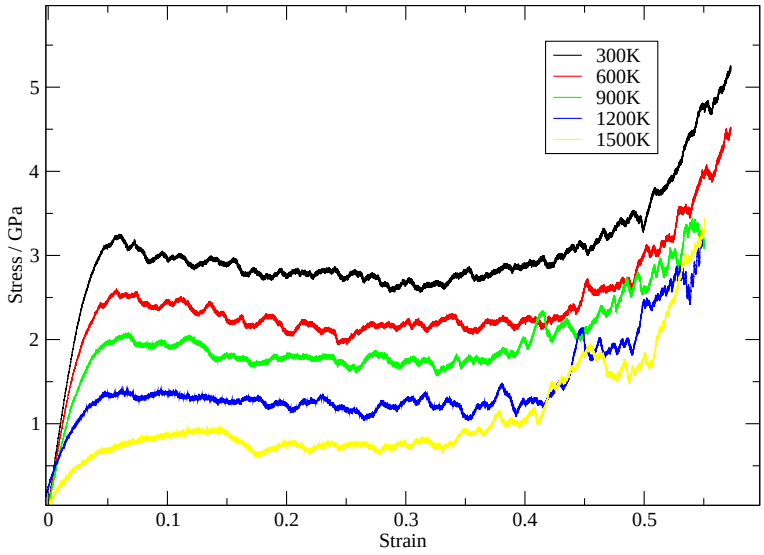

Figure 7.12 *Stress vs. strain for our simulations at strain rate of 2.5×10^8 s^{-1}. The rise in stress at high strains is due to lack of grain boundaries lying normal to the direction of compression. This means that grain boundary sliding is no longer an effective deformation mechanism.*

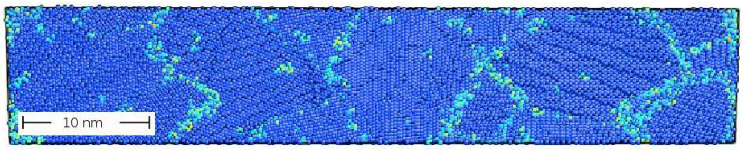

Figure 7.13 *View of the short face of the MD cell at a strain of 57%. Most of the grain boundaries now run more or less parallel to the compression direction making grain boundary sliding ineffective as a deformation mechanism. Atoms are coloured according to centrosymmetry parameter.*

deformation. Although this is effectively due to periodic boundary conditions and finite size effects, restricting grain boundary sliding in the system may cause the deformation behaviour to be more like that of a material with large grain sizes where grain boundary sliding may be prohibited by the lack of grain boundary surface area. Based on this evidence it is likely that at high temperatures and at high strain rates the plasticity behaviour of bcc materials changes. At low temperatures deformation will be mediated at least in part by slip and twinning. At higher temperatures grain boundary sliding and/or twinning will be the dominant deformation mechanisms. The shear bands produced during high speed cutting can reach temperatures over 1100K [167]. Grain boundary sliding and amorphization may play a part in the plasic deformation taking place in these

shear bands.

Our method of construction of this polycrystalline sample has not to our knowledge been used before in a published study. In previous studies, polycrystalline samples were created by a Voronoi construction. This involves first choosing a set of random points in the cell. Each of these points is assigned a grain and a grain orientation. Any point in the volume of the cell is then occupied by the grain assigned to the nearest of these randomly chosen points. Some atoms near the grain boundaries are usually then removed to prevent the energy of the system from becoming too large and the system is allowed to equilibrate for some period of time. With this method, there are little or no disordered atoms at the grain boundaries. The boundary is sharp and each grain develops a sawtooth profile at the boundaries. The steps in these sawtooth profile surfaces may act as dislocation sources and it may be easier for dislocations to cross grain boundaries if there are no disordered atoms in the grain boundaries to absorb atoms when the dislocations come into contact with these grain boundaries. As one might expect, based on this jagged grain surface profile, dislocations have been observed to emerge from the grain boundaries in previous studies. We do not see as many dislocations emerge from the grain boundaries. We do, however, see a significant amount of slip occur in the samples. This is partly due to creation of a network of dislocations when the sample is being created. As in previous simulations, we see a significant amount of twinning in the sample also.

7.4 Conclusion

We have performed molecular dynamics simulations involving pure shear of polycrystalline Fe. We find a transition in the deformation mechanisms at high temperatures. At low temperatures slip and twinning contribute significantly to the deformation while grain boundary sliding and recrystallization also take place. At high temperatures slip and twinning are not observed and the deformation is dominated by grain boundary sliding and recrystallization. At high strains, we find that grain boundary sliding is no longer effective due to grain boundaries now being aligned in the direction of compression. At these strains, deformation occurs through slip and twinning at low temperatures and through amorphization at high temperatures.

The results of these simulations suggest that amorphisation and grain boundary

sliding may take place in shear bands formed during high speed cutting of bcc materials. While temperatures are not believed to reach the melting temperature in segmented chip shear bands, the final microstructure of the shear bands is a nanocrystalline structure [34]. Our simulations suggest that amorphisation may occur in these shear bands below (but somewhat close to) the melting temperature. In previous attempts to produce free machining Ti alloys which produce short breaking segmented chips, elements such as lanthanum were added to Ti alloys in an attempt to lower the melting temperature of the alloy [34]. This is because the Johnson-Cook model described in section 2.8.1 shows a more pronounced thermal softening effect when the melting temperature is lower and this softening effect is necessary for the shear localisation effect which produces the shear bands seen in segmented chips. We have shown that an amorphisation effect can occur in metals at temperatures close to the melting temperature when the metal is subject to straining conditions similar to those in a shear band of a segmented chip. These amorphous regions in the chip will be less strongly bound than crystalline regions and this may account for the chips being short breaking. The amorphisation effect may also account for the change in the microstructure in the shear band as such a dramatic change in microstructure is unlikely to come from deformation by dislocations and twinning.

As a nanocrystalline structure has been found in the shear bands of machining chips of Ti alloys, the simulations presented here should represent plasticity in these shear bands reasonably accurately. Our simulations suggest that the Johnson-Cook model is an inappropriate model for accurately simulating shear bands in machining chips. This model assumes that the dominant plasticity mechanisms are dislocation glide and strain hardening. These mechanisms did not play a significant role in the plasticity behaviour of our simulated nanocrystalline sample.

Chapter 8

Conclusions

We have presented Molecular dynamics simulations of plasticity in various nanostructures. We have contributed to improving best practices in relation to simulations of nanopillar and nanowire plasticity. Nanopillars in simulations should be constructed with low energy crystallographic surfaces and constrained atoms should be introduced to avoid unwanted conservation of momentum effects. Results of simulations of plasticity in both bcc and fcc nanowires were examined and the implications on previous experimental results was discussed. In addition to this we have presented results from simulations of plasticity in polycrystalline Fe and discussed the implications of these results on experimental observations from high speed cutting experiments as well as FEM simulations of chip formation.

In chapter 4 we presented results from simulations of plasticity in nanopillars of Iron. The plasticity behaviour of the nanowires depended sensitively on certain aspects of the initial configuration of the simulation. In particular, we found that applying an incremental strain to the system by rescaling the coordinates led to conservation of momentum being imposed on the system as it was deformed and this put constraints on the final shape of the pillar. In addition to this we found that the choice of crystallographic surface on the faces of the pillar affected the results of the simulation. We found that the pillar deformed by amorphisation and buckled when it was constructed with {100} faces while it deformed by slip when constructed with low energy {110} faces. For this reason the use of high energy surfaces should be avoided in plasticity simulations. We also found that surface tension caused nanopillars to amorphise quickly under an applied strain when

simulations were carried out at high temperatures. These results are particularly relevant to much of the existing literature where nanopillars and nanowires are often set up with high energy surfaces and strains are often applied in a way that conserves momentum in the system.

In chapter 5 we presented results from plasticity simulations on nanopillars of bcc Iron in compression and tension. In compression deformation occured through glide of $\frac{1}{2}\langle 111\rangle$ on $\{110\}$ planes. A large amount of cross slip was observed allowing the dislocation lines to move more or less at 45° to the direction of compression. In tension the pillar deformed by twinning. The stress vs. strain signatures for tension and compression were strikingly different. The results agree qualitatively with recent experimental results and indicate the probable deformation mechanisms in those experiments.

In chapter 6 results from simulations of fcc Cu nanowires in tension and compression were presented. The differences in plasticity behaviour in tension and compression were minor in comparison with the behaviour of the pillars of bcc Iron. In both compression and tension deformation occured through movement of Shockley partials on $\{111\}$ planes. In tension many vacancies were created in the pillar.

In chapter 7 we presented results from simulations of pure shear on a polycrystalline sample of Iron. Plasticity occurred through a range of mechanisms including slip, twinning and grain boundary sliding. At high temperatures dislocation glide did not occur. At high strains and temperatures, deformation occurred through amorphisation. This might suggest that amorphisation can occur in the shear bands of segmented chips during high speed cutting of metals. The observation of amorphisation in the sample as well as a significant amount of grain boundary sliding suggests that at high strain rates, and particularly at high temperatures, the plasticity behaviour of metals may change considerably. This may mean that the current practice of extrapolating empirical models over several orders of magnitude is unreliable and FEM simulations using such models may be of little help with regards to predicting chip morphology.

8.1 Suggested future research

This thesis has provided some insights into the plasticity behaviour of nanostructures with some relevance to machining processes. There are many avenues of research which could still be explored in this are. Here we briefly present some interesting directions for further research.

Plasticity of hcp nanostructures is an area particularly lacking in published work. The author of this thesis is not aware of any published work reporting molecular dynamics simulations of nanopillars or of nanocrystalline material. Many materials used in industry (some Ti alloys in particlar) are hcp.

Ultrasonic vibrations are often applied to the workpiece during machining processes in industry. This has the effect of reducing the stresses on the cutting tool. The exact reasons for this effect are still unknown. It would therefore be useful to perform plasticity simulations on various systems while ultrasonic vibrations are applied to the system.

The compression-tension asymmetry described in chapter 5 is currently not exploited by machining equipment. Developing cutting tools or other elements of a machining apparatus which lower the force on the cutting tool during high speed cutting could be very useful. This could be achieved by designing the machining apparatus in such a way that local tensile stresses are applied to much of the internal part of the chip as during chip formation. The shape of the cutting tool and the speed at which it is applied to the work piece could perhaps be altered to achieve such a goal. Finite element simulations could be used to determine the stress distribution in the chip during chip formation for proposed new cutting tool shapes.

Perhaps the most important and most challenging goal for simulating chip formation in the future is to develop a simulation technique which can predict the dynamics and microstructure evolution of a full shear band accurately. More generally, a simulation technique is needed which can accurately predict microstructure evolution in systems with length scales which range from 100 nm to 100 μn. Finite element simulations cannot predict microstructural evolution of such small length scales as they lack the necessary physical accuracy while molecular dynamics simulations require too much computing time to simulate systems of that size. Perhaps molecular dynamics can provide some input for

finite element simulations which is more sophisticated than the Johnson-Cook constitutive model. A simulation technique used for these purposes would have to be capable of predicting a wide range of plasticity behaviour including (but possibly not limited to) dislocation glide, twinning, grain boundary sliding, and amorphisation.

Appendix A

Determining Burgers vectors and dislocation lines in the DXA

Here we present further details of the dislocation line tracing and Burgers vector calculation in the dislocation extraction algorithm presented in section 3.8.5.

To calculate burgers vectors, burgers circuits are traced around the dislocation on the surface mesh. This is done by moving between adjacent nodes until a closed loop is formed enclosing the dislocation. To accomplish this, Stukowski creates a halfedge data structure. This sort of data structure is commonly used in computational geometry codes [168]. The data structure contains facets, nodes, and halfedges and is illustrated in figure A.1. It is structured as follows:

- Triangular facets store three halfedges arranged in a circular sequence as shown in figure A.1. Each facet has associated with it a normal vector pointing away from the disordered atoms and towards the crystalline atoms.
- Each halfedge is associated with just one facet which it borders.
- Each halfedge connects a source node to a destination node and is associated with the vector which connects these nodes in the reference lattice.
- Each halfedge is associated with its opposite halfedge. This provides information on which facets border any given facet.
- Each node stores a list of the halfedges that point away from it.

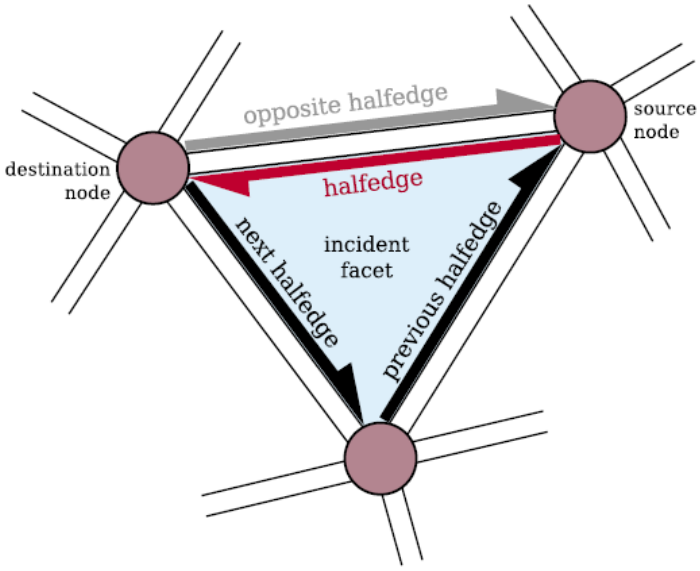

Figure A.1 *Illustration of the halfedge data structure. The structure consists of facets, nodes, and halfedges. Image taken from paper by Stukowski and Albe [83]*

Given this data structure one can easily trace find closed circuits of halfedges on the mesh surface collecting the associated lattice vector for each halfedge in the process. The accessibility of lists of neighbouring facets for any given facet will become useful in later parts of the algorithm.

The interface mesh is constructed by searching for near neighbours of each interface atom which can be connected together to form a triangular or quadrangular facet. All quadrangular facets are broken up into two triangular facets by running a triangle vertex diagonally through the quadrangular facet.

For certain defects, for example a stacking fault, only a single plane of atoms might be designated as interface atoms. In this case, facets can share their 3 nodes with a facet pointing in the opposite direction. These nodes have to be duplicated to make sure that circuits can be traversed on the mesh surface later on. This node duplication procedure is illustrated in figure A.2. To determine whether or not a node must be duplicated, all facets bordering the node are traversed in clock-wise order. If there are remaining facets adjacent to this node which have not then been traversed, the node must be duplicated.

One can now search for burgers circuits on the mesh surface and calculate the respective burgers vector. This is done by searching for closed circuits of halfedges on the mesh surface.

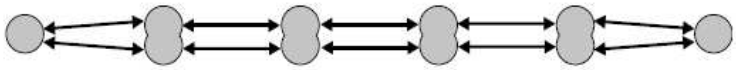

Figure A.2 *Illustration of node duplication required when just one plane of atoms is classified as interfaced atoms. Image taken from paper by Stukowski and Albe [83]*

As the circuits are traced a sequence of the halfedges traversed are collected. If the sequence of lattice vectors corresponding to each of these halfedges is denoted $\{\mathbf{e}_1, \mathbf{e}_2, \mathbf{e}_3, ..., \mathbf{e}_n\}$, then the burgers vector, $\mathbf{b}$, is simply the sum of these vectors: $\mathbf{b} = \sum_{i=1}^{n} \mathbf{e}_i$. When a circuit is found which is a burgers circuit (i.e. one for which $\mathbf{b} \neq 0$) then the search is stopped as the burgers vector for the dislocation has been found.

Once a burgers circuit has been found, the circuit is duplicated and a burgers circuit sweeps though the dislocation line in both directions away from the original burgers circuit. The circuits are advanced by altering them by the replacement operations listed in figure A.3. At each step edges on the burgers circuit are changed to create a new burgers circuit. Facets which have been swept over are marked as having been covered. The burgers circuit does not sweep back over these facets. At each iteration of the burgers circuit progression, the centre of mass for the atoms on the circuit is calculated. The locations of these centres of mass are used to create a line in the output representing the dislocation. The burgers circuit is limited in size to consist of less than a number of halfedges, N_{max}, which is set by the user. This number must be large enough so that a circuit can be created which encloses the dislocation. The limitation on the size of the burgers circuit prevents the circuit from overexpanding when it reaches a grain boundary or dislocation node as shown if figure A.4. Note that grain boundaries still contribute to the surface mesh as a surface is is created for the boundary between all crystalline and disordered or defect areas of the crystal.

The dislocation lines are now present in the output. The grain boundary surface is also gathered from the surface mesh and sent to the output.

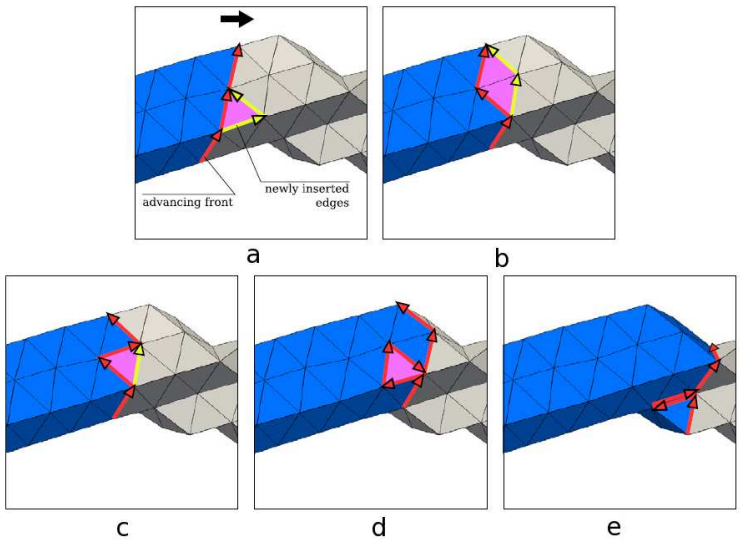

Figure A.3 *Image illustrating the elementary replacement operations implemented at each step during advancement of the burgers circuits along dislocation lines. (a) Replacing on edge with two edges, (b) replacing two edges with another two edges, (c) replacing two edges with one edge, (d) removing three edges, and (e) removing two edges. Image taken from paper by Stukowski and Albe [83]*

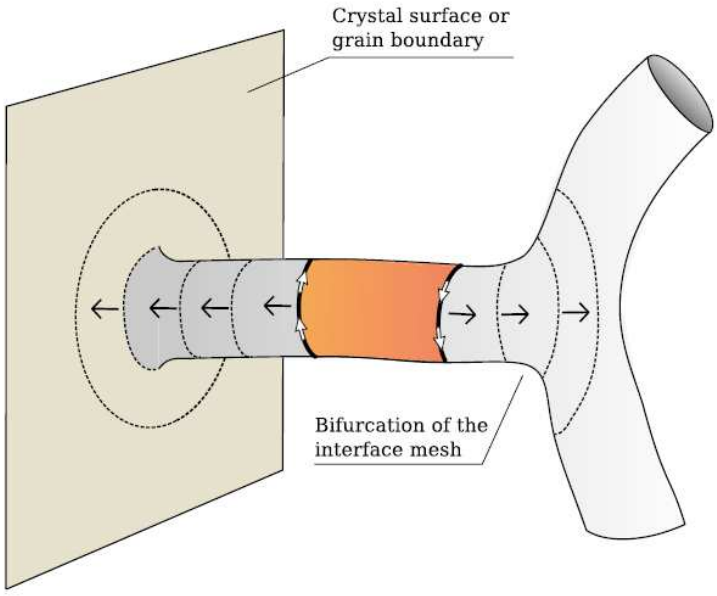

Figure A.4 *Graphic illustrating burgers vector advancement on a dislocation line. If the circuit continues to advance when it meets a grain boundary or a dislocation node, circuits will continue to be traced on the grain boundary surface or at the node which is not required. Limiting the size of the burgers circuit prevents this from happening. Image taken from paper by Stukowski and Albe [83]*

Bibliography

[1] Con J. Healy and Graeme J. Ackland. MD simulations of compression of nanoscale iron pillars. *MRS Proceedings*, 1369, 1 2011.

[2] Con J. Healy and Graeme J. Ackland. Molecular dynamics simulations of compression–tension asymmetry in plasticity of Fe nanopillars. *Acta Materialia*, 70:105 – 112, 2014.

[3] S J A Koh and H P Lee. Molecular dynamics simulation of size and strain rate dependent mechanical response of fcc metallic nanowires. *Nanotechnology*, 17:3451, 2006.

[4] Suzhi Li, Xiangdong Ding, Ju Li, Xiaobing Ren, Jun Sun, and Evan Ma. High-efficiency mechanical energy storage and retrieval using interfaces in nanowires. *Nano Letters*, 10(5):1774–1779, 2010.

[5] Harold S. Park and Jonathan A. Zimmerman. Modeling inelasticity and failure in gold nanowires. *Phys. Rev. B*, 72:054106, Aug 2005.

[6] M.A. Meyers, A. Mishra, and D.J. Benson. Mechanical properties of nanocrystalline materials. *Progress in Materials Science*, 51(4):427 – 556, 2006.

[7] CarlC. Koch. Structural nanocrystalline materials: an overview. *Journal of Materials Science*, 42(5):1403–1414, 2007.

[8] Helena Van Swygenhoven and Julia R. Weertman. Deformation in nanocrystalline metals. *Materials Today*, 9(5):24 – 31, 2006.

[9] Jakob Schiotz, Francesco D. Di Tolla, and Karsten W. Jacobsen. Softening of nanocrystalline metals at very small grain sizes. *Nature*, 391(6667):561–563, February 1998.

[10] T. H. Fang, W. L. Li, N. R. Tao, and K. Lu. Revealing extraordinary intrinsic tensile plasticity in gradient nano-grained copper. *Science*, 331(6024):1587–1590, 2011.

[11] Derek Hull. *Introduction to Dislocations*. Pergamon Press, 1 edition, 1985.

[12] E. Orowan. Zur kristallplastizität. i. *Zeitschrift für Physik*, 89(9-10):605–613, 1934.

[13] E. Orowan. Zur kristallplastizität. ii. *Zeitschrift für Physik*, 89(9-10):614–633, 1934.

[14] E. Orowan. Zur kristallplastizität. iii. *Zeitschrift für Physik*, 89(9-10):634–659, 1934.

[15] G. I. Taylor. The mechanism of plastic deformation of crystals. part i. theoretical. *Proceedings of the Royal Society of London. Series A*, 145(855):362–387, 1934.

[16] M. Polanyi. Über eine art gitterstörung, die einen kristall plastisch machen könnte. *Zeitschrift für Physik*, 89(9-10):660–664, 1934.

[17] Alexander Stukowski, Vasily V Bulatov, and Athanasios Arsenlis. Automated identification and indexing of dislocations in crystal interfaces. *Modelling and Simulation in Materials Science and Engineering*, 20(8):085007, 2012.

[18] Cornelis W. Passchier and Rudolph A.J. Trouw. *Microtectonics*. Springer, 1998.

[19] Boris K. Vainshtein, Vladimir M. Fridkin, and Vladimir L. Indenbom. *Modern Crystallography 2*. Springer, 2000.

[20] Peter Haasen. *Physical Metallurgy*. Cambridge University Press, 1996.

[21] Hiroki Moriwake, Akihide Kuwabara, Craig A. J. Fisher, Rong Huang, Taro Hitosugi, Yumi H. Ikuhara, Hideki Oki, and Yuichi Ikuhara. First-Principles Calculations of Lithium-Ion Migration at a Coherent Grain Boundary in a Cathode Material, LiCoO2. *Advanced Materials*, 25(4):618–622, 2013.

[22] J. Frenkel. Zur theorie der elastizitätsgrenze und der festigkeit kristallinischer körper. *Zeitschrift für Physik*, 37(7-8):572–609, 1926.

[23] J K Mackenzie and R Shuttleworth. A phenomenological theory of sintering. *Proceedings of the Physical Society. Section B*, 62(12):833, 1949.

[24] R Peierls. The size of a dislocation. *Proceedings of the Physical Society*, 52(1):34, 1940.

[25] Joachim Roesler, Harald Harders, and Martin Baeker. *Mechanical Behaviour of Engineering Materials*. Springer, 2006.

[26] N. Q. Chinh, P. Szommer, Z. Horita, and T. G. Langdon. Experimental evidence for grain-boundary sliding in ultrafine-grained aluminum processed by severe plastic deformation. *Advanced Materials*, 18(1):34–39, 2006.

[27] M.S. Duesbery and V. Vitek. Plastic anisotropy in b.c.c. transition metals. *Acta Materialia*, 46(5):1481 – 1492, 1998.

[28] M. S. Duesbery, V. Vitek, and D. K. Bowen. The effect of shear stress on the screw dislocation core structure in body-centred cubic lattices. *Proceedings of the Royal Society of London. A. Mathematical and Physical Sciences*, 332(1588):85–111, 1973.

[29] V. Vitek. Computer simulation of the screw dislocation motion in b.c.c. metals under the effect of the external shear and uniaxial stresses. *Proceedings of the Royal Society of London. A. Mathematical and Physical Sciences*, 352(1668):109–124, 1976.

[30] V. Vitek. Core structure of screw dislocations in body-centred cubic metals: relation to symmetry and interatomic bonding. *Philosophical Magazine*, 84(3-5):415–428, 2004.

[31] Mingliang Tian, Jinguo Wang, James Kurtz, Thomas E. Mallouk, and M. H. W. Chan. Electrochemical growth of single-crystal metal nanowires via a two-dimensional nucleation and growth mechanism. *Nano Letters*, 3(7):919–923, 2003.

[32] Jose Luis Elechiguerra, Jose Reyes-Gasga, and Miguel Jose Yacaman. The role of twinning in shape evolution of anisotropic noble metal nanostructures. *J. Mater. Chem.*, 16:3906–3919, 2006.

[33] Yue Wu, Yi Cui, Lynn Huynh, Carl J. Barrelet, David C. Bell, and Charles M. Lieber. Controlled growth and structures of molecular-scale silicon nanowires. *Nano Letters*, 4(3):433–436, 2004.

[34] Carsten Siemers, Judith Laukart, Badya Zahra, Joachim Rosler, Zdenek Spotz, and Karel Saksl. Development of advanced and free-machining titanium alloys by micrometer-size particle distribution. *Mater. Sci. Forum*, 690:262 – 265, 2011.

[35] Edward M. Trent and Paul K. Wright. Chapter 11 - high speed machining. In Edward M. Trent and Paul K. Wright, editors, *Metal Cutting (Fourth Edition)*, pages 339 – 369. Butterworth-Heinemann, Woburn, fourth edition edition, 2000.

[36] Jyotsna Majumdar and Indranil Manna. *Laser-Assisted Fabrication of Materials*. Springer, 2013.

[37] Bertram Hopkinson. A method of measuring the pressure produced in the detonation of high explosives or by the impact of bullets. *Philosophical Transactions of the Royal Society of London. Series A, Containing Papers of a Mathematical or Physical Character*, 213(497-508):437–456, 1914.

[38] Murat Demiral, Tonu Leemet, Mikko Hokka, Tapani Kuokkala, Anish Roy, and Vadim Silberschmidt. Finite-Element Simulations of Split Hopkinson Test of Ti-Based Alloy. *Advanced Materials Research*, 223:296 – 303, 2011.

[39] Feng Dai, Sheng Huang, Kaiwen Xia, and Zhuoying Tan. Some fundamental issues in dynamic compression and tension tests of rocks using split hopkinson pressure bar. *Rock Mechanics and Rock Engineering*, 43(6):657–666, 2010.

[40] Michael D. Uchic, Dennis M. Dimiduk, Jeffrey N. Florando, and William D. Nix. Sample dimensions influence strength and crystal plasticity. *Science*, 305(5686):986–989, 2004.

[41] C Marichal, H Van Swygenhoven, S Van Petegem, and C Borca. {110} slip with {112} slip traces in bcc tungsten. *Sci. Rep.*, 2013.

[42] Michael D. Uchic, Paul A. Shade, and Dennis M. Dimiduk. Plasticity of micrometer-scale single crystals in compression. *Annu. Rev. Mater. Res.*, 39:361–386, 2009.

[43] Dongchan Jang and Julia R. Greer. Size-induced weakening and grain boundary-assisted deformation in 60 nm grained Ni nanopillars. *Scripta Materialia*, 64(1):77 – 80, 2011.

[44] J. S. Carpenter, A. Misra, M. D. Uchic, and P. M. Anderson. Strain rate sensitivity and activation volume of Cu/Ni metallic multilayer thin films measured via micropillar compression. *Applied Physics Letters*, 101(5):–, 2012.

[45] Ferenc F. Csikor, Christian Motz, Daniel Weygand, Michael Zaiser, and Stefano Zapperi. Dislocation avalanches, strain bursts, and the problem of plastic forming at the micrometer scale. *Science*, 318(5848):251–254, 2007.

[46] A. Dubach, R. Raghavan, J.F. Löffler, J. Michler, and U. Ramamurty. Micropillar compression studies on a bulk metallic glass in different structural states. *Scripta Materialia*, 60(7):567 – 570, 2009.

[47] Seung Min Han, Tara Bozorg-Grayeli, James R. Groves, and William D. Nix. Size effects on strength and plasticity of vanadium nanopillars. *Scripta Materialia*, 63(12):1153 – 1156, 2010.

[48] D. Kiener, P.J. Guruprasad, S.M. Keralavarma, G. Dehm, and A.A. Benzerga. Work hardening in micropillar compression: In situ experiments and modeling. *Acta Materialia*, 59(10):3825 – 3840, 2011.

[49] K.S. Ng and A.H.W. Ngan. Stochastic nature of plasticity of aluminum micro-pillars. *Acta Materialia*, 56(8):1712 – 1720, 2008.

[50] Fredrik Östlund, Philip R. Howie, Rudy Ghisleni, Sandra Korte, Klaus Leifer, William J. Clegg, and Johann Michler. Ductile–brittle transition in micropillar compression of gaas at room temperature. *Philosophical Magazine*, 91(7-9):1190–1199, 2011.

[51] Fredrik Östlund, Karolina Rzepiejewska-Malyska, Klaus Leifer, Lucas M. Hale, Yuye Tang, Roberto Ballarini, William W. Gerberich, and Johann Michler. Brittle-to-ductile transition in uniaxial compression of silicon pillars at room temperature. *Advanced Functional Materials*, 19(15):2439–2444, 2009.

[52] Ju-Young Kim, Dongchan Jang, and Julia R. Greer. Tensile and compressive behavior of tungsten, molybdenum, tantalum and niobium at the nanoscale. *Acta Materialia*, 58(7):2355 – 2363, 2010.

[53] Ju-Young Kim, Dongchan Jang, and Julia R. Greer. Crystallographic orientation and size dependence of tension–compression asymmetry in molybdenum nano-pillars. *International Journal of Plasticity*, 28(1):46 – 52, 2012.

[54] Ju-Young Kim and Julia R. Greer. Tensile and compressive behavior of gold and molybdenum single crystals at the nano-scale. *Acta Materialia*, 57(17):5245 – 5253, 2009.

[55] Gordon R. Johnson and William H. Cook. A constitutive model and data for metals subjected to large strains, high strain rates and high temperatures. In *Proc. 7th International Symposium on Ballistics*, pages 541–547, 1983.

[56] Martin Baker. Finite element investigation of the flow stress dependence of chip formation. *Journal of Materials Processing Technology*, 167(1):1 – 13, 2005.

[57] Aviral Shrot and Martin Bäker. Is it possible to identify johnson-cook law parameters from machining simulations? *International Journal of Material Forming*, 3(1):443–446, 2010.

[58] D. C.. Rapaport. *The Art of Molecular Dynamics Simlation*. Cambridge University Press, 2004.

[59] Zijun Yan. General thermal wavelength and its applications. *European Journal of Physics*, 21(6):625, 2000.

[60] Charles Kittel. *Introduction to Solid State Physics*. Wiley, 2004.

[61] M. W. Finnis and J. E. Sinclair. A simple empirical N-body potential for transition metals. *Philosophical Magazine A*, 50(1):45–55, 1984.

[62] Murray S. Daw and M. I. Baskes. Embedded-atom method: Derivation and application to impurities, surfaces, and other defects in metals. *Phys. Rev. B*, 29:6443–6453, Jun 1984.

[63] Ducastelle. Modules élastiques des métaux de transition. *J. Phys. France*, 31(11-12):1055–1062, 1970.

[64] G J Ackland, M W Finnis, and V Vitek. Validity of the second moment tight-binding model. *Journal of Physics F: Metal Physics*, 18(8):L153, 1988.

[65] Derek J. Hepburn and Graeme J. Ackland. Metallic-covalent interatomic potential for carbon in iron. *Phys. Rev. B*, 78:165115, Oct 2008.

[66] J.P. Biersack and J.F. Ziegler. Refined universal potentials in atomic collisions. *Nuclear Instruments and Methods in Physics Research*, 194(1–3):93 – 100, 1982.

[67] G. J. Ackland and V. Vitek. Many-body potentials and atomic-scale relaxations in noble-metal alloys. *Phys. Rev. B*, 41:10324–10333, May 1990.

[68] A. Subramaniyan and C. Sun. Continuum interpretation of virial stress in molecular simulations. *International Journal of Solids and Structures*, 45(14–15):4340 – 4346, 2008.

[69] Mark A. Tschopp, Douglas E. Spearot, and David L. McDowell. Chapter 82 influence of grain boundary structure on dislocation nucleation in fcc metals. In John Hirth, editor, *A Tribute to F.R.N. Nabarro*, volume 14 of *Dislocations in Solids*, pages 43 – 139. Elsevier, 2008.

[70] D T. Kulp, G J. Ackland, M. Sob, V. Vitek, and T. Egami. Many-body potentials for Cu-Ti intermetallic alloys and a molecular dynamics study of vitrification and amorphization. *Modelling and Simulation in Materials Science and Engineering*, 1(3):315, 1993.

[71] Loup Verlet. Computer "Experiments" on Classical Fluids. I. Thermodynamical Properties of Lennard-Jones Molecules. *Phys. Rev.*, 159:98–103, Jul 1967.

[72] William G. Hoover. Canonical dynamics: Equilibrium phase-space distributions. *Phys. Rev. A*, 31:1695–1697, Mar 1985.

[73] Shuichi Nose. A unified formulation of the constant temperature molecular dynamics methods. *The Journal of Chemical Physics*, 81(1):511–519, 1984.

[74] M. Parrinello and A. Rahman. Polymorphic transitions in single crystals: A new molecular dynamics method. *Journal of Applied Physics*, 52(12):7182–7190, 1981.

[75] G.J. Ackland, K. D'Mellow, S.L. Daraszewicz, D.J. Hepburn, M. Uhrin, and K. Stratford. The MOLDY short-range molecular dynamics package. *Computer Physics Communications*, 182(12):2587 – 2604, 2011.

[76] G. J. Ackland and A. P. Jones. Applications of local crystal structure measures in experiment and simulation. *Phys. Rev. B*, 73:054104, Feb 2006.

[77] Ju Li. AtomEye: an efficient atomistic configuration viewer. *Modelling and Simulation in Materials Science and Engineering*, 11(2):173, 2003.

[78] Alexander Stukowski. Visualization and analysis of atomistic simulation data with OVITO–the Open Visualization Tool. *Modelling and Simulation in Materials Science and Engineering*, 18(1):015012, 2010.

[79] P. D. Lane, G. J. Galloway, R. J. Cole, M. Caffio, R. Schaub, and G. J. Ackland. Validating molecular dynamics with direct imaging of radiation damage debris. *Phys. Rev. B*, 85:094111, Mar 2012.

[80] Cynthia L. Kelchner, S. J. Plimpton, and J. C. Hamilton. Dislocation nucleation and defect structure during surface indentation. *Phys. Rev. B*, 58:11085–11088, Nov 1998.

[81] Alexander Stukowski. Structure identification methods for atomistic simulations of crystalline materials. *Modelling and Simulation in Materials Science and Engineering*, 20(4):045021, 2012.

[82] J. Dana. Honeycutt and Hans C. Andersen. Molecular dynamics study of melting and freezing of small lennard-jones clusters. *The Journal of Physical Chemistry*, 91(19):4950–4963, 1987.

[83] Alexander Stukowski and Karsten Albe. Extracting dislocations and non-dislocation crystal defects from atomistic simulation data. *Modelling and Simulation in Materials Science and Engineering*, 18(8):085001, 2010.

[84] Futoshi Shimizu, Shigenobu Ogat, and Ju Li. Theory of shear banding in metallic glasses and molecular dynamics calculations. *Materials Transactions*, 48:2923–2927, 2007.

[85] D. V. Bachurin and P. Gumbsch. Elastic and plastic anisotropy after straining of nanocrystalline palladium. *Phys. Rev. B*, 85:085407, Feb 2012.

[86] Nina Gunkelmann, Eduardo M. Bringa, Keonwook Kang, Graeme J. Ackland, Carlos J. Ruestes, and Herbert M. Urbassek. Polycrystalline iron under compression: Plasticity and phase transitions. *Phys. Rev. B*, 86:144111, Oct 2012.

[87] Søren L. Frederiksen, Karsten W. Jacobsen, and Jakob Schiøtz. Simulations of intergranular fracture in nanocrystalline molybdenum. *Acta Materialia*, 52(17):5019 – 5029, 2004.

[88] Jong Bae Jeon, Byeong-Joo Lee, and Young Won Chang. Molecular dynamics simulation study of the effect of grain size on the deformation behavior of nanocrystalline body-centered cubic iron. *Scripta Materialia*, 64(6):494 – 497, 2011.

[89] R. Komanduri, N. Chandrasekaran, and L.M. Raff. Some aspects of machining with negative-rake tools simulating grinding: a molecular dynamics simulation approach. *Philisophical Magazine*, 79 (7):955–968, 1999.

[90] L. Proville, D. Rodney, and M.-C. Marinica. Quantum effect on thermally activated glide of dislocations. *Nature Materials*, 11:845–849, 2012.

[91] H. Swygenhoven, P. Derlet, and A. Froseth. Stacking fault energies and slip in nanocrystalline metals. *Nature Materials*, 3:399, 2004.

[92] J Marian, W Cai, and VV Bulatov. Dynamic transitions from smooth to rough to twinning in dislocation motion. *Nature Materials*, 3(3):158–163, Mar 2004.

[93] S. J. A. Koh, H. P. Lee, C. Lu, and Q. H. Cheng. Molecular dynamics simulation of a solid platinum nanowire under uniaxial tensile strain: Temperature and strain-rate effects. *Phys. Rev. B*, 72:085414, Aug 2005.

[94] Hideyuki Ikeda, Yue Qi, Tahir Çagin, Konrad Samwer, William L. Johnson, and William A. Goddard. Strain rate induced amorphization in metallic nanowires. *Phys. Rev. Lett.*, 82:2900–2903, Apr 1999.

[95] Dongchan Jang, Xiaoyan Li, Huajian Gao, and Julia R. Greer. Deformation mechanisms in nanotwinned metal nanopillars. *Nat Nano*, 7(9):594–601, 2012.

[96] Christopher R. Weinberger and Wei Cai. Surface-controlled dislocation multiplication in metal micropillars. *PNAS*, 105:14304–14307, 2008.

[97] M. Hou and O. Melikhova. Internal stress and mechanical deformation of Al and Al/Ni multilayered nanowires. *Acta Materialia*, 57(2):453 – 465, 2009.

[98] Xiaoyan Li and Wei Yang. Size dependence of dislocation-mediated plasticity in ni single crystals: Molecular dynamics simulations. *Journal of Nanomaterials*, 2009:1–10, 2009.

[99] Wei Cai, Maurice de Koning, Vasily V. Bulatov, and Sidney Yip. Minimizing boundary reflections in coupled-domain simulations. *Phys. Rev. Lett.*, 85:3213–3216, Oct 2000.

[100] K. Ohsawa and E. Kuramoto. Flexible boundary condition for a moving dislocation. *Journal of Applied Physics*, 86(1):179–185, 1999.

[101] Baolin Wang, Guanghou Wang, Xiaoshuang Chen, and Jijun Zhao. Melting behavior of ultrathin titanium nanowires. *Phys. Rev. B*, 67:193403, May 2003.

[102] Subramanian K. R. S. Sankaranarayanan, Venkat R. Bhethanabotla, and Babu Joseph. Molecular dynamics simulation of temperature and strain rate effects on the elastic properties of bimetallic Pd-Pt nanowires. *Phys. Rev. B*, 76:134117, Oct 2007.

[103] N. Abdolrahim, I. N. Mastorakos, and H. M. Zbib. Deformation mechanisms and pseudoelastic behaviors in trilayer composite metal nanowires. *Phys. Rev. B*, 81:054117, Feb 2010.

[104] C.-H. Nien, T. E. Madey, Y. W. Tai, T. C. Leung, J. G. Che, and C. T. Chan. Coexistence of {011} facets with {112} facets on W(111) induced by ultrathin films of Pd. *Phys. Rev. B*, 59:10335–10340, Apr 1999.

[105] T.E. Madey, C.-H. Nien, K. Pelhos, J.J. Kolodziej, I.M. Abdelrehim, and H.-S. Tao. Faceting induced by ultrathin metal films: structure, electronic properties and reactivity. *Surface Science*, 438(1–3):191 – 206, 1999.

[106] Z. L. Wang, R. P. Gao, B. Nikoobakht, and M. A. El-Sayed. Surface reconstruction of the unstable {110} surface in gold nanorods. *The Journal of Physical Chemistry B*, 104(23):5417–5420, 2000.

[107] He Zheng, Ajing Cao, Christopher R. Weinberger, Jian Yu Huang, Kui Du, Jianbo Wang, Yanyun Ma, Younan Xia, and Scott X. Mao. Discrete plasticity in sub-10-nm-sized gold crystals. *Nat Commun*, 1:144, Dec 2010.

[108] Jian Wang, Hanchen Huang, S. V. Kesapragada, and Daniel Gall. Growth of y-shaped nanorods through physical vapor deposition. *Nano Letters*, 5(12):2505–2508, 2005.

[109] Z. L. Wang, R. P. Gao, B. Nikoobakht, and M. A. El-Sayed. Surface reconstruction of the unstable {110} surface in gold nanorods. *The Journal of Physical Chemistry B*, 104(23):5417–5420, 2000.

[110] Cheng-Lun Hsin, Wenjie Mai, Yudong Gu, Yifan Gao, Chi-Te Huang, Yuzi Liu, Lih-Juann Chen, and Zhong-Lin Wang. Elastic properties and buckling of silicon nanowires. *Advanced Materials*, 20(20):3919–3923, 2008.

[111] Robert M. Jones. *Buckling of Bars, Plates, and Shells*. Bull Ridge Corperation, 2006.

[112] Pär A.T. Olsson and Harold S. Park. Atomistic study of the buckling of gold nanowires. *Acta Materialia*, 59(10):3883 – 3894, 2011.

[113] E. Rabkin, H.-S. Nam, and D.J. Srolovitz. Atomistic simulation of the deformation of gold nanopillars. *Acta Materialia*, 55(6):2085 – 2099, 2007.

[114] Eugen Rabkin and David J. Srolovitz. Onset of plasticity in gold nanopillar compression. *Nano Letters*, 7(1):101–107, 2007.

[115] Jiankuai Diao, Ken Gall, and Martin L. Dunn. Yield strength asymmetry in metal nanowires. *Nano Letters*, 4(10):1863–1867, 2004.

[116] Jiankuai Diao, Ken Gall, Martin L. Dunn, and Jonathan A. Zimmerman. Atomistic simulations of the yielding of gold nanowires. *Acta Materialia*, 54(3):643 – 653, 2006.

[117] Sergey Kotrechko and Alexander Ovsjannikov. Temperature dependence of the yield stress of metallic nano-sized crystals. *Philosophical Magazine*, 89(33):3049–3058, 2009.

[118] Yu-Hua Wen, Zi-Zhong Zhu, and Ru-Zeng Zhu. Molecular dynamics study of the mechanical behavior of nickel nanowire: Strain rate effects. *Computational Materials Science*, 41(4):553 – 560, 2008.

[119] Brad Lee Holian and Peter S. Lomdahl. Plasticity induced by shock waves in nonequilibrium molecular-dynamics simulations. *Science*, 280(5372):2085–2088, 1998.

[120] Alexey V. Bolesta, Lianqing Zheng, Donald L. Thompson, and Thomas D. Sewell. Molecular dynamics simulations of shock waves using the absorbing boundary condition: A case study of methane. *Phys. Rev. B*, 76:224108, Dec 2007.

[121] Konstantin A. Afanasyev and Frederic Sansoz. Strengthening in gold nanopillars with nanoscale twins. *Nano Letters*, 7(7):2056–2062, 2007.

[122] Christopher R. Weinberger and Wei Cai. Plasticity of metal nanowires. *J. Mater. Chem.*, 22:3277–3292, 2012.

[123] Ajing Cao and E. Ma. Sample shape and temperature strongly influence the yield strength of metallic nanopillars. *Acta Materialia*, 56(17):4816 – 4828, 2008.

[124] Jiankuai Diao, Ken Gall, and Martin L. Dunn. Surface stress driven reorientation of gold nanowires. *Phys. Rev. B*, 70:075413, Aug 2004.

[125] Suzhi Li, Xiangdong Ding, Junkai Deng, Turab Lookman, Ju Li, Xiaobing Ren, Jun Sun, and Avadh Saxena. Superelasticity in bcc nanowires by a reversible twinning mechanism. *Phys. Rev. B*, 82:205435, Nov 2010.

[126] Ju-Young Kim, Dongchan Jang, and Julia R. Greer. Insight into the deformation behavior of niobium single crystals under uniaxial compression and tension at the nanoscale. *Scripta Materialia*, 61(3):300 – 303, 2009.

[127] G. I. Taylor and C. F. Elam. The distortion of iron crystals. *Proceedings of the Royal Society of London. Series A*, 112(761):337–361, 1926.

[128] J. Christian. Some surprising features of the plastic deformation of body-centered cubic metals and alloys. *Metallurgical and Materials Transactions A*, 14:1237–1256, 1983.

[129] L. Hollang, M. Hommel, and A. Seeger. The flow stress of ultra-high-purity molybdenum single crystals. *physica status solidi (a)*, 160(2):329–354, 1997.

[130] R. Gröger, V. Racherla, J.L. Bassani, and V. Vitek. Multiscale modeling of plastic deformation of molybdenum and tungsten: II. Yield criterion for single crystals based on atomistic studies of glide of screw dislocations. *Acta Materialia*, 56(19):5412 – 5425, 2008.

[131] R. Gröger and V. Vitek. Multiscale modeling of plastic deformation of molybdenum and tungsten. III. Effects of temperature and plastic strain rate. *Acta Materialia*, 56(19):5426 – 5439, 2008.

[132] Gunther Richter, Karla Hillerich, Daniel S. Gianola, Reiner Mönig, Oliver Kraft, and Cynthia A. Volkert. Ultrahigh strength single crystalline nanowhiskers grown by physical vapor deposition. *Nano Letters*, 9(8):3048–3052, 2009.

[133] C.R. Liu and Y.B. Guo. Finite element analysis of the effect of sequential cuts and tool–chip friction on residual stresses in a machined layer. *International Journal of Mechanical Sciences*, 42(6):1069 – 1086, 2000.

[134] Albert J. Shih. Finite element analysis of the rake angle effects in orthogonal metal cutting. *International Journal of Mechanical Sciences*, 38(1):1 – 17, 1995.

[135] W Liang and M Zhou. Response of copper nanowires in dynamic tensile deformation. *Proceedings of the Institution of Mechanical Engineers, Part C: Journal of Mechanical Engineering Science*, 218(6):599–606, 2004.

[136] Haiyi Liang, Moneesh Upmanyu, and Hanchen Huang. Size-dependent elasticity of nanowires: Nonlinear effects. *Phys. Rev. B*, 71:241403, Jun 2005.

[137] Harold S. Park, Ken Gall, and Jonathan A. Zimmerman. Deformation of fcc nanowires by twinning and slip. *Journal of the Mechanics and Physics of Solids*, 54(9):1862 – 1881, 2006.

[138] Ajing Cao and Yueguang Wei. Atomistic simulations of the mechanical behavior of fivefold twinned nanowires. *Phys. Rev. B*, 74:214108, Dec 2006.

[139] J. Monk, J. J. Hoyt, and D. Farkas. Metastability of multitwinned Ag nanorods: Molecular dynamics study. *Phys. Rev. B*, 78:024112, Jul 2008.

[140] L. D. Marks. Surface structure and energetics of multiply twinned particles. *Philosophical Magazine A*, 49(1):81–93, 1984.

[141] Fenying Wang, Wei Sun, Yajun Gao, Yunhong Liu, Jianwei Zhao, and Changqing Sun. Investigation on the most probable breaking behaviors of copper nanowires with the dependence of temperature. *Computational Materials Science*, 67(0):182 – 187, 2013.

[142] H. Van Swygenhoven, P. M. Derlet, and A. G. Froseth. Stacking fault energies and slip in nanocrystalline metals. *Nat Mater*, 3(6):399–403, Jun 2004.

[143] H. Van Swygenhoven, P.M. Derlet, and A.G. Frøseth. Nucleation and propagation of dislocations in nanocrystalline fcc metals. *Acta Materialia*, 54(7):1975 – 1983, 2006.

[144] A. Hasnaoui, P.M. Derlet, and H. Van Swygenhoven. Interaction between dislocations and grain boundaries under an indenter – a molecular dynamics simulation. *Acta Materialia*, 52(8):2251 – 2258, 2004.

[145] A Hasnaoui, H Van Swygenhoven, and P.M Derlet. On non-equilibrium grain boundaries and their effect on thermal and mechanical behaviour: a molecular dynamics computer simulation. *Acta Materialia*, 50(15):3927 – 3939, 2002.

[146] D. Wolf, V. Yamakov, S.R. Phillpot, A. Mukherjee, and H. Gleiter. Deformation of nanocrystalline materials by molecular-dynamics simulation: relationship to experiments? *Acta Materialia*, 53(1):1 – 40, 2005.

[147] V. Yamakov, D. Wolf, M. Salazar, S.R. Phillpot, and H. Gleiter. Length-scale effects in the nucleation of extended dislocations in nanocrystalline Al by molecular-dynamics simulation. *Acta Materialia*, 49(14):2713 – 2722, 2001.

[148] H Van Swygenhoven, M Spaczer, and A Caro. Microscopic description of plasticity in computer generated metallic nanophase samples: a comparison between Cu and Ni. *Acta Materialia*, 47(10):3117 – 3126, 1999.

[149] H Van Swygenhoven, A Caro, and D Farkas. Grain boundary structure and its influence on plastic deformation of polycrystalline fcc metals at the nanoscale: a molecular dynamics study. *Scripta Materialia*, 44(8–9):1513 – 1516, 2001.

[150] H Van Swygenhoven, A Caro, and D Farkas. A molecular dynamics study of polycrystalline fcc metals at the nanoscale: grain boundary structure and its influence on plastic deformation. *Materials Science and Engineering: A*, 309–310(0):440 – 444, 2001. Dislocations 2000: An International Conference on the Fundamentals of Plastic Deformation.

[151] H. Van Swygenhoven, M. Spaczer, A. Caro, and D. Farkas. Competing plastic deformation mechanisms in nanophase metals. *Phys. Rev. B*, 60:22–25, Jul 1999.

[152] H. Van Swygenhoven, P. M. Derlet, and A. Hasnaoui. Atomic mechanism for dislocation emission from nanosized grain boundaries. *Phys. Rev. B*, 66:024101, Jun 2002.

[153] Jakob Schiotz, Francesco D. Di Tolla, and Karsten W. Jacobsen. Softening of nanocrystalline metals at very small grain sizes. *Nature*, 1998.

[154] M.A. Meyers, A. Mishra, and D.J. Benson. Mechanical properties of nanocrystalline materials. *Progress in Materials Science*, 51(4):427 – 556, 2006.

[155] A Latapie and D Farkas. Molecular dynamics simulations of stress-induced phase transformations and grain nucleation at crack tips in Fe. *Modelling and Simulation in Materials Science and Engineering*, 11(5):745, 2003.

[156] Yizhe Tang, Eduardo M. Bringa, and Marc A. Meyers. Inverse hall–petch relationship in nanocrystalline tantalum. *Materials Science and Engineering: A*, 580(0):414 – 426, 2013.

[157] Zhiliang Pan, Yulong Li, and Q. Wei. Tensile properties of nanocrystalline tantalum from molecular dynamics simulations. *Acta Materialia*, 56(14):3470 – 3480, 2008.

[158] Zhen Bing Hou and Ranga Komanduri. Modeling of thermomechanical shear instability in machining. *International Journal of Mechanical Sciences*, 39(11):1273 – 1314, 1997.

[159] Chunzheng Duan and Minjie Wang. A review of microstructural evolution in the adiabatic shear bands induced by high speed machining. *Acta Metallurgica Sinica (English Letters)*, 26(2):97–112, 2013.

[160] M.A. Meyers, Y.B. Xu, Q. Xue, M.T. Pérez-Prado, and T.R. McNelley. Microstructural evolution in adiabatic shear localization in stainless steel. *Acta Materialia*, 51(5):1307 – 1325, 2003.

[161] Q. Xue and III Gray, G.T. Development of adiabatic shear bands in annealed 316L stainless steel: Part II. TEM studies of the evolution of microstructure during deformation localization. *Metallurgical and Materials Transactions A*, 37(8):2447–2458, 2006.

[162] M.T Perez-Prado, J.A Hines, and K.S Vecchio. Microstructural evolution in adiabatic shear bands in Ta and Ta–W alloys. *Acta Materialia*, 49(15):2905 – 2917, 2001.

[163] M.I. Mendelev, S. Hans, D.J. Srolovitz, G.J. Ackland, D.Y. Sun, and M. Asta. Development of new interatomic potentials appropriate for crystalline and liquid iron. *Phil. Mag.*, 83:3977–3994, 2003.

[164] Y.Z. Chen, A. Herz, Y.J. Li, C. Borchers, P. Choi, D. Raabe, and R. Kirchheim. Nanocrystalline Fe–C alloys produced by ball milling of iron and graphite. *Acta Materialia*, 61(9):3172 – 3185, 2013.

[165] Basil Tikoff and Haakon Fossen. Simultaneous pure and simple shear: the unifying deformation matrix. *Tectonophysics*, 217(3–4):267 – 283, 1993.

[166] A Machova and G J Ackland. Dynamic overshoot in IMG alpha-iron by atomistic simulations. *Modelling and Simulation in Materials Science and Engineering*, 6(5):521, 1998.

[167] Martin Baker, Joachim Rösler, and Carsten Siemers. A finite element model of high speed metal cutting with adiabatic shearing. *Computers & Structures*, 80(5–6):495 – 513, 2002.

[168] Jakob Andreas Bræntzen. *Guide to computational geometry processing : foundations, algorithms, and methods / Jakob Andreas Bræntzen [and others].* Springer, 2012.